CAPACITIVE MICROMACHINED ULTRASONIC LAMB WAVE TRANSDUCERS

A DISSERTATION
SUBMITTED TO THE DEPARTMENT OF ELECTRICAL ENGINEERING
AND THE COMMITTEE ON GRADUATE STUDIES
OF STANFORD UNIVERSITY
IN PARTIAL FULFILLMENT OF THE REQUIREMENTS
FOR THE DEGREE OF
DOCTOR OF PHILOSOPHY

Mohammed Hanif Badi
April 2004

© Copyright by Mohammed Hanif Badi 2004
All Rights Reserved

I certify that I have read this dissertation and that, in my opinion, it is fully adequate in scope and quality as a dissertation for the degree of Doctor of Philosophy.

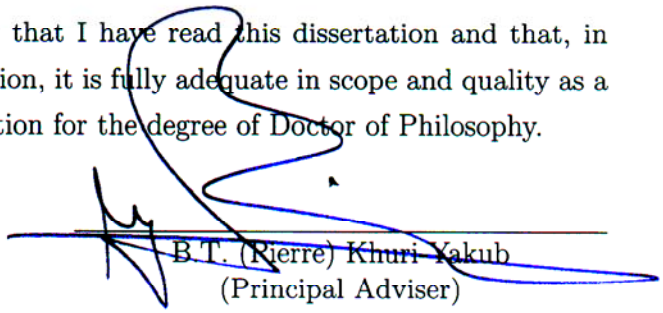

B.T. (Pierre) Khuri-Yakub
(Principal Adviser)

I certify that I have read this dissertation and that, in my opinion, it is fully adequate in scope and quality as a dissertation for the degree of Doctor of Philosophy.

Robert W. Dutton

I certify that I have read this dissertation and that, in my opinion, it is fully adequate in scope and quality as a dissertation for the degree of Doctor of Philosophy.

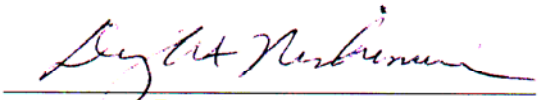

Dwight Nishimura

Approved for the University Committee on Graduate Studies.

Abstract

Many sensors and acoustic wave filters rely on the conversion of electrical energy into mechanical energy. This function is traditionally performed using a piezoelectric transducer in an interdigital configuration that launches acoustic waves along the substrate upon which the device is built. While almost all acoustic wave devices operate efficiently in a gaseous or vacuum ambient, only those that generate primarily shear motion in their substrate remain efficient in a liquid environment due to excessive damping. The exception to this rule occurs for devices that propagate waves with a velocity lower than that of sound in the liquid. Asymmetric Lamb waves, also known as flexural plate waves, fit this criterion. Furthermore, these waves generally operate in the 1-10 MHz range where the design and implementation of the accompanying electronics is relatively simple. As a result, asymmetric Lamb waves are often used in both sensor and filter applications. This dissertation describes the fabrication, modeling and experimental results of a novel device built for the transduction of Lamb waves using the Capacitive Micromachined Ultrasonic Transducer (CMUT).

The CMUT is similar to other capacitance transducers in that it employs a vibrating membrane to send and receive ultrasound in air and in water. Its invention was reported in 1994, and it has since found applications in a variety of arenas. The presence of Lamb waves in devices fabricated for the purpose of transmitting an acoustic signal into the surrounding medium has a deleterious effect on the system behavior. This is because the wave that is excited creates a cross-coupling of energy between otherwise independent cells. If this excitation of Lamb waves is instead exploited and optimized, however, the foundation for a new device is created.

The Lamb wave device described in this dissertation uses high aspect ratio CMUTs

built using two different fabrication techniques. The first results in a capacitive transducer built using the standard sacrificial-layer CMUT manufacturing process, while the second employs the significantly more robust and less labor-intensive wafer bonding method. Both arrays and single element structures have been built on substrates that have a thickness ranging from 500 microns down to 8 microns. They have been characterized using S-parameter, pitch-catch, and laser doppler vibrometer techniques, and their behavior is consistent with results from simulations performed using both analytical and finite element models. Measurements further demonstrate an insertion loss of 16.4 dB at 2.6 MHz for an electrically matched device fabricated using a single 60 μm x 1 cm CMUT at both the transmit and receive ports.

Acknowledgements

Many people have asked me why I chose to earn a PhD. After all, I have never had a strong interest in academia and speak often about a career in management rather than in research. The answer is that I wanted to go through the process. I wanted to have a chance to take a conceptual idea and lead it to maturity, overcome the challenges that would be sure to crop up along the way, and have a stronger and more confident mind as a result. I am pleased to report that I have achieved each of these goals, but not without the help of many people. So many, in fact, that I feel I will certainly miss someone. I arrived at Stanford as a freshman and have built many relationships throughout my undergraduate and graduate years. So if (when) I do leave someone out, know that it is not due to ungratefulness.

Let me begin with my advisor, Professor Pierre Khuri-Yakub. Not only is he my dissertation advisor, he was also the instructor of my very first engineering class. Since then he has been my de facto mentor and the source of many academic and industrial opportunities for which I am very grateful. He is very accessible for someone who is so busy and has an excellent knack for solving problems. A veteran graduate student once told me that the most important part of a PhD project is to choose a good advisor. Pierre has a well deserved reputation for being one of the best there is, and I feel lucky to have worked under his direction for so long.

I have known the rest of my committee since my undergraduate days as well, and they have been equally supportive of all my efforts while at Stanford. Professor Robert Dutton afforded my perhaps my most rewarding academic experience by allowing me to teach his analog circuit design class the year he went on sabbatical; Professor Dwight Nishimura was the instructor of my introductory Fourier transform

class and in my eyes is a model of the ideal teacher; Professor Francis Everitt gave me my first shot at research and has always had a wise word to share when I have turned to him for advice.

I received considerable help from my colleagues in the Khuri-Yakub lab. I'd especially like to thank Dr. Göksen Yaralioglu with whom I worked very closely throughout the course of the research presented here. He possesses a vast array of knowledge from which I borrowed often and freely; whenever he didn't have the answer, he'd utter the notorious words, "We'll talk about it later." Sure enough, a day or two later he'd walk up, I'd salute him (he is, after all, a Private in the Turkish army), and he'd have the answer. I also worked closely with Dr. Sanlı Ergun. A significant part of this research involved the fabrication of devices and Sanlı is a processing guru. His explanation of concepts was always very clear, he was never to busy to work with me, and my brainstorm sessions with him were among my most productive.

I'd like to acknowledge the rest of the Khuri-Yakub group who helped either my work or my sanity during my time in the lab. I also received considerable help from the Kenny Group, specifically Dan Laser and (now Professor) Beth Pruitt.

One day while walking down the street with yet another seasoned graduate student, I picked up a second tidbit of advice: avoid a PhD project that involves device fabrication. These were known to be the most frustrating and time consuming projects. This advice I did not follow, and quickly found myself in the Stanford Nanofabrication Facility (SNF) at three in the morning with an exploding silicon nitride LPCVD tube (and the two fire engines that came with it)! Lucky for me, the SNF process staff bent over backwards to train me on the equipment, help me with those difficult process steps, and give me a reason to smile whenever I put on a bunny suit. I am especially grateful to Nancy Latta, Ted Berg, Dick Crane, Jim Haydon, Paul Jerabek, Mahnaz Mansourpour, Gladys Sarmiento, Ray Seymour, Maurice Stevens, Mary Tang, and Uli Thumser.

The support staff at HEPL, Ginzton, CIS, and Packard have come through for me more times than I can possibly count. Thank you to Pete Cruz and Percy Medina at the receiving dock, Larry Randall for all his computer (and gaming) expertise, Pauline Prather for her bonding assistance, and Tom Carver in the Ginzton fab for

his creative ideas to help with my difficult problems. Also, the Ginzton front office crowd (Marilynne Elverson, Jenny Kienitz, Amy Hornibrook, and Darla Le-Grand-Sawyer) as well as Diane Shankle and Marianne Marx in the Packard front office. Finally, Lori Kohara (who was exiled to Ginzton with her HR group for a couple of years) for giving me a place right across the hall to vent, hang out, catch up on what's going on in the real world, and of course friendship.

Outside of the academic confines of the lab, I have many friends who I have counted on over and over again for advice, adventure, and companionship. First, Tutti Taychakhoonavudh, that strange girl on roller blades who kept inviting me to her dorm for lunch freshman year. She has always been there to give me a shoulder to cry on, to challenge my assumptions, to offer counsel, and to just go out and play. And the list continues: Jack Chu, for keeping me up with pop culture and always willing to go duck hunting with me; Mark Evans for being a worthy NHL '97 adversary and accepting me in spite of my alma mater; Mark Gudiksen for keeping me warm at 9000 feet and sane here at sea level; Sean Hansen for getting me into this field in the first place and doing me a "favour"; Sean Katz for Mercury through Pluto and Jupiter twice; Shabnam Moon for coffee on the sidewalk and KOHL; Frank O'Mahony for throwing magnets and that yummy carrot sauce; Myles Steiner for many tirades and teaching where "we" got it all from; and finally Eric Straver who has nodded his head three times through this section and for being my Prime Minister. I also thank the Popielatys, Kirchners, Mendelmans, and Andersons for opening their homes to me and their support and encouragement over the years.

I had a number of extracurricular activities that kept me busy and my mind stimulated outside of research. The most significant of these was the Stanford Canadian Club. I ran the group with Eric Straver for a number of years and received immense support from Bernie Etzinger, Brian Gardner, Mitch Poplack, Kelley Porter, and Anne Robinson. Another activity that often consumed me was The Game. I have played with two teams over the years. In New York I was with the G-Team (also known as Team Green[1]): Geetika Agrawala, Jack Chu, Alex Driggs, and Michael

[1]It's not easy being green.

Ehrman. In the Bay Area I hooked up with Team Advil: John Owens, Alex Aravanis, Scott Pegg, and Greg Yap.

A quick aside: I recently called my friend Andrew Northrop to chat and catch up with him. He is one of the primary reasons I came to Stanford and one of those guys who always does it right. I asked the perfunctory question, "How are you?" His answer left a big impression on me. He responded, "What can I say? I lead a lucky life." I thought about this and realised that he does, and then pondered the logical question – do I?

Of course I do. This luck is in part due to the people described above, those not mentioned, and my own efforts. The root of all of my luck, however, is family. Being able to take the time to earn a PhD is a luxury, and it is one that I have been able to afford only because I have had the unequivocal love and support of these wonderful people.

My beautiful wife Ahsia dealt with my erratic schedule, my days (weeks) of never being home because I had to work in lab, and my cranky moods as a result. Yet she has always been supportive of my work, drive, and ambition. Her charming smile and the twinkle in her eye picks me up when I'm down, and her constant adrenaline and sense of adventure pushes me even higher when I'm up. I am only just beginning to understand how well she completes me.

My sister Ghazala has always been my academic role model as well as my overall inspiration. I have never known life without her and in many ways I owe who I am to her. The best part of being the younger sibling is that one can borrow from the elder's experiences. She shares hers freely and looks out for me in ways that I'm sure I will never completely comprehend.

My parents, Zubeida and Abdul Aziz, have spent their lives affording me of every opportunity that could be made available, including the best education possible. They taught me to work hard, be confident, and show compassion. And perhaps most importantly, they never let me forget that I would have their love and support in anything I chose to do. I dedicate this work to them.

Contents

Abstract **v**

Acknowledgements **vii**

1 Introduction **1**

2 History **7**

2.1 1876 - 1917: Basic Formulation 7

2.2 1922 - 1951 10

2.2.1 Theory Extension 10

2.2.2 Wedge Method of Excitation 11

2.2.3 Reflections In The Plate 11

2.3 1945 - 1957 12

2.3.1 Propagation Along A Plate In Water 12

2.3.2 Experimental Verification Of Dispersion 12

2.4 1961 - 1965 13

2.4.1 Experimental Confirmation In The Megahertz Range 13

2.4.2 Four Basic Methods of Exciting Lamb Waves 15

2.5 1970 - Present 17

2.5.1 A Fifth "Basic" Method: Direct Coupling 18

2.5.2 The First Direct Coupled Lamb Wave Devices 18

2.5.3 Direct Coupled Lamb Wave Devices as Sensors 19

2.5.4 Combining Direct Coupled Devices With Integrated Circuits . 20

2.5.5 Direct Coupled Devices Without Piezoelectric Agents 21

2.5.6 Capacitive Micromachined Ultrasonic Lamb Wave Transducers 22

3 Fundamentals: The CMUT and Lamb Waves 23

3.1 CMUTs . . . 23

3.1.1 First Order Model . . . 25

3.1.2 Second Order Model: Small Signal Equivalent Circuit . . . 29

3.1.3 Manufacturing Process . . . 34

3.2 Lamb Waves . . . 36

3.2.1 Derivation of the Period Equation . . . 37

3.2.2 Analysis of the Period Equation . . . 43

3.2.3 Lamb Wave Properties . . . 44

3.3 Lamb Waves and CMUTs . . . 46

4 Modeling 48

4.1 Analytical Analysis: The Piston Model . . . 49

4.1.1 Membrane Impedance: Z_{mem} . . . 49

4.1.2 Device Capacitance: C_0 . . . 52

4.1.3 Radiation Impedance: Z_{rad} . . . 53

4.1.4 Transformer Ratio: n . . . 55

4.1.5 Spring Softening Capacitance: $-C_0/n^2$ . . . 55

4.1.6 Parasitic Impedances: C_p, R_{series}, *and* R_{shunt} . . . 55

4.1.7 Using The Piston Model . . . 56

4.2 Analytical Analysis: The Distributed Model . . . 59

4.2.1 Distributed Expressions for Spring Softening and the Transformer Turns Ratio . . . 59

4.2.2 Using The Distributed Model . . . 64

4.3 Equivalent Circuit Modeling of Lamb Wave Transduction . . . 65

4.4 The Finite Element Model . . . 67

4.4.1 Introduction to Finite Element Analysis . . . 67

4.4.2 Model Verification: A Piston CMUT . . . 68

4.4.3 Expanding the Finite Element Model . . . 71

4.5 Using The Finite Element Model . . . 74

4.5.1 Normal Mode Theory and Decomposition 75
4.5.2 Modeling The Lamb Wave Device In Air 77
4.5.3 Basic Electrical and Mechanical Characteristics 79
4.5.4 Device Conversion Loss 82
4.5.5 Analyzing the Transduction Mechanism 83
4.5.6 Effect of Absorbing Boundaries 88

5 Manufacturing Process **90**
5.1 The Sacrificial Layer Method 91
5.2 The Wafer Bonding Method 100
5.3 Method Comparison 104

6 Device Characterization **108**
6.1 Confirmation of the Electromechanical Model 108
6.2 Confirmation of Lamb Wave Transduction 115
6.2.1 Acoustic Wave Propagation 115
6.2.2 Comparing Acoustic Behavior to Lamb Waves 117
6.3 Analyzing and Optimizing Device Efficiency 118
6.3.1 Substrate Thinning 119
6.3.2 Matching Networks 121
6.3.3 Using a Single Membrane 123
6.4 Quantifying Device Efficiency 126
6.4.1 Three Generations Of Lamb Wave Devices 128
6.4.2 Accounting For Losses In Device 3 129
6.5 Lamb Wave Sensor Technology 129

7 Conclusions **133**
7.1 Contributions 134
7.2 Future Research 135

A Processing Details (Sacrificial Layer Method) **137**

B Processing Details (Wafer Bonding Method) **140**

Bibliography **143**

List of Tables

2.1 Select work done in the field of Lamb waves. 17

3.1 Variables used in (3.26) - (3.28) 37
3.2 Solutions to equations describing particle displacement of a Lamb wave. For u_1 and u_2, $\exp[\jmath(kx_1 - \omega t)]$ behaviour is assumed. 42

4.1 Circuit element modifications between the piston and distributed models. 65
4.2 Analytical expressions used in the calculation of the equivalent circuit prediction in Figure 4.14. Variables names reference schematic in Figure 4.1. 70
4.3 Values for variables in (4.31) are available from finite element analysis (FEA) or analytically. 75
4.4 Resonant frequencies using harmonic and modal analyses. 80

5.1 Etch rates of (100) silicon in (μm/hr) for various KOH concentrations and temperatures, after [78]. 94
5.2 Etch rates of thermally grown silicon dioxide in (nm/hr) for various KOH concentrations and temperatures, after [78]. 102

6.1 Device details for the three curves shown in Figure 6.21. 127

7.1 Comparison of the capacitive microcmachined ultrasonic Lamb wave transducer to other Lamb wave devices. 134

List of Figures

1.1 (a) Crystal structure supporting surface acoustic waves in a semi-infinite solid; (b)Interdigital transducer formed by patterned electrodes at the surface of a piezoelectric crystal. 2

1.2 Classical front-end topology of a high frequency circuit, consisting of an antenna, radio frequency (RF) filter, low noise amplifier (LNA), mixer, and an intermediate frequency (IF) filter. SAW devices are used to implement the filters. 3

1.3 Crystal structure supporting anti-symmetric and symmetric Lamb waves. 4

2.1 Theoretical and measured Lamb waves in an aluminum plate from Worlton [102]. 14

2.2 Four primary methods of Lamb wave excitation as described by Viktorov. See text for a description of the figures. 16

3.1 Four different ways in which to actuate capacitive transducers after [18, 47]. (a.1) The distance between the plates is varied; (a.2) An intermediate plate is moved relative to two fixed plates for use in differential measurements; (b.1) Overlap of the plates is varied with position; (b.2) Overlap of the plates is varied with position for use in differential measurements; (c) The dielectric constant between the plates is varied. 24

3.2 Diagram of an example CMUT membrane. 25

3.3 When the switch is open, the CMUT is in transmit mode; when it is closed, it is in receive mode and feeds the load R_L. 26

3.4 Lumped first order model of a CMUT. 26
3.5 Equivalent circuit model of a transmitting CMUT. 29
3.6 Diagram for a generic electromechanical transducer, after [38]. 30
3.7 Canonical form of the equivalent circuit symbolizing the coupling of an electrical mesh to a mechanical one by a symmetric transduction coefficient. 33
3.8 Equivalent forms of the equivalent circuit that describes the generic electromechanical transducer shown in Figure 3.6. 34
3.9 Equivalent circuit model of a transmitting CMUT. 35
3.10 (a) Geometry of a CMUT built using the sacrificial-layer process; (b) Geometry of a CMUT built using the wafer-bonding method. 35
3.11 Pictoral representations of the cross-section of elastic waves propagating to the right. Both vertical and horizontal displacements are exaggerated for clarity. (a) Bulk longitudinal (compressional) wave in an unbounded solid; (b) Bulk transverse (shear) wave in an unbounded solid; (c) Surface acoustic wave (SAW) in a semi-infinite solid; (d) Flexural plate waves (Lamb waves) in thin solid plates. 36
3.12 Illustrating the particle motion of a symmetric Lamb wave. (a) In the x_1 direction the particles follow a cosine behaviour as a function of x_2. Those above and below the center line $x_2 = 0$ move in the same direction. (b) In the x_2 direction the particles follow a sinusoidal behaviour as a function of x_2. Those that fall in the region $x_2 > 0$ move in the positive direction and those that are in the region $x_2 < 0$ move in the negative direction. 41
3.13 (a) Select Lamb and Rayleigh velocities on silicon. (b) An expansion of the A_0 curve for frequency-thickness values near .038 kHz-m, the operating point near the devices discussed in this paper. The calculations used to create both plots treat silicon as an isotropic material. The constants are taken from [4]: $V_s = 5840.9$ m/s, $V_l = 8429.4$ m/s. 43
3.14 Experimental setup of the delay-line oscillator. 45

3.15 Radiation pattern of a CMUT for different operating frequencies. The substrate thickness is 500 μm. After [43]. 47

4.1 Equivalent circuit model of a transmitting CMUT derived in Section 3.1.2. 49
4.2 Orientation of the rectangular membrane used to solve (4.1). 50
4.3 Diagram of a single CMUT membrane for the (a) sacrificial layer method and (b) wafer bonding method. 52
4.4 Real (solid) and imaginary (dashed) parts of the impedance presented by air to a membrane 1 cm long and 77 μm wide. Constants for air are taken from [45]: $\rho = 1.24$ kg/m^3, $v = 344$ m/s. 54
4.5 Geometry used in obtaining data presented in this chapter. 56
4.6 Static membrane deflection as a function of location for the structure shown in Figure 4.5. The ambient pressure on the membrane in this simulation is 1 atmosphere = 101.3 kPa. The constants used in this simulation are $Y_0 = 1.67$ x 10^{11} Pa, $\sigma = .053$, $\rho = 2332$ kg/m^3, and T = 100 MPa. 57
4.7 Membrane impedance for the structure shown in Figure 4.5. The solid line was obtained using the analytical equation in (4.3); the dashed line is a curve fit from a series LC circuit where L = 2.65 nH and C = 891.6 nF. 58
4.8 Input impedance for the structure shown in Figure 4.5. 59
4.9 Schematics used in the discussion to explain open and short circuit resonance phenomena. 60
4.10 Equivalent circuit of a transmitting CMUT using the nomenclature of [85]. 60
4.11 A comparison between the CMUT input impedance results obtained using the piston and distributed models. The curve representing the piston model is identical to the one shown in Figure 4.8. 64
4.12 Equivalent circuit of a transmitting CMUT modified to include the coupling effect of energy into a Lamb wave in the substrate. 66

4.13 Element used in FEA model verification. 68

4.14 Input impedance obtained from ANSYS and analytical expressions in conjunction with the equivalent circuit. While there are two curves in the above graph, only one is discernable. This is because results from the two methods are the same and their resulting curves superimpose exactly. The device geometry is the same as that described in Figure 4.5 and the device is assumed to be operating in vacuum. . . . 69

4.15 Membrane impedance under various conditions. In all cases the membrane width is 60 μm and is assumed to be vibrating in a vacuum. For (a) - (c) the membrane thickness is 1.34 μm. (a) Analytical (solid) and FEA (dashed) results when the membrane is under bias; (b) Analytical (solid) and FEA (dashed) results when the membrane is *not* under bias. Although only one curve is discernable, there are two present in the figure; (c) A zoom of the previous graph to show the two curves; (d) Analytical (solid) and finite element (dashed) result when the membrane thickness is reduced to 0.2 μm. 71

4.16 A series of TRANS126 elements are used in ANSYS to correctly model a CMUT. 72

4.17 A comparison between the CMUT input impedance results obtained using the piston, distributed, and finite element models. The curves representing the piston and distributed models are identical to the ones shown in Figures 4.8 and 4.11. 73

4.18 Abstract finite element representation of a CMUT placed on a substrate. This particular model is for the sacrificial layer method of device fabrication. A similar one can be made for the wafer bonding method. 74

4.19 Mesh used in the finite element representation of a membrane in air. . 78

4.20 The three curves used to determine the value of the damping coefficient for the membrane material property in Ansys. 79

4.21 Real (solid) and imaginary (dashed) parts of the input impedance of a Lamb wave device consisting of a CMUT on an 8 μm substrate with a 60 μm wide membrane. The short circuit resonance is at 2.73 MHz. . 80
4.22 Membrane displacement of a Lamb wave device consisting of a CMUT on an 8 μm substrate. The frequency of maximum displacement is 2.73 MHz. 81
4.23 Power in the A_0 (solid) and S_0 (dashed) modes along a cross-section of the device. The frequency of maximum Lamb wave coupling is 2.73 MHz. Furthermore, over 95% of the power is in the A_0 mode. . . 82
4.24 Total Lamb wave power showing both first and third order resonances. 83
4.25 Electrical power (solid) into the device and acoustic power (dashed) along a cross-section of the substrate. 84
4.26 Resistance presented to the membrane by the Lamb wave (solid) and A_0 mode (dashed) for 10, 14, 18 and 500 μm substrates. The real part of the air impedance as expressed in (4.6) is also shown as a point of reference. The vertical lines represent the resonant region of the device. 85
4.27 Power coupled into the A_0 mode of the substrate using three different excitation mechanisms. Only the relative value of the different curves is important in this figure. The absolute numbers are a function of the arbitrarily chosen forces applied in the finite element model. 86
4.28 Data in Figure 4.29 is taken along the membrane/substrate interface over the region specified above. 86
4.29 Stresses measured along the membrane/substrate interface as shown in Figure 4.28. (a) T_{xx}, (b) T_{xy}, (c) T_{yy}. 87
4.30 Insertion loss predicted from a transient analysis using FEM. Data is presented for a structure with absorbing boundaries (solid) and without (dashed). 89

5.1 Process steps of the capacitive micromachined ultrasonic transducer manufacturing process using the sacrificial layer method. A single transducer is shown in the picture above. 92

5.2 Stills of the wafer surface after doping 93
5.3 Stills of membrane fingers from two different runs at the beginning of the release process. (a) The finger consists of a single membrane 1 cm long; (b) The finger consists of many small membranes 98 μm long, separated by 2 μm. 94
5.4 (a) Microscope still of membrane breakage; (b) SEM of the same. . . 95
5.5 Process steps associated with thinning the substrate to complete the Lamb wave device. A single transducer is shown in the picture above. 97
5.6 (a) 2-D and (b) 3-D representations of the backside of the fabricated device. Note that the wafer is shown upside down and in this particular instance one membrane is used at the transmit and receive ports. . . 97
5.7 Wafer holder used to protect the front side of a 4-inch wafer during etching. (a) The two halves of the holder; (b) The fully assembled holder. 98
5.8 SEM stills of the fabricated device using the sacrificial layer method. (a) Left side of the device; (b) Front view of the device with the membrane lifted up to expose the gap area and insulation region. 99
5.9 The effect of KOH on chrome/gold electrodes. The pad on the left was chrome/gold over silicon while the one on the right is chrome/gold on silicon nitride. The features on the pad on the right are strips of gold that peeled off of other areas of the wafer. 99
5.10 Process steps of the capacitive micromachined ultrasonic transducer manufacturing process using the wafer bonding method. Two transducers are shown in the picture above. 101
5.11 Process steps associated with thinning the substrate to complete the Lamb wave device. Two transducers are shown in the picture above. . 103
5.12 SEM stills of the (a) left side and (b) right side of the fabricated device using the wafer bonding method. 105
5.13 Sacrificial layer method: real and imaginary parts of the input impedance of two membranes (solid and dashed) that make up a single device. . 106

5.14 Wafer bonding method: real and imaginary parts of the input impedance of two membranes (solid and dashed) that make up a single device. . 106

6.1 Input impedance of a Lamb wave device on a 500 μm substrate with a membrane width of 60 μm, membrane thickness of 1.34 μm, and an air gap of 0.97 μm at a bias of 100 V. 109

6.2 Real part of the input impedance of a Lamb wave device on a 500 μm substrate with a membrane width of 60 μm at various bias voltages. The collapse voltage is 150 V. 110

6.3 Imaginary part of the input impedance of a Lamb wave device on a 500 μm substrate with a membrane width of 60 μm at various bias voltages. The collapse voltage is 150 V. 110

6.4 Experimental setup of the LDV system. The LDV system comprises of the Poltytec-PI OFV-3001 decoder in conjunction with an OVD-30 sensor head. 111

6.5 Input pulse (applied electrically) and membrane displacement (measured optically) on a CMUT that is on an 8 μm substrate with a membrane that is 60 μm wide. The voltage to displacement conversion factor is 50 nm/V. 112

6.6 (a) Step response measured optically using an LDV system. Voltage and displacement conversion factor is 50 nm/V; (b) Fourier transform of step response; (c) Membrane response measured using a CW source as described in the text; (d) Results of (b) and (c) superimposed on each other. 113

6.7 Dimensions of the device described by the data in Figure 6.8. 114

6.8 (a) Displacement of the thinner region of the device pictured in Figure 6.7; (b) Displacement of the thicker region of the device. 114

6.9 Locations along the device substrate where data is taken to create the graph shown in Figure 6.10. 115

6.10 Data obtained at each point marked in Figure 6.10. The top curve is obtained at the point closest to the transmitting membrane. The voltage to displacement conversion factor is 50 nm/V. 116
6.11 (a) Experimental data of the received signal; (b) Zoom in of the received pulse (experimental); (c) Simulated data of the received signal; (d) Zoom in of the received pulse (simulated). 117
6.12 Real part of the input impedance for a single device as it is thinned from 350 μm to 18 μm. 120
6.13 Real part of the input impedance for a single device as it is thinned from 350 μm to 18 μm. 120
6.14 (a) Real and (b) imaginary parts of the input impedance of a device on a 450 μm substrate; (c) Real and (d) imaginary parts of the input impedance of a device on an 8 μm substrate. 121
6.15 Real part of the input impedance with (dashed) and without (solid) epoxy to absorb the reflections. 122
6.16 L-match used for the input impedance graphs shown in Figure 6.18 . 123
6.17 (a) Real and (b) imaginary parts of the input impedance. Both transmit (solid) and receive (dashed) ports are shown without the matching network. 124
6.18 (a) Real and (b) imaginary parts of the input impedance. Both transmit (solid) and receive (dashed) ports are shown with the matching network. 124
6.19 Power loss associated with the matching network for the transmit (solid) and receive (dashed) ports using the impedance data of Figure 6.18 in conjunction with (6.2). 125
6.20 Normalized impulse response spectra of the membranes (solid lines) and the device substrate (dashed line). 126
6.21 Insertion loss of three different Lamb wave devices built using CMUT technology. Details of the device are shown in Table 6.1. 127
6.22 Backside of the Lamb wave device where isopropanol is added for the mass loading experiment. 130

6.23 Received voltage signal showing the effect of mass loading of a Lamb wave device due to isopropanol. The unloaded (solid) and loaded (dashed) responses are shown. 130
6.24 Humidity measurement at 23 ^{o}C. 131

Chapter 1

Introduction

In the late 1960s researchers began to investigate an alternate market for devices built using tools devised for integrated circuit (IC) manufacturing. Through their efforts, and borrowing from the billions of dollars and decades of research invested in IC technology, the field of MEMS was born. The term is a buzzword as well as an acronym for micro-electro-mechanical-systems. In a strict sense it is an umbrella for devices that employ electrical and mechanical components at the micron scale which work together to perform a function. In reality the term is a misnomer, since many devices that are put into said umbrella do not have any electrical components at all, or are comprised of geometries outside of the micron scale (both bigger and smaller). Perhaps a better description of the term is that it encompasses devices built using the tools and techniques developed for the integrated circuit industry. This includes lithography, deposition, and etching, as well as newer techniques developed specifically by and for the MEMS community [47]. The first paper published in this field was in 1982, titled *Silicon as a Mechanical Material* [66].

A common device built using MEMS technology is the electromechanical transducer, a structure defined as one that converts electrical energy to mechanical energy and vice versa. One can think of the transducer as the electromechanical analog of a transformer, which converts energy between the electrical and magnetic domains. One of the more popular electromechanical transducers converts electrical energy to surface acoustic waves (SAW), or Rayleigh waves, which were first described in 1885

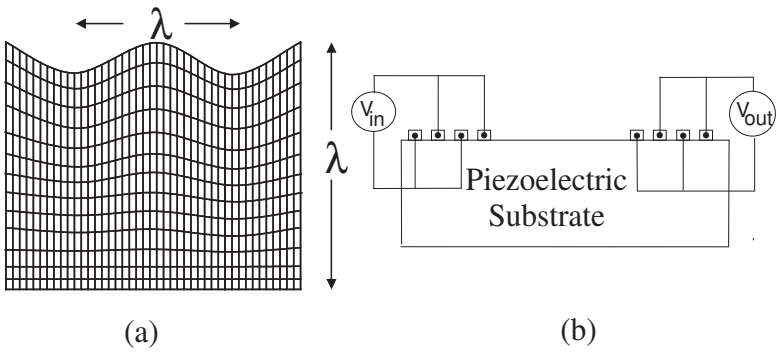

Figure 1.1: (a) Crystal structure supporting surface acoustic waves in a semi-infinite solid; (b)Interdigital transducer formed by patterned electrodes at the surface of a piezoelectric crystal.

by Lord Rayleigh [70]. The SAW device is made up of a crystal where a stress free boundary condition is imposed on the surface. A series of interdigital transducers, formed by patterned electrodes on the surface of a piezoelectric crystal, convert an input electrical signal into the acoustic wave. This wave propagates along the length of the device to a set of receive transducers, which convert energy back into the electrical domain. Figure 1.1 illustrates both the crystal and the device.

The SAW device has applications in two primary arenas. It is best known as a filter, where it is traditionally used in the front end of high frequency communication circuits for both the RF and IF filters (see Figure 1.2). In the former case, the device takes in the broadband signal received by an antenna and only passes on information that is in the band of interest. In the latter case, the device filters out image frequencies coming out of the mixer to pass on the IF signal to the subsequent electronics.

As a sensor, the SAW device can detect a range of phenomena. This range can be greatly enhanced by coating the area between the electrodes shown in Figure 1.1b with materials that undergo changes in mass, elasticity, or conductivity when exposed to different stimuli. For example, a vapor sensor is created when a coating is applied that absorbs specific chemical vapors. One main disadvantage to this technology lies in the fact that atoms of the crystal lattice move in the direction normal to the surface when the Rayleigh wave passes through. This makes SAW devices poorly suited

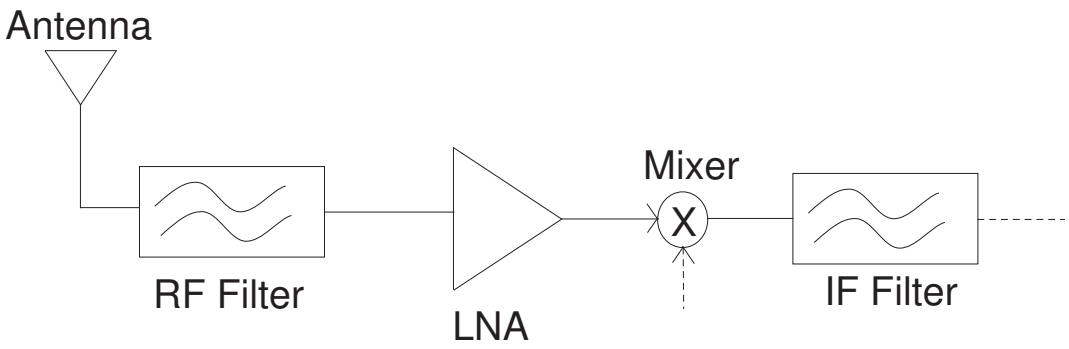

Figure 1.2: Classical front-end topology of a high frequency circuit, consisting of an antenna, radio frequency (RF) filter, low noise amplifier (LNA), mixer, and an intermediate frequency (IF) filter. SAW devices are used to implement the filters.

for liquid sensing, since they excite compressional waves in the liquid that result in excessive attenuation of the signal [10, 21].

A Rayleigh wave is really the high frequency limiting case of a Lamb wave. The shape of a crystal supporting the two possible Lamb wave modes is shown in Figure 1.3. Lamb wave devices operate in the 100 kHz to multiple megahertz range and, in addition to being used as sensors and filters, they have certain advantages over their high frequency counterparts. First, Lamb waves can propagate along a substrate when immersed in water. Even though particle displacement is in the direction normal to the substrate, the low velocity of the acoustic wave precludes it from leaking into its environment. Second, the accompanying electronics necessary for Lamb wave device applications work at lower frequencies than those of SAW devices. They are thus easier to design and cheaper to implement. Finally, the mass sensitivity of a Lamb wave sensor is almost an order of magnitude greater than that of a Rayleigh wave sensor [10]

One property that Lamb wave devices do have in common with those built using SAW technology is that they are primarily built using piezoelectric materials. Many of the more common and efficient of these materials are not compatible with standard IC processes, and therefore integrating them with MEMS devices built with on-chip circuitry presents a challenge. A common solution is to hold off on the introduction

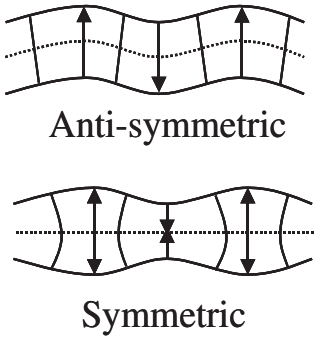

Figure 1.3: Crystal structure supporting anti-symmetric and symmetric Lamb waves.

of piezoelectrics to the wafer until the very last step. While this technique is effective, it significantly limits the options available while manufacturing the device.

This dissertation introduces a new type of Lamb wave device that borrows from the transducer technology of the capacitive micromachined ultrasonic transducer (CMUT). It is built using standard IC processes and does not use piezoelectric materials. Rather, the Lamb wave is excited by a vibrating membrane that transfers acoustic energy into the substrate through its supporting posts. The wave travels along the substrate where it is picked up by a second set of CMUTs and converted back into an electrical signal. The purpose of this research is to investigate the feasibility of using CMUTs to build Lamb wave devices. Numerous methods are used to model its behavior, its manufacturing process is described, and its characteristics are compared to Lamb wave devices built using other methods. This research also sets the stage for future work investigating the fabrication of SAW devices using CMUT technology.

Following this introduction, which makes up Chapter 1, Chapter 2 presents a history of the field in an effort to put the Lamb wave device described here into its proper historical framework. It starts with the study of acoustic waves travelling along a circular cylinder [17, 69], and continues on to the derivations of Rayleigh [71] and Lamb [49, 50]. It then traces through the major advances in Lamb wave theory up to the introduction of direct coupled Lamb wave devices [100]. At this point the

focus narrows exclusively to direct coupled devices and brings the reader to the current state of research in the field.

Chapter 3 uses the concept of capacitive actuation to describes how a CMUT works. It continues with a presentation of first- [42] and second-order [38] models which describe the behavior of the transducer, as well as a brief comment on the manufacturing process of the device. Lamb waves are then introduced, along with a derivation and analysis of the period equation that describes the factors which influence the waves' velocity [1, 96]. Finally, the merging of CMUT and Lamb wave technologies is introduced through an account of the experiment where it was first verified that Lamb waves could be excited by capacitive micromachined ultrasonic transducers [42].

The modeling work performed to describe the capacitive micromachined ultrasonic Lamb wave transducers is the subject of Chapter 4. Three different configurations are described, of which two are analytical. The main difference between them is in the description of the transduction coefficient. In the piston model, the membrane movement acts like a piston; in the distributed model the membrane is allowed its full bending shape. The third model is numerical, rooted in finite element analysis. This is the most accurate of the three (also the most time intensive), and is used to analyze the modal composition of the acoustic wave, make predictions of device efficiency, and understand device behavior in different environments.

The manufacturing method of the device is presented in Chapter 5, where two different process flows are discussed. The first, dubbed the sacrificial layer method, involves the etching of a polysilicon layer underneath a layer of silicon nitride that acts as the transducer membrane. The second is referred to as the wafer bonding method, where a double-side polished prime wafer is bonded to an SOI wafer. A trench etched in the former wafer makes up the gap of the CMUT, while the device layer of the latter wafer acts as the membrane. The wafer bonding method results in higher membrane yield, better repeatability, and shorter fabrication time.

Chapter 6, the final one before the conclusion, describes the characterization of the fabricated devices. It starts by confirming the validity of the electromechanical models derived in Chapter 4. It then verifies that the CMUTs do indeed propagate

acoustic energy, and that this energy is in the form of a Lamb wave. This is followed by an experimental analysis of the factors that determine device efficiency, and the presentation of results from an optimized device. Finally, sensor and filter applications are presented.

Chapter 2

History

The purpose of this dissertation is to introduce a novel direct coupled method for the detection and generation of Lamb waves. Since it acts to both further our theoretical understanding and build on our technological sophistication of these waves, it is important to fit the work described here into its proper historical framework. It is only through this exercise that one can properly understand the contribution of this research to the fields of science and engineering.

This chapter aims to do just that. It begins with the studies of Leo Pochhammer in 1876 and traces the major advances in Lamb wave theory to Richard White's demonstration of direct coupled surface acoustic waves in 1968. The focus then narrows to direct coupled Lamb wave technology and touches on some of the major players in this arena. Since this chapter covers over 150 years of research, the scope of the discussion is very broad. Where deemed appropriate, however, a more detailed description is given.

2.1 1876 - 1917: Basic Formulation

Lamb waves are best described as waves that propagate along an infinite elastic plate with free boundaries. The earliest work done in this field was by Leo August Pochhammer who, in 1876, presented the theory for elastic waves travelling along a

circular cylinder [69][1]. Lord Rayleigh and Sir Horace Lamb chose to follow up this work [49, 71] in 1889 by tackling what Lamb called the "somewhat simpler problem of two-dimensional waves in a solid bounded by parallel planes [50]." Both Rayleigh and Lamb were able to mathematically describe the behavior of the elastic waves from fundamental stress-strain equations and boundary conditions. This description resulted in what they coined the *period-equation*, an expression that could only be solved in the limits of short and long wavelengths. While there was considerable interest in understanding the behaviour of the waves for wavelengths between the two extremes, the two found the equation in this region to be "intractable[2]."

Lamb found a way around the intractibility of the *period-equation* in 1917 and he published his results in the classic paper titled *On Waves in an Elastic Plate* [50]. In his introduction Lamb states that he chose to return to the problem of waves on a plate of rectangular cross section for two reasons. The first was to contribute to elastic theory. He expressed his frustration at being restricted to the study of waves in a rectangular plate in the limit of short and long wavelengths. He also reiterated his sentiments that any advances in the understanding of the wave behaviour in the area between the two extremes would have "some degree of interest." His second reason was to help answer specific questions that had been posed in the field of modern seismology. Significant effort had been put into answering questions relating to waves and vibrations in an elastic medium imagined as resting on matter of a different elasticity and density. He felt that these questions would not be answered unless the *period-equation* could be solved to obtain a practical solution. In the rest of the paper Lamb proposes a solution to the equation and shows how it lends significant insight to the behaviour of waves in an elastic plate. Since the breakthrough described by Lamb in this paper set the stage for all future work in this field, it is important from a historical perspective to understand the problem he faced and the technique with which it was solved.

Equation (2.1) presents the *period-equation* for symmetric waves as it was written

[1]According to [46] the general elastic equations describing this problem were investigated independently by Chree [17] in 1889.

[2]The Mirriam-Webster definition of *intractable* is: 1. Not easily governed, managed, or directed; 2. Not easily manipulated or wrought.

in Lamb's paper.

$$\frac{\tanh \beta f}{\tanh \alpha f} = \frac{4\xi^2 \alpha\beta}{\left(\xi^2 + \beta^2\right)^2} \tag{2.1}$$

The variable ξ is the wave number $\frac{2\pi}{wavelength}$, and the quantity $2f$ denotes the thickness of the plate. The variables α and β, also presented in the same form in which they were printed in Lamb's paper, are defined below where λ and μ are the Lamé constants, ρ is the plate density, and σ is the wave frequency in units of radians/second.

$$h^2 = \frac{\rho\sigma^2}{\lambda + 2\mu} \tag{2.2}$$

$$k^2 = \frac{\rho\sigma^2}{\mu} \tag{2.3}$$

$$\alpha^2 = \xi^2 - h^2 \tag{2.4}$$

$$\beta^2 = \xi^2 - k^2 \tag{2.5}$$

The problem encountered by Lamb and Rayleigh in their efforts to solve (2.1) is that they concentrated on solving for the wave frequency σ when given its wavelength. This was not possible due to the fact that frequency and wavelength are a factor in virtually every term of the equation. The solution Lamb came up with was to instead solve for the wavelength corresponding to a given wave velocity. The key to his method was to relate the variables α and β through a constant m ($\beta = m\alpha$). He used this equivalence to combine (2.4) and (2.5) into

$$\xi^2 = \frac{k^2 - m^2 h^2}{1 - m^2} \tag{2.6}$$

through which the velocity (V) can be written solely as a function of the variable m and constants λ, μ, and ρ:

$$V^2 = \frac{\sigma^2}{\xi^2} = \frac{k^2}{\xi^2}\frac{\mu}{\rho} = \frac{(\lambda + 2\mu)\left(1 - m^2\right)}{\lambda + 2\mu - m^2\mu}\frac{\mu}{\rho}. \tag{2.7}$$

In the limit of incompressible plate materials ($\lambda = \infty$, $h = 0$, and $\alpha = \xi$), this

equation becomes

$$V^2 = \left(1 - m^2\right) \frac{\mu}{\rho}. \tag{2.8}$$

Furthermore, defining a new variable ω as equal to the product of the wave number (ξ) and half the plate thickness (f), Lamb simplified the *period-equation* to that shown in (2.9).

$$\frac{\tanh m\omega}{\tanh \omega} = \frac{4m}{(1 + m^2)^2} \tag{2.9}$$

By analyzing the roots of (2.8) and (2.9) and using tables of hyperbolic and circular functions distributed by the Smithsonian Institution of Washington D.C. in 1909, Lamb was able to use (2.9) to relate a wave's velocity to its wavelength through the variable ω.

Using this method of simplifying the "intractable" equation by introducing the variable m, Lamb went on to perform a similar calculation for anti-symmetric waves and later showed that the problem could also be solved for both types of waves without the assumption of an incompressible plate material.

With a solution to the *period-equation* in hand, Lamb described the major features of these elastic waves. He showed that there are an infinite number of symmetric and anti-symmetric modes, described their dispersive behavior, and gave a mathematical formulation of the plate's particle displacement over the thickness of the plate. The latter point was of special interest because it showed that unlike Rayleigh waves, which were well understood at the time, the amplitude of the Lamb wave field does not decrease along the depth of the plate.

2.2 1922 - 1951

2.2.1 Theory Extension

The theory of elastic waves on rectangular plates was extended in 1922 by Professor Stephen Timoshenko in two different papers published while he was teaching at Zagreb Polytechnic [86, 87]. The purpose of his work was to include a "correction" [86] in the describing equations for the presence of rotary inertia and shear. His final expressions

showed that the correction for shear was four times as important as the correction for rotary inertia. More importantly, however, he demonstrated that neither correction is important if the wavelength of the transverse vibrations is large in comparison to the dimensions of the plate cross-section. This result will be the foundation of an important assumption later on in this dissertation.

2.2.2 Wedge Method of Excitation

An important feature of these waves that was not touched on by Lamb is the ability to couple to them through a medium such as air or water. This revelation was presented in 1938 by Professor Hans Reissner while teaching at Berlin's Technische Hochschule in the civil engineering department [72]. Specifically, he described the conditions of the transmission of energy through water into a plate in terms of the wave's angle of incidence, the physical constants of the plate material, and the ambient liquid. This technique to excite waves in a plate was later coined the *wedge method* [96]. Reissner showed that at a given frequency there are at least two angles of incidence for which the wave can be excited in a plate. His formulation was based on the condition of phase-velocity coincidence. This principle states that a plate wave will be excited by an incident sound wave when the component of the phase velocity of the sound wave in the direction parallel to the free boundary equals the natural phase velocity of a free wave along the plate.

2.2.3 Reflections In The Plate

Reissner's theory was verified by F.H. Sanders [76] in 1939 and later simplified by J. Götz [40][3] in 1943. Both Sanders and Götz analyzed their data under the assumption of infinite plate area; while their results were qualitatively consistent with theory, they were not numerically consistent with the experimental error [23]. In order to resolve this error, Fay and Fortier performed over 16,000 experiments in 1951 in order to track down its source. They found that the differences between theory and

[3]This was later translated by C.E. Morgan, Jr. in February 1947. The source, according to Fay and Fortier[23], is *Nav Ships 900.138.*

experiment were due to reflections from the plate boundary. As a result they modified Reissner's condition of phase-velocity coincidence to include the effect of successive reflections from the plate edges [23].

2.3 1945 - 1957

2.3.1 Propagation Along A Plate In Water

Once the acoustic energy is coupled into the plate through an ambient liquid it will propagate along the structure. This is a problem slightly different from that studied by Lamb due to the fact that the two parallel planes of the plate are no longer free but rather border an infinite liquid. This so-called waveguide problem was dealt with in 1945 by M.F.M. Osborne and S.D. Hart where they derived the *period-equation* for this situation [64]. Their resulting expressions are strikingly similar to those of Lamb; the only difference is the modification of one term to account for the presence of water. Their more important result, however, is the fact that the water around the plate results in a minimal level of attenuation.

2.3.2 Experimental Verification Of Dispersion

One of the more obvious characteristics of Lamb waves, and one of the easiest to experimentally verify, is their dispersive nature. The comparison of the actual Lamb wave velocity to that predicted by the describing equations, was first done for cylindrical rods qualitatively in 1931 by Röhrich [74] and quantitatively in 1940 by Shear and Focke [80]. Both efforts compared their results to the rudimentary theories of Leo Pochhammer [69]; the results did not match since Pochammer's equations were not sophisticated enough to properly model the experiments in question. It was therefore not until the early 1940s when Bancroft [11] and Hudson [37] derived exact equations that the results were brought into agreement with theory.

Experimental confirmation of the dispersive nature of lower order modes in plates of rectangular cross-section was first reported by R.W. Morse in 1948 [60]. He performed his experiments in the 200 to 650 KHz range using brass plates coupled to a

driving crystal by an oil film. It is worth noting that he repeated his measurements for circular rods and obtained results that matched well with those predicted by Bancroft.

Morse's work is well complemented by the research of Ivan Tolstoy and Eugene Usdin [93]. In addition to a detailed description of the group velocity of the waves along a rectangular cross-section, they verified the dispersion relationship of many of the wave's higher order modes (up to the fiftieth). During the course of their research they also noted that by using the proper phase relations between two sources on opposite sides of the plate, one could selectively excite either the symmetric or anti-symmetric mode. The details of this discovery are alluded to in [93] but were first reported in [22].

2.4 1961 - 1965

2.4.1 Experimental Confirmation In The Megahertz Range

By the mid-1950s Lamb waves had found their way into the mainstream. The ultrasonic inspection of materials used to be performed solely with longitudinal and transverse waves. Because these waves were not suitable for the inspection of thin-walled materials (less than 5 mm), the samples were instead tested by other nondestructive testing methods such as magnetic, x-ray, and luminescent inspection. With the introduction of this new wave type, the geometrical restrictions were lifted and it became possible to inspect structures greater than 0.3 mm [96]. Furthermore, Lamb waves also found significant use in ultrasonic solid delay lines. The delay lines were made of plates of fused silica and were generally used as storage elements in radar and computer circuitry [84]. Finally, the propagation of sound through a plate bounded by stress-free parallel planes had become a standard method of waveguide transmission.

Perhaps in response to the commercialization of Lamb wave devices into products, scientists quickly began to push the limits of their operating frequency. In 1961 D.C. Worlton extended the experimental confirmation of the wave's theoretical studies into the Megahertz range [102]. This confirmation is particularly relevant to the devices

described in this dissertation because they operate in the same frequency range as those tested by Worlton. For this reason Worlton's experiments are presented in detail below.

In his paper Worlton described three experiments. The first involved the coupling of a Lamb wave[4] at 5 MHz to a 0.051 inch aluminum plate submerged in water. Of particular interest was the angle of incidence necessary to couple energy of a specific mode into the plate. Worlton excited seven modes (the symmetric and anti-symmetric modes of the first three orders and the fourth order symmetric mode) and the angle of incidence matched those predicted by theory. For reference, the figure printed in his paper is reproduced in Figure 2.1.

In his second experiment Worlton measured the velocity of various Lamb wave

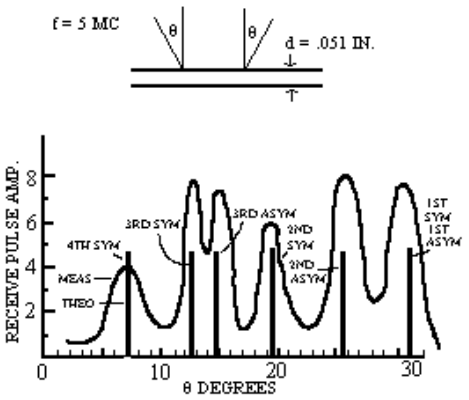

Figure 2.1: Theoretical and measured Lamb waves in an aluminum plate from Worlton [102].

modes at different frequencies as they travelled down plates of various thicknesses. He superimposed his results on top of the theoretical velocity curves and showed that they agreed very well. This experiment verified the dispersive nature of the waves, the cutoff frequency of the different modes, and the quantitative values predicted

[4]In a footnote in this paper Worlton sheds some light on the etymology of the phrase "Lamb wave:": "[F.A.] Firestone and [D.S.] Ling have, in particular, done much to elucidate the theory from an ultrasonic testing standpoint. Firestone coined the phrase 'Lamb waves' to describe the wave motion theoretically postulated by Lamb." The source cited by Worlton is a technical report (No. 50-6001) from Sperry Products, Inc. written by Firestone and Ling; attempts to find this report were not successful.

by the theoretical equations. His third experiment verified that in the limit of large frequency-thickness products the waves act like Rayleigh waves.

D.C. Worlton also added to the theoretical framework of Lamb waves by exploring the difference between symmetric and anti-symmetric modes. By building on Lamb's expressions he derived both the horizontal and vertical particle displacement equations and presented a mathematical formulation of their ratios. In comparing his results to experiment, Worlton showed that the relative rate of wave attenuation as it travels down the plate can vary significantly depending on the order of the mode. Specifically, modes that have a large vertical to horizontal displacement ratio will attenuate more rapidly. The explanation he proposed for this phenomenon is that horizontal particle motion will radiate energy to the water at a very slow rate since liquids do not support a shearing motion. Conversely, modes that vibrate primarily in the vertical direction drive the liquid in a manner similar to a piston vibrator and therefore impart energy to the water very quickly. The graphs presented in his paper show that the minimum attenuation is obtained for what he called the first symmetric and anti-symmetric modes (referred today as the zeroth order modes).

2.4.2 Four Basic Methods of Exciting Lamb Waves

By the mid-1960s most of the fundamental theory of Lamb waves had been presented and experimentally confirmed. The efforts of researchers therefore shifted from trying to understand Lamb wave behaviour to exploring different methods for their excitation and reception. In 1965 there were two basic categories of Lamb wave excitation: the creation of disturbances on the surface of the plate and the creation of disturbances inside the plate or at the ends. In almost all cases the methods in the former category were used because they were much simpler to realize. Within this category are the four basic methods described by I.A. Viktorov in his review paper on Lamb waves [96]. They are described below and are illustrated in Figure 2.2:

a. Shear disturbances uniformly distributed on the surface of the plate in a band of fixed width. The disturbances are produced by a Y-cut quartz plate or a titanium plate with the appropriate polarization.

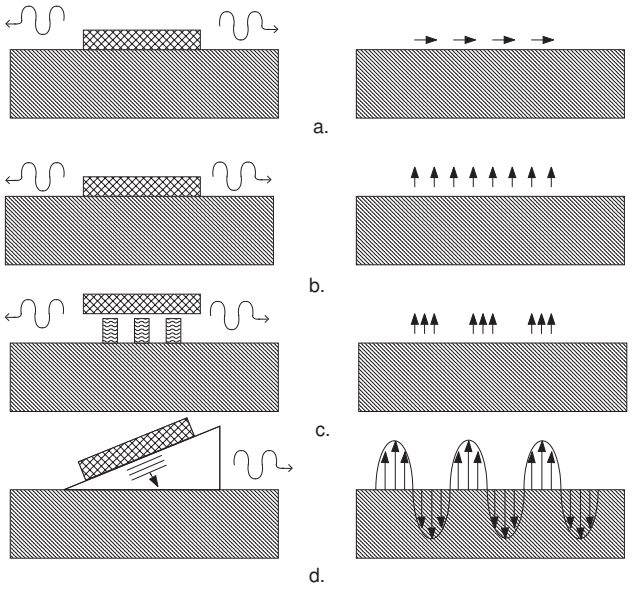

Figure 2.2: Four primary methods of Lamb wave excitation as described by Viktorov. See text for a description of the figures.

b. Normal disturbances uniformly distributed on the surface of the plate. The disturbances are produced by quartz or titanate plates acoustically coupled through a coupling variant or by an ultrasonic beam normally incident on the plate through an immersion variant.

c. Normal disturbances distributed periodically over the surface of the plate with a spatial period equal to the excited Lamb wavelength. This method has been coined the *comb method*.

d. Normal disturbances distributed according to the law of a sinusoidal travelling wave over the surface of the plate in a band of fixed width. Once again a coupling or immersion variant could be used; in either case the disturbances are accomplished by sending in the energy at an oblique incidence to the plate. This method is best known as the *wedge method* and was described in Section 2.2.2.

Note that in each of the four cases the excitation of Lamb waves works in a similar way in that they involve the mechanical coupling of a compressional or shear wave transducer to the body on which the surface waves are to propagate. Of these four methods, only the latter two exhibit resonant behaviour. By varying the distance

Theoretical Studies

Authour(s)	Year	Description	Ref.
Hattunen and Luukkala	1973	Study of generalized Lamb waves	[34]
Plona, Behravesh, and Mayer	1975	Lamb waves at liquid/solid boundaries	[67]
Auld and Tan	1977	Scattering at a pair of thin slots	[6]
Rokhlin	1980	Lamb wave diffraction by cracks	[75]
Diodati, Tassi, and Alippi	1985	Lamb wave reflections at plate edges	[20]
Adler	1985	Analysis of composite structures	[2]
Lamb Wave Applications			
Ball and Shewring	1976	Non-Destructive Testing	[9]
Bendec, Peretz, and Rokhlin	1984	Sizing spot welds	[12]
Palma et al.	1985	Voltage Sensing	[65]
Wu et al.,	2002	Sensing using optical transduction	[103]
Direct Coupled Devices			
Tirole et al.	1993	AlN/Si piezo structure	[88]
Joshi	1996	Electronically variable time delay	[44]
Fischer et al.,	2000	Lamb wave on native silicon	[24]

Table 2.1: Select work done in the field of Lamb waves.

between the tines of the comb profile or the wedge angle, any of the possible plate modes can be excited or received.

2.5 1970 - Present

The work done on Lamb waves since 1970 is difficult to catalog because of its sheer volume. Perhaps the greatest indication of the growing popularity of Lamb waves and their devices is their appearance in textbooks; by the mid-1970s they were being discussed alongside Rayleigh waves [1, 5, 28, 46, 56]. The landmark advance in Lamb wave technology during this time period was White's discovery of direct coupled acoustic waves. The sections below discuss this discovery as well as a few of the major projects involving direct coupled Lamb wave devices. Select others are listed in Table 2.1 along with other relevant Lamb wave papers.

2.5.1 A Fifth "Basic" Method: Direct Coupling

A revolutionary advance in Lamb wave transduction came in 1970. Richard White, a professor at the University of California, Berkeley, showed that acoustic waves could be excited on plates using photolithographically patterned and spatially periodic electrodes on the plane surface of a piezoelectric plate [100]. This method is described as "direct" because unlike the four mechanisms described above, the coupling of an external transducer is not needed to excite and receive the surface waves. This therefore precludes the use of contact pressure from the transducer and thus avoids surface damage to the device. Other advantages of this method include the fact that the transducer can be easily handled and precisely fabricated, and that it may be operated at extreme temperatures or in a vacuum. While White's experiments were performed for surface acoustic wave (SAW) devices at 15 and 45 MHz, his method is also applicable to Lamb wave devices.

2.5.2 The First Direct Coupled Lamb Wave Devices

The first person to apply White's direct coupling method to Lamb waves was Professor Kohji Toda of the National Defense Academy in Japan. In a series of papers in the early 1970s, Toda demonstrated and explained the piezoelectric coupling of plate modes to Lamb waves using interdigital transducers (IDTs). In his first report, published in 1971, Toda describes a Lamb wave device built on an un-polarized PZT ceramic plate excited by an interdigital arrangement of transducer electrodes [89]. In addition to exciting the Lamb waves, these electrodes are used to apply the necessary polarizing treatment to the piezoelectric material. Using four different groups of electrode configurations with different finger dimensions along with results of the Schwartz-Christoffel transform, Toda showed that the optimal electrode spacing is one-half of a wavelength. Using this spacing in a delay line configuration, Toda verified the equations relating the Lamb wave phase velocities and studied the attenuation, reflection, and equivalent circuit of this new method of wave transduction.

In 1974 Toda published his second paper which analyzed the frequency characteristics of IDTs for Lamb wave excitation [90]. Specifically, he was interested in the

frequency dependance on the surface displacement of the total number of electrode fingers and their configurations. Borrowing concepts once again from surface acoustic wave theory to build his model, Toda built on work by Tseng [94] for his analysis. The resulting equations correctly predicted his earlier observations that an increasing number of transmitting electrodes result in a larger output amplitude and a smaller fractional bandwidth.

Toda followed up this initial work on the theory and fabrication of direct coupled Lamb wave devices with a plethora of studies on their applications. Examples of these applications include the determination of static tensile stress on the plate upon which the Lamb wave is traveling [91], the amplitude modulation of signals [81], and the fabrication of a ternary logic communication system [92].

2.5.3 Direct Coupled Lamb Wave Devices as Sensors

Many researchers picked up on Toda's work in an effort to both optimize direct coupled Lamb wave devices and to find applications in which they would be useful. One of the biggest arenas in which the potential of these devices was being explored was that of sensors. The ground breaking work in this field was performed by Stuart Wenzel and Professor Richard White as part of Wenzel's doctoral research at the University of California, Berkeley. As described in their first paper on this topic [101], the motivation behind Lamb wave sensors is that the devices operate at a low frequency range where inexpensive electronic components are readily available. These components could be used, for example, to build an amplifier for the feedback loop of a Lamb wave oscillator. By monitoring the frequency of this oscillator the effects of various stimuli on the Lamb wave device could be sensed. The authors expected that the fractional frequency shift caused by changes in certain stimuli could be an order of magnitude higher for an A_0 or S_0 mode oscillator than for that of a SAW device. Another selling point of a Lamb wave sensor was the fact that it could be immersed in a liquid. This characteristic links to the findings of Osborne and Hart described above; because of relative velocities of sound in the plate and in liquids, the slow A_0 waves on a plate immersed in liquid will not radiate into their environment.

The frequency changes of a Lamb wave oscillator are caused by changes in the wave velocity as it propagates from the transmitting membranes to the receiving ones. The velocity is in turn affected by changes in the plate's in-plane tension, stiffness, mass per unit area, and rotary inertia caused by the presence of the particular stimulus the sensor is being used to detect. As a result, it is important to fully understand the dispersion relation for the A_0 mode in terms of the various plate characteristics. This derivation was performed by Wenzel [98, 99] and the predictions of the resulting equation were shown to agree well with the actual sensor response.

Wenzel's experiments included chemical vapour tests with polymer-coated membranes, density measurements with low-viscosity liquids, measurements of the absolute pressure of helium gas, and measurements of the viscosity of glycerol-water solutions. The device used in these experiments were primarily piezoelectric ZnO/Al/Silicon Nitride structures. Other applications of Wenzel's devices, investigated by his colleagues Richard Moroney and Professor Roger Howe, include fluid motion [57], the microtransport of particles [59], and the fabrication of ultrasonic micromotors [58].

2.5.4 Combining Direct Coupled Devices With Integrated Circuits

Wenzel's research, completed in 1992, focused primarily on the delay line aspects of the Lamb wave sensor. In 1994 Professor Michiel J. Vellekoop, then at the Delft University of Technology, published his work on both the oscillator in the feedback loop of the sensor and his efforts to put both components into a single chip [95]. His research required the marriage of three fields: bipolar IC technology, thin-film piezoelectric zinc oxide technology, and micromachining technology. Furthermore, the latter two had to be IC compatible so as to prevent malfunction of the electronic circuitry. The dimensions of his delay line are 3 mm by 8 mm, the oscillator chip size is 10 mm by 10 mm, and his device yield is 76%. The insertion loss of the completed device is around 30 dB.

2.5.5 Direct Coupled Devices Without Piezoelectric Agents

While piezoelectrics have been the most commonly used materials in direct coupled Lamb wave devices, significant effort has been put into finding alternate agents to aid in coupling to the acoustic mode. The reason for this is that the manufacturing process is significantly more complicated when piezoelectrics are combined with either IC or MEMS technologies. Alternative direct coupled methods include electrostrictive, electrostatic, and magnetic methods.

In his doctoral dissertation Wenzel [98] described an electrostrictive Lamb wave device built using rudimentary micromachining techniques. The structure consists of aluminum electrodes sandwiched around .15 μm of silicon nitride. In the presence of an electric field the electrodes squeeze the nitride causing vertical strain. Through the Poisson effect this strain is coupled to lateral strain which excites a Lamb wave along the substrate. Wenzel reported successful generation of the A_0 mode with this configuration.

In 1993 Giesler and Meyer [26, 27] from the Fraunhofer Institute for Biomedical Engineering in Germany reported the fabrication of an electrostatic transducer that could be used to couple Lamb waves along a silicon nitride membrane. The structure is effectively that of a capacitor where one electrode is on a Pyrex substrate and the other is on a 1.5 μm silicon nitride membrane positioned 6 μm away. The thin membrane vibrates in response to an applied AC signal and a Lamb wave is thus launched along the membrane. Using a microcontroller and a direct digital synthesis circuit they were able to minimize thermal and pressure dependant drifts when their device was wired up as a delay line oscillator.

A third type of direct coupled Lamb wave device that does not use piezoelectric materials is the magnetic structure built by Stephen Martin et al. from the Sandia National Laboratory [53]. The key to their structure is a set of meander-line current conductors patterned on the surface of the membrane. The lines run across the width of a thin membrane and are positioned at regular intervals along the length of the surface. When a static in-plane magnetic field is applied perpendicular to the current direction, a surface-normal Lorentz stress is generated. This stress results in the launching of a Lamb wave along the membrane. The insertion loss of this device is

around 23 dB.

2.5.6 Capacitive Micromachined Ultrasonic Lamb Wave Transducers

This dissertation introduces yet another type of direct coupled Lamb wave device. The key technology employed here is the capacitive micromachined ultrasonic transducer (CMUT). Described in more detail in Chapter 3, the CMUT is a capacitor where one electrode is a highly doped region at the top of the silicon substrate and the other is the metal layer on a suspended membrane. When an AC signal is superimposed on top of a DC bias, the membrane vibrates resulting in the movement of the posts that support said membrane. This movement couples energy into the substrate in the form of a Lamb wave. Similarly, when a Lamb wave approaches a CMUT under static bias, the membrane will vibrate resulting in an AC signal that can be delivered to the receiving electronics.

The main advantage that CMUT technology lends to Lamb wave devices over the traditional piezoelectric method is that the manufacturing method is fully IC-compatible. As such, it avoids the complications associated with combining multiple technologies in a single process flow. It also lays the groundwork for an integrated chip containing both a sensor and its accompanying electronics. Relative to other non-piezoelectric devices, this one has similar dimensions and a competitive insertion loss (16 dB). Its innovation is the subject of this dissertation and in a large part the result of much of the work described in this chapter.

Chapter 3

Fundamentals: The CMUT and Lamb Waves

This chapter serves as an introduction to both the Capacitive Micromachined Ultrasonic Transducer (CMUT) and Lamb waves. The CMUT is the vehicle of transduction for the Lamb wave devices described in this dissertation. Lamb waves, as explained in the previous chapter, are best described as waves that propagate along an infinite elastic plate with free boundaries. The sections that follow begin with an introduction to the CMUT, a presentation of first and second order models that describe its behaviour, and a comment on its manufacturing process. An overview of acoustic waves is then given after which the focus narrows to Lamb waves. The equations that govern their propagation is presented along with a qualitative description of the waves' behaviour. The chapter ends with a discussion of the experiment that first demonstrated that CMUTs could be used to couple energy into a Lamb wave.

3.1 CMUTs

As shown in Figure 3.1, there are three main ways to actuate a capacitive transducer. The CMUT and most other air-coupled capacitance transducers [52, 77] employ the method illustrated in Figure 3.1(a.1) where the distance between the plates is varied as a function of time. The invention of the CMUT was reported in 1994 [30] by Matthew

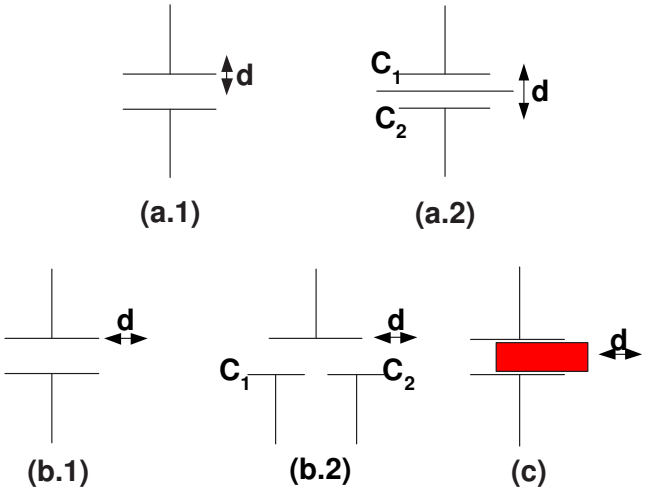

Figure 3.1: Four different ways in which to actuate capacitive transducers after [18, 47]. (a.1) The distance between the plates is varied; (a.2) An intermediate plate is moved relative to two fixed plates for use in differential measurements; (b.1) Overlap of the plates is varied with position; (b.2) Overlap of the plates is varied with position for use in differential measurements; (c) The dielectric constant between the plates is varied.

Haller who performed this research as part of his doctoral dissertation under the direction of Professor B.T. Khuri-Yakub at Stanford University. It has traditionally been used to send and receive ultrasound in air and in water and has found applications in non-destructive evaluation [32], ultrasound imaging [63], microfluidics [41, 55], and acoustic sensing using optical and radio frequency detection [29, 33].

The diagram of an example single CMUT cell is shown in Figure 3.2. The device consists of a capacitor where one electrode is a highly doped region at the top of the silicon substrate and the other is the metal layer on a suspended membrane. When a static voltage is placed between the two electrodes, the membrane is attracted to the substrate by Coulombic forces. When an AC voltage is superimposed on top of the DC potential, the membrane will move in response to the signal and an ultrasonic wave is generated and launched into the environment (this could be the surrounding fluid or the substrate). Likewise, if under DC bias an ultrasonic wave approaches the membrane, it will vibrate and an output AC voltage can be measured from the device electrodes. The applied DC bias is necessary because it supplies the charge that is

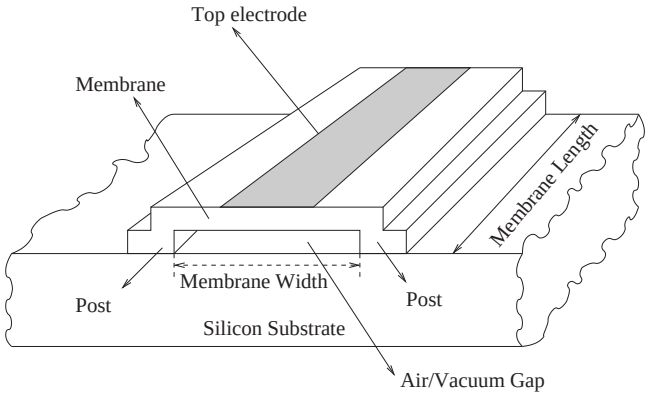

Figure 3.2: Diagram of an example CMUT membrane.

modulated by the membrane movement to create an AC signal. Figure 3.3 shows a simplified model of the CMUT in both transmit and receive configurations.

3.1.1 First Order Model

An analysis of the first order model of a CMUT gives significant insight into the behaviour of the transducer under static bias. Specifically, it sheds light on the phenomena of membrane collapse and spring-softening. The model under a static bias voltage can be derived from the sum of forces placed on the membrane [42, 48]. In addition to the electrostatic force brought about by the DC bias, there is a concurrent force due to the mass of the membrane and an opposite force resulting from its residual stress. Assuming that the membrane's restoring force is a linear function of its displacement, that the parallel plate approximation holds, that the CMUT operates in a vacuum, and that all fringing fields can be neglected, one can represent the transducer by the lumped electro-mechanical model of Figure 3.4 [42]. In this figure, the mass represents the mass of the membrane, the capacitor models the electrostatic force, and the spring accounts for the restoring force of the membrane. Since the sum of forces at equilibrium in any system is zero (d'Alembert's principle):

$$F_{mass} + F_{cap} + F_{spring} = 0. \tag{3.1}$$

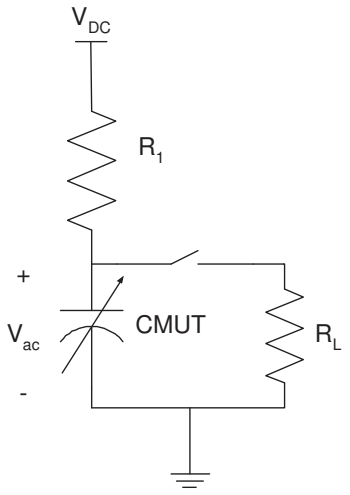

Figure 3.3: When the switch is open, the CMUT is in transmit mode; when it is closed, it is in receive mode and feeds the load R_L.

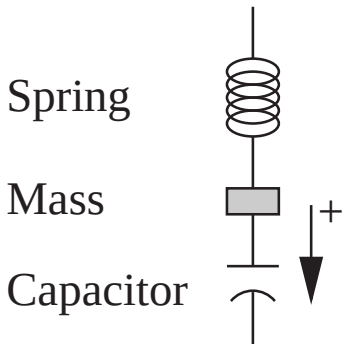

Figure 3.4: Lumped first order model of a CMUT.

The force exerted by the capacitor can be found by applying the principal of virtual work to the basic capacitor equations. Assuming once again that the capacitor is under an applied voltage V with a plate area A, static plate separation d_0, AC plate separation $u(x,t)$, and a dielectric with permittivity ϵ, the force is obtained from the derivation in (3.2) - (3.4). In these equations C represents the capacitance, E is the electric field, and F is the force on the electrodes.

$$C = \frac{\epsilon A}{d_0 - u(x,t)} \tag{3.2}$$

$$\begin{aligned} E &= \frac{1}{2}CV^2 \\ &= \frac{1}{2}\frac{\epsilon A}{d_0 - u\left(x,t\right)}V^2 \qquad (3.3) \\ F &= -\frac{dE}{du} \\ &= \frac{1}{2}V\left(t\right)^2\frac{\epsilon A}{\left(d_0 - u\left(x,t\right)\right)^2} \qquad (3.4) \end{aligned}$$

The force exerted by the mass is simply $F_{mass} = ma$ and the restoring force of the spring is $F_{spring} = -ku$. Substituting these expressions into (3.1) results in

$$\begin{aligned} ma + \frac{1}{2}V\left(t\right)^2\frac{\epsilon A}{\left(d_0 - u\left(x,t\right)\right)^2} - ku\left(x,t\right) &= 0 \\ m\frac{d^2\left(u\left(x,t\right)\right)}{dt^2} + \frac{1}{2}V\left(t\right)^2\frac{\epsilon A}{\left(d_0 - u\left(x,t\right)\right)^2} - ku\left(x,t\right) &= 0 \qquad (3.5) \end{aligned}$$

Since the purpose of this exercise is to find the response of the device under static DC bias, the time dependance in the voltage and displacement terms in (3.5) disappears and the first term in the equation simplifies to zero. This results in

$$ku\left(x\right) = \frac{\epsilon AV^2}{2\left(d_0 - u\left(x\right)\right)^2} \qquad (3.6)$$

which has two distinct regions of interest for different applied bias voltages. Below a certain voltage level, the solution to (3.6) has three real roots of which only one has physical significance. As the applied voltage is increased, the electrostatic and gravitational forces on the membrane surpass the restoring force created by the residual stress on the membrane and the structure experiences *membrane collapse*. The happens when the membrane deflection is one-third of the total gap thickness. Plugging $u = \frac{d_0}{3}$ into (3.6) and solving for V yields

$$V_{collapse} = \sqrt{\frac{8kd_0^3}{27\epsilon A}} \qquad (3.7)$$

While an increasing bias voltage brings the CMUT membrane towards the substrate and thus closer to collapse, it also acts to create a phenomenon called *spring softening*. This term is used to describe the decrease of the resonant frequency of the membrane for increasing DC bias voltages. Qualitatively, this occurs because of the interplay between the electrostatic force on the capacitor and the restoring force of the membrane. When the applied DC voltage increases, the top electrode will move in the positive direction which will result in a membrane force in the opposite direction. Since the two electrodes are now closer together the electrostatic force will be even greater, displacing the membrane even more in the positive direction. This increase in force can also be interpreted as a decrease of the spring constant – a *softening* of the spring. This phenomenon can qualitatively be understood by going back to (3.5) and performing a Taylor Series expansion of the (middle) term representing the electrostatic force of the capacitor around the point[1] $u(x,t) = u^*$ brought about by an applied bias voltage V^*:

$$m\frac{d^2\left(u\left(x,t\right)\right)}{dt^2} + \frac{1}{2}V^{*^2}\frac{\epsilon A}{\left(d_0-u^*\right)^2} + V^{*^2}\frac{\epsilon A}{\left(d_0-u^*\right)^3}\left(u\left(x,t\right)-u^*\right) - ku\left(x,t\right) = 0 \quad (3.8)$$

$$m\frac{d^2\left(x\left(t\right)\right)}{dt^2} + V^{*^2}\frac{\epsilon A}{\left(d_0-u^*\right)^2}\left(\frac{1}{2}-\frac{u^*}{d_0-u^*}\right) - \left(k - V^{*^2}\frac{\epsilon A}{\left(d_0-u^*\right)^3}\right)u\left(x,t\right) = 0 \quad (3.9)$$

This equation can be rewritten in the familiar form of (3.5),

$$m\frac{d^2\left(x\left(t\right)\right)}{dt^2} + \frac{1}{2}V^2\frac{\epsilon A}{\left(d_0-u^*\right)^2}\left(1-\frac{2u^*}{do-u^*}\right) - k_{soft}u\left(x,t\right) = 0 \quad (3.10)$$

where

$$k_{soft} = k - V^{*^2}\frac{\epsilon A}{\left(d_0-u^*\right)^3} \quad (3.11)$$

[1]Note that previous derivations on this subject [42, 48] performed the linearization around the point $u(x,t) = 0$. Since spring softening is brought about by membrane deflection with its accompanying applied DC voltage, the Taylor Series expansion here is done around the value of membrane deflection u^* brought about by a voltage V^*.

Thus, the spring constant k has been decreased by a term proportional to the DC voltage applied to the CMUT.

This first order model can also be used to analyze the forces that are applied to the membrane in response to both DC and AC bias voltages. Assuming $d_0 \ll x$ and $\mathrm{V} = V_{DC} + V_{ac}$, (3.4) can be simplified as

$$\begin{aligned} F &= \frac{1}{2}V^2 \frac{\epsilon A}{\left(d_0 - u\left(x,t\right)^2\right)} \\ F &\alpha V^2 = \left(V_{DC} + V_{ac}\right)^2 \qquad (3.12) \\ F &\alpha V_{DC}^2 + 2V_{DC}V_{ac} + V_{ac}^2 \, . \qquad (3.13) \end{aligned}$$

The three terms in (3.13) correspond to the DC, first, and second harmonics, respectively. Since CMUTs are usually operated at their first harmonic, $F_{small-signal} = 2V_{DC}V_{ac}$.

3.1.2 Second Order Model: Small Signal Equivalent Circuit

An equivalent circuit that describes the behaviour of the CMUT due to small signal excitation is shown in Figure 3.5 and is based on the standard equivalent circuit for a transmitting electro-mechanical transducer [38]. The schematic of a receiving transducer is identical to this one except that the AC source appears on the mechanical

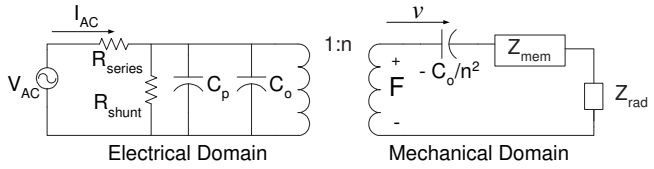

Figure 3.5: Equivalent circuit model of a transmitting CMUT.

side of the circuit and a load takes the place of the voltage source in the electrical domain. The input for the circuit in Figure 3.5 is an AC voltage source V_{ac} from which the source current I_{ac} is pulled. On the mechanical side of the circuit, the voltage is transformed from the electrical domain using a transformer with turns ratio n to a force labeled F. This force is defined to be uniform over the surface of the membrane. The velocity that results, v, is defined as the average velocity over the width of the

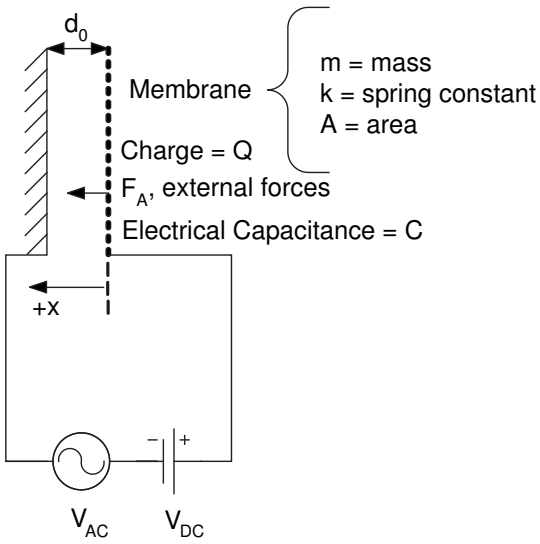

Figure 3.6: Diagram for a generic electromechanical transducer, after [38].

membrane. While specifics regarding the various circuit elements will be described in detail in Chapter 4, a derivation of the model is presented below.

The derivation begins with an expansion of the first order model of the CMUT to include small signal effects. This is done by applying the same approach described in Section 3.1.1 in conjunction with the schematic for a generic electromechanical transducer shown in Figure 3.6 [38]. First, consider the equation of motion of the membrane presented in (3.5) but modified below to include the presence of an external force F_A. Once again explicit mention of the temporal and spatial dependance of u has been left out:

$$\begin{aligned} m\ddot{u} + \frac{1}{2}V^2\frac{\epsilon A}{(d_0-u)^2} - ku &= F_A \\ m\ddot{u} + \frac{Q^2}{2\epsilon A} - ku &= F_A\,. \end{aligned} \tag{3.14}$$

Second, consider a similar equation for the electrical part of the diagram where the sum of the applied voltages are equated to the voltage drop across the capacitor as

shown in (3.15).

$$\begin{aligned} V_{DC} + V_{ac} &= \frac{Q}{C} \\ &= \frac{Q\left(d_0 - u\right)}{\epsilon A} \end{aligned} \tag{3.15}$$

Since the goal of this exercise is to investigate the fundamental frequency response of the CMUT, the one can assume that the variables in (3.14) and (3.14) consist of static and first order terms:

$$\begin{aligned} u &= u_0 + \frac{1}{2}u_1 e^{\jmath\omega t} + \frac{1}{2}u_1^* e^{-\jmath\omega t} \\ Q &= Q_0 + \frac{1}{2}Q_1 e^{\jmath\omega t} + \frac{1}{2}Q_1^* e^{-\jmath\omega t} \\ F_A &= \frac{1}{2}F_1 e^{\jmath\omega t} + \frac{1}{2}F_1^* e^{-\jmath\omega t} \\ V_{ac} &= \frac{1}{2}V_{ac_1} e^{\jmath\omega t} + \frac{1}{2}V_{ac_1}^* e^{-\jmath\omega t} \ . \end{aligned} \tag{3.16}$$

These equations can also be used to calculate expressions for the nonlinear terms Q^2 and uQ which must be computed before they can be plugged into (3.14)and (3.15). Since only the fundamental frequency terms are of interest, the higher order terms will be left out to give

$$\begin{aligned} Q^2 &= Q_0^2 + Q_0 Q_1 e^{\jmath\omega t} + Q_0 Q_1^* e^{-\jmath\omega t} \\ uQ &= u_0 Q_0 + \frac{1}{2}\left(u_0 Q_1 + u_1 Q_0\right) e^{\jmath\omega t} + \frac{1}{2}\left(u_0 Q_1^* + u_1^* Q_0\right) e^{-\jmath\omega t} \ . \end{aligned} \tag{3.17}$$

Substituting (3.16) - (3.17) into (3.14) - (3.15) yields the following pair of equations:

$$\begin{aligned} V_{DC} + \frac{1}{2}V_{ac_1} e^{\jmath\omega t} + \frac{1}{2}V_{ac_1}^* e^{-\jmath\omega t} &= \frac{Q_0\left(d_0 - u_0\right)}{\epsilon A} + \frac{1}{2}e^{\jmath\omega t}\left[\overbrace{\left(\frac{1}{\jmath\omega C}\right)}^{Z_E}\underbrace{\jmath\omega Q_1}_{I_1} - \frac{Q_0}{\jmath\omega\epsilon A}\underbrace{\jmath\omega u_1}_{v_1}\right] \\ &+ \frac{1}{2}e^{-\jmath\omega t}\left[\left(\frac{1}{\jmath\omega C}\right)\jmath\omega Q_1^* - \frac{Q_0}{\jmath\omega\epsilon A}\jmath\omega u_1^*\right] \end{aligned} \tag{3.18}$$

and

$$\begin{aligned}\frac{1}{2}F_1 e^{\jmath\omega t} + \frac{1}{2}F_1^* e^{-\jmath\omega t} &= u_0 k + \frac{Q_0^2}{2\epsilon A} + \frac{1}{2}e^{\jmath\omega t}\left[\overbrace{-\left(\jmath\omega m + \frac{k}{\jmath\omega}\right)}^{z_m}\underbrace{\jmath\omega u_1}_{v_1} + \frac{Q_0}{\jmath\omega\epsilon A}\underbrace{\jmath\omega Q_1}_{I_1}\right] \\ &+ \frac{1}{2}e^{-\jmath\omega t}\left[-\left(\jmath\omega m + \frac{k}{\jmath\omega}\right)\jmath\omega u_1^* + \frac{Q_0}{\jmath\omega\epsilon A}\jmath\omega Q_1\right] . \qquad (3.19)\end{aligned}$$

By equating the coefficients of the $e^{\jmath\omega t}$ terms in the two equations above and using the new variable names as marked, the two electromechanical equations can be written as

$$\begin{aligned}V_{ac} &= Z_E I_1 - \frac{Q_0}{\jmath\omega\epsilon S}v_1 \\ F_1 &= -\frac{Q_0}{\jmath\omega\epsilon S}I_1 + z_m v_1 . \qquad (3.20)\end{aligned}$$

According to [38], these two equations are in the same format as those that describe an equivalent circuit where an electrical mesh couples to a mechanical one by a symmetric transduction coefficient. The representative circuit is shown in Figure 3.7 and its accompanying canoncial equations are

$$\begin{aligned}E &= Z_E I - Tv \\ F &= TI - z_m v . \qquad (3.21)\end{aligned}$$

A comparison between (3.20) and (3.21) shows that

$$\begin{aligned}T &= \frac{Q_0}{\jmath\omega\epsilon S} \\ &= \frac{1}{\jmath\omega\frac{\epsilon S}{Q_0}} \qquad (3.22) \\ &= \frac{1}{\jmath\omega C_T} \qquad (3.23)\end{aligned}$$

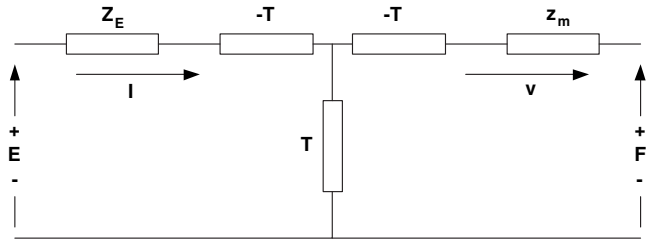

Figure 3.7: Canonical form of the equivalent circuit symbolizing the coupling of an electrical mesh to a mechanical one by a symmetric transduction coefficient.

where (E_0 represents the electric field in the capacitor)

$$C_T = \frac{\epsilon S}{Q_0} = \frac{d_0 - u}{V_{DC}} \ . \tag{3.24}$$

Furthermore, by filling in the full expressions for the variables Z_E and z_m, the equivalent circuit in Figure 3.7 can be redrawn as shown in Figure 3.8a or, equivalently, as Figure 3.8b[2].

The final step of the derivation of the schematic in Figure 3.5 is to build on the skeleton of Figure 3.8b. First, it should be noted that the capacitor labelled $\frac{1}{k}$ and the inductor make up the membrane impedance and can therefore be replaced with a block marked Z_{mem}. Second, the open circuit on the mechanical side of Figure 3.8b should be replaced with the mechanical load presented to the circuit. In air, the effects of the radiation of energy from the membrane to the environment can be represented by the complex impedance Z_{rad}. Further changes to the schematic include the addition of a parasitic capacitance in shunt with the device capacitor C_0 and series and shunt resistances R_{series} and R_{shunt}. Finally, the transformer ratio is defined through the conversion process as the quotient of the transduction coefficient divided by the impedance moved into the shunt position. Mathematically,

$$n \ = \ \frac{T}{Z_{C_0}}$$

[2]On page 108 of his text [38], Professor Hunt shows that the two networks are equivalent because "application of conventional electric-network analysis to [the two circuits] produces the same set of [equations] that are obtained by solving the differential equations for the original system."

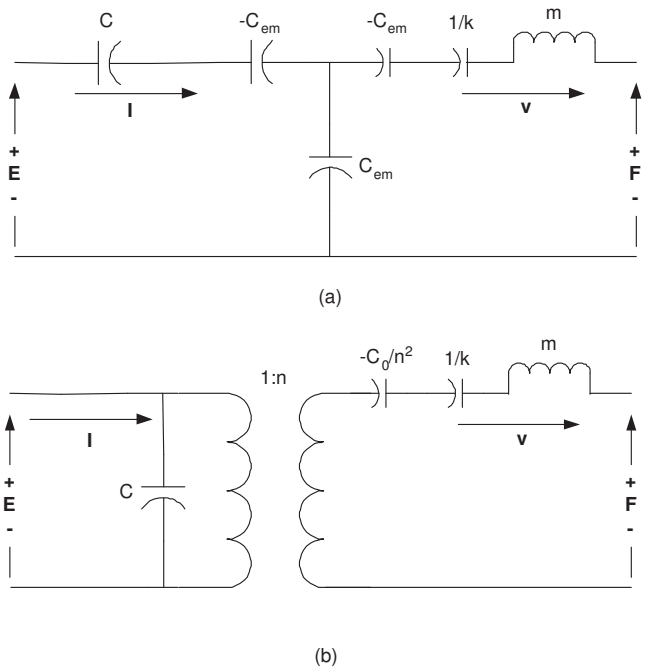

Figure 3.8: Equivalent forms of the equivalent circuit that describes the generic electromechanical transducer shown in Figure 3.6.

$$\begin{aligned} n &= \frac{C_0}{C_T} \\ n &= \frac{C_0 V_{DC}}{d_0 - u} \, . \end{aligned} \tag{3.25}$$

This is equivalent to stating that the turns ratio is equal to the product of the device capacitance and the electric field in the device. With these modifications and changes, the circuit of Figure 3.8b is identical to the one presented at the beginning of the section in Figure 3.5 and shown again below for convenience. Once again, specific details regarding the various elements that make up the model will be discussed in Chapter 4.

3.1.3 Manufacturing Process

The capacitive micromachined ultrasonic transducers described in this dissertation have been built using two different manufacturing processes. They are both described

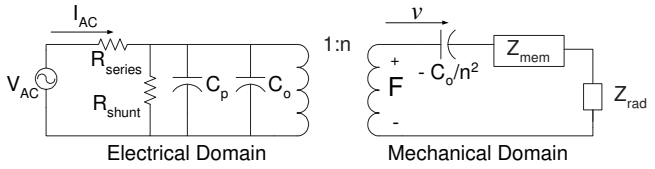

Figure 3.9: Equivalent circuit model of a transmitting CMUT.

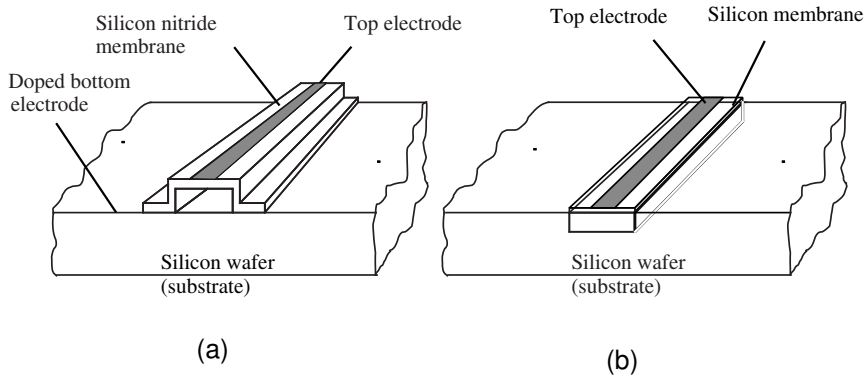

Figure 3.10: (a) Geometry of a CMUT built using the sacrificial-layer process; (b) Geometry of a CMUT built using the wafer-bonding method.

in detail in Chapter 5 where their merits and shortcomings are also discussed. The first, coined the *sacrificial layer method* [42], involves the deposition of LPCVD silicon nitride on top of a sacrificial layer of polysicilicon. After holes are drilled in the silicon nitride to expose the underlying polysilicon, the wafer is exposed to KOH in order to facilitate the membrane release. Figure 3.10a shows the geometry of a structure built using the sacrificial layer method.

The second process used to build the CMUT is the *wafer-bonding method* [36]. This technique gets its name from the fact that the actuating membrane is formed from the device layer of an SOI wafer that is bonded to a carrier wafer. The resulting geometry is shown in Figure 3.10b.

3.2 Lamb Waves

Lamb waves are one of the four types of elastic waves that can propagate in solids. They are defined as the waves that propagate along a thin plate (much smaller than the acoustic wavelength) with free boundaries. As will be shown mathematically in the following section (and touched on during the discussion in the previous chapter of the work of D.C. Worlton), the particle motion of the atoms in the plate are both normal to and along the plane of the substrate. This is in contrast to other waves (e.g., Love waves) that do not have particle motion in the normal direction. Figure 3.11 shows a description of these waves and includes an illustration of the two types of Lamb wave modes that can exist (symmetric[3] and anti-symmetric[4]).

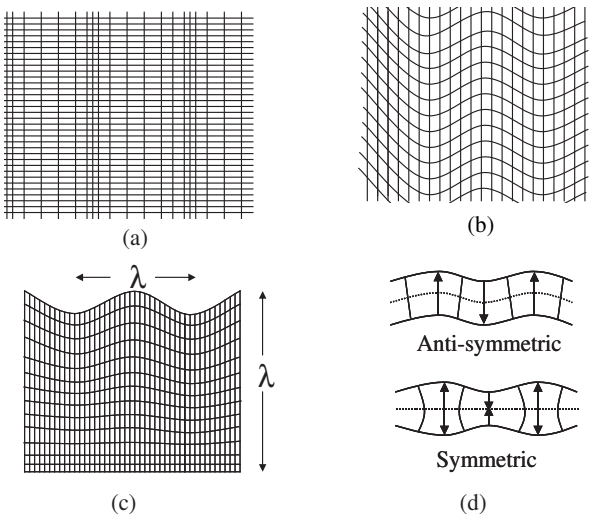

Figure 3.11: Pictoral representations of the cross-section of elastic waves propagating to the right. Both vertical and horizontal displacements are exaggerated for clarity. (a) Bulk longitudinal (compressional) wave in an unbounded solid; (b) Bulk transverse (shear) wave in an unbounded solid; (c) Surface acoustic wave (SAW) in a semi-infinite solid; (d) Flexural plate waves (Lamb waves) in thin solid plates.

[3]Since in the symmetric modes the boundaries of the plate periodically dilate and contract, they are often called *dilatational* or *longitudinal* modes

[4]Due to the periodic flexing motion of the plate boundaries these modes are also called *flexural* modes.

Variable	Description
τ	Stress Tensor
ε	Strain Tensor
ρ	Material Density
u	Particle Displacement
f	Applied Body Force Per Unit Mass
δ	Kronecker Delta
λ,μ	Lamé Costants

Table 3.1: Variables used in (3.26) - (3.28)

3.2.1 Derivation of the Period Equation

The velocity at which Lamb waves travel is determined by the frequency of the wave, the material in which the wave is travelling, and the thickness of the plate. The discussion in Chapter 2 presented the period-equation (2.1), the properties of which Lamb helped to explain in his 1889 paper. This equation is derived using the linear equations of elastodynamics and the boundary conditions of zero traction at the plate surface. The formulation [1] begins with a system of equations that govern the motion of a homogeneous, isotropic, linearly elastic body,

$$\tau_{ij,j} + \rho f_i = \rho \ddot{u}_i \tag{3.26}$$

$$\tau_{ij} = \lambda \varepsilon_{kk} \delta_{ij} + 2\mu \varepsilon_{ij} \tag{3.27}$$

$$\varepsilon_{ij} = \frac{1}{2}\left(u_{i,j} + u_{j,i}\right) \tag{3.28}$$

where these equations employ tensor notation, meaning the summation convention is assumed and that the comma represents differentiation. These formulas represent the stress equation of motion (also known as Cauchy's first law of motion), Hooke's law, and the strain-displacement relation, respectively. Table 3.1 described the variables that are used. When (3.28) is substituted into (3.27) and the resulting expression is plugged into Cauchy's first law of motion in the absence of body forces, the following

displacement equation of motion is obtained (summation convention is assumed):

$$\mu u_{i,jj} + (\lambda + \mu)\, u_{j,ji} = \rho \ddot{u}_i. \tag{3.29}$$

This system of equations is complicated in that it couples the three displacement components. Furthermore, efforts to uncouple them by eliminating two of the three displacement components through two of the three equations results in fourth order partial differential equations. An alternative method to handle the displacement equations of motion is to express the components of the displacement vector in terms of derivatives of potentials that satisfy uncoupled wave equations. In this effort, the equation of motion in (3.29) can be re-written in vector notation as

$$\mu \nabla^{\mathbf{2}} \mathbf{u} + (\lambda + \mu)\, \nabla \nabla \cdot \mathbf{u} = \rho \ddot{\mathbf{u}}. \tag{3.30}$$

For the terms in (3.30) and the equations that follow, light-faced letters stand for scalars, Roman letters in boldface represent vectors, and lower case Greek letters in boldface denote second-order tensors.

The next step in this process is to decompose the displacement vector in the form

$$\mathbf{u} = \nabla \varphi + \nabla \times \boldsymbol{\psi}. \tag{3.31}$$

Substituting (3.31) into (3.30) and using the identities $\nabla \cdot \nabla \varphi = \nabla^2 \varphi$ and $\nabla \cdot \nabla \times \boldsymbol{\psi} = 0$, the rearrangement of terms results in

$$\nabla \left[(\lambda + 2\mu)\, \nabla^2 \varphi - \rho \ddot{\varphi} \right] + \nabla \times \left[\mu \nabla^2 \boldsymbol{\psi} - \rho \ddot{\boldsymbol{\psi}} \right] = 0. \tag{3.32}$$

This equation is satisfied when the two bracketed terms equal zero. This occurs when φ and $\boldsymbol{\psi}$ satisfy the following[5]:

$$\nabla^2 \varphi \;=\; \frac{1}{c_L^2} \ddot{\varphi} \tag{3.33}$$

[5]It should be noted that (3.35) and (3.36) represent the longitudinal and shear wave velocities in the transducer, respectively.

$$\nabla^2 \boldsymbol{\psi} = \frac{1}{c_T^2} \ddot{\boldsymbol{\psi}} \tag{3.34}$$

$$c_L^2 = \frac{\lambda + 2\mu}{\rho} \tag{3.35}$$

$$c_T^2 = \frac{\mu}{\rho} \tag{3.36}$$

When (3.33) and (3.34) are used with (3.31), they result in uncoupled wave equations. The derivation of the period-equation continues by setting expressions for the field variables in such a way as to represent a standing wave in the x_2-direction and a propagating wave in the x_1-direction. For motion in plane strain (strain normal to the $x_1 - x_2$ plane and the shear strains $\gamma_{x_1 x_3}$ and $\gamma_{x_2 x_3}$ are equal to zero)[6] in the $x_1 - x_2$ plane,

$$u_3 \equiv 0 \tag{3.37}$$

$$\frac{\partial}{\partial x_3}(\ ) \equiv 0. \tag{3.38}$$

The system of equations represented by (3.31) then simplifies to

$$u_1 = \frac{\partial \varphi}{\partial x_1} + \frac{\partial \psi_3}{\partial x_2} - \cancelto{0}{\frac{\partial \psi_2}{\partial x_3}} \tag{3.39}$$

$$u_2 = \frac{\partial \varphi}{\partial x_2} - \frac{\partial \psi_3}{\partial x_1} + \cancelto{0}{\frac{\partial \psi_1}{\partial x_3}}. \tag{3.40}$$

The expressions for φ and $\boldsymbol{\psi}$ are found by expanding (3.33) and (3.34) as

$$\frac{\partial^2 \varphi}{\partial x_1^2} + \frac{\partial^2 \varphi}{\partial x_2^2} + \cancelto{0}{\frac{\partial^2 \varphi}{\partial x_3^2}} = \frac{1}{c_L^2} \frac{\partial^2 \varphi}{\partial t^2} \tag{3.41}$$

$$\frac{\partial^2 \psi_3}{\partial x_1^2} + \frac{\partial^2 \psi_3}{\partial x_2^2} + \cancelto{0}{\frac{\partial^2 \psi_3}{\partial x_3^2}} = \frac{1}{c_T^2} \frac{\partial^2 \psi_3}{\partial t^2} \tag{3.42}$$

[6] Alternately, surface traction forces $T \cdot x_2$ are equal to zero

and considering their solutions to be in the form

$$\varphi = \Phi(x_2)\exp\left[\jmath(kx_1 - \omega t)\right] \tag{3.43}$$

$$\psi_3 = \Psi(x_2)\exp\left[\jmath(kx_1 - \omega t)\right]. \tag{3.44}$$

Substituting (3.43) and (3.44) into (3.41) and (3.42), respectively, yields the following solutions in terms of constants A_1, A_2, B_1, and B_2:

$$\Phi(x_2) = A_1\sin(px_2) + A_2\cos(px_2) \tag{3.45}$$

$$\Psi(x_2) = B_1\sin(qx_2) + B_2\cos(qx_2) \tag{3.46}$$

$$p^2 = \frac{\omega^2}{c_L^2} - k^2 \tag{3.47}$$

$$q^2 = \frac{\omega^2}{c_T^2} - k^2 \tag{3.48}$$

Plugging (3.43) and (3.44) into (3.39) and (3.40) gives the following expressions for the particle displacements:

$$u_1 = \jmath k\Phi + \frac{d\Psi}{dx_2} \tag{3.49}$$

$$u_2 = \frac{d\Phi}{dx_2} - \jmath k\Psi \tag{3.50}$$

An analysis of these last two equations shows the symmetric and antisymmetric nature of Lamb waves. Note that u_1, or the displacement in the x_1 direction, is symmetric with respect to $x_2 = 0$ if it consists of cosine functions. Likewise, u_2 is symmetric with respect to $x_1 = 0$ if it consists of sine functions. This behaviour is illustrated in Figure 3.12. For antisymmetric waves u_1 contains cosine functions and u_2 consists of sine functions. Table 3.2 lists the function form of u_1, u_2, Φ, and Ψ for both categories of Lamb waves. The constants A_1, A_2, B_1, and B_2 can be obtained from the boundary conditions. For the situation described here, the boundaries are free and therefore τ_{21} and τ_{22} equal zero. Expressions for these stress tensors, derived

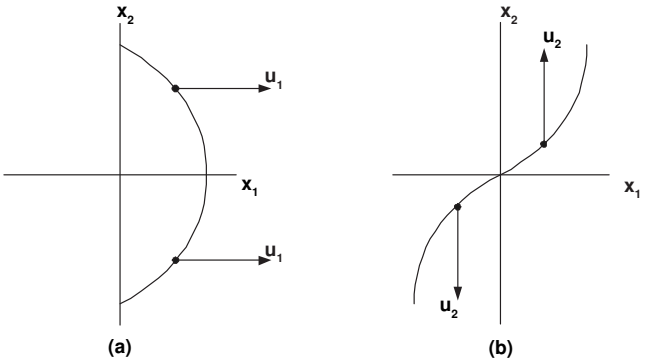

Figure 3.12: Illustrating the particle motion of a symmetric Lamb wave. (a) In the x_1 direction the particles follow a cosine behaviour as a function of x_2. Those above and below the center line $x_2 = 0$ move in the same direction. (b) In the x_2 direction the particles follow a sinusoidal behaviour as a function of x_2. Those that fall in the region $x_2 > 0$ move in the positive direction and those that are in the region $x_2 < 0$ move in the negative direction.

from (3.27) and (3.28), are

$$\tau_{21} = \mu\left(\frac{\partial u_2}{\partial x_1} + \frac{\partial u1}{\partial x_2}\right) = \mu\left(2\frac{\partial^2\varphi}{\partial x_1 \partial x_2} - \frac{\partial^2\psi}{\partial x1^2} + \frac{\partial^2\psi}{\partial x_2^2}\right) \tag{3.51}$$

$$\begin{aligned}\tau_{22} &= \lambda\left(\frac{\partial u_1}{\partial x_1} + \frac{\partial u_2}{\partial x_2}\right) + 2\mu\frac{\partial u_2}{\partial x_2} \\ &= \lambda\left(\frac{\partial^2\varphi}{\partial x_1^2} + \frac{\partial^2\varphi}{\partial x_2^2}\right) + 2\mu\left(\frac{\partial^2\varphi}{\partial x_2^2} - \frac{\partial^2\psi}{\partial x_1 \partial x_2}\right)\end{aligned} \tag{3.52}$$

which, when coupled with (3.43) - (3.48) result in

$$\tau_{21} = \mu\left[-2\jmath pA_2\sin(px_2) + \left(k^2 - q^2\right)B_1\sin(qx_2)\right] \tag{3.53}$$

$$\tau_{22} = \lambda\left(k^2 + p^2\right)A_2\cos(px_2) - 2\mu\left[p^2A_2\cos(px_2) + \jmath kqB_1\cos(qx_2)\right] \tag{3.54}$$

for symmetric modes and

$$\tau_{21} = \mu\left[2\jmath kpA_1\cos(px_2) + \left(k^2 - a^2\right)B_2\cos(qx_2)\right] \tag{3.55}$$

$$\tau_{22} = -\lambda\left(k^2 + p^2\right)A_1\sin(px_2) - 2\mu\left[p^2A_1\sin(px_2) - \jmath kqB_2\sin(qx_2)\right]. \tag{3.56}$$

Symmetric Modes

$$\Phi = A_2 \cos(px_2)$$
$$\Psi = B_1 \sin(qx_2)$$
$$u_1 = \jmath k A_2 \cos(px_2) + qB_1 \cos(qx_2)$$
$$u_2 = -pA_2 \sin(px_2) - \jmath k B_1 \sin(qx_2)$$

Antisymmetric Modes

$$\Phi = A_1 \sin(px_2)$$
$$\Psi = B_2 \cos(qx_2)$$
$$u_1 = \jmath k A_1 \sin(px_2) - qB_2 \sin(qx_2)$$
$$u_2 = pA_1 \cos(px_2) - \jmath k B_2 \cos(qx_2)$$

Table 3.2: Solutions to equations describing particle displacement of a Lamb wave. For u_1 and u_2, $\exp[\jmath(kx_1 - \omega t)]$ behaviour is assumed.

for asymmetric modes. In the (3.53) - (3.56) $\exp[\jmath(kx_1 - \omega t)]$ dependence is assumed.

Since the boundary conditions state that τ_{21} and τ_{22} equal zero at $x = \pm b$ where b is equal to the place thickness, (3.53) - (3.56) turn into a system of homogenous equations for which the determinant of their coefficients must equal zero. Doing this and combining terms yields the period equations for symmetric and antisymmetric Lamb wave modes as shown in (3.57) and (3.58), respectively.

$$\frac{\tan(qb)}{\tan(pb)} = -\frac{4k^2pq}{(q^2-k^2)^2} \tag{3.57}$$

$$\frac{\tan(qb)}{\tan(pb)} = -\frac{(q^2-k^2)^2}{4k^2pq} \tag{3.58}$$

The equations above list the period-equation in terms of the Lamé constants λ and μ. They can also be written in terms of the longitudinal (V_L) and shear (V_S) velocities of material in which the Lamb wave is propagating and the wave number β [5]:

$$\frac{\tan k_{ts}b/2}{\tan k_{tl}b/2} = -\frac{4\beta^2 k_{tl}k_{ts}}{(k_{ts}^2-\beta^2)^2} \quad (Symmetric) \tag{3.59}$$

$$\frac{\tan k_{ts}b/2}{\tan k_{tl}b/2} = -\frac{(k_{ts}^2-\beta^2)^2}{4\beta^2 k_{tl}k_{ts}} \quad (Antisymmetric) \tag{3.60}$$

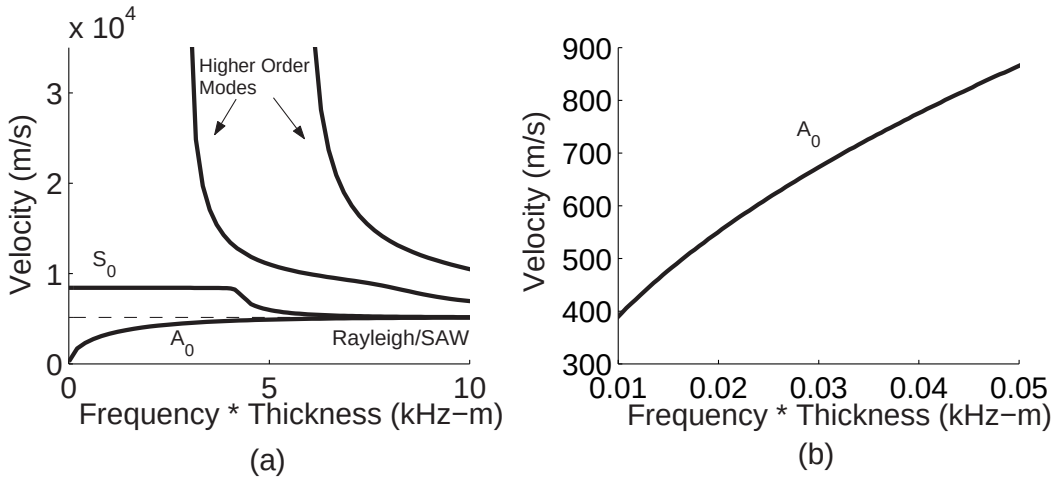

Figure 3.13: (a) Select Lamb and Rayleigh velocities on silicon. (b) An expansion of the A_0 curve for frequency-thickness values near .038 kHz-m, the operating point near the devices discussed in this paper. The calculations used to create both plots treat silicon as an isotropic material. The constants are taken from [4]: $V_s = 5840.9$ m/s, $V_l = 8429.4$ m/s.

$$k_{tl}^2 = \left(\frac{\omega}{V_l}\right)^2 - \beta^2 \tag{3.61}$$

$$k_{ts}^2 = \left(\frac{\omega}{V_s}\right)^2 - \beta^2 \,. \tag{3.62}$$

3.2.2 Analysis of the Period Equation

Every root in the period equation defines the phase velocity of a corresponding mode. When p and q are substituted into (3.57) and (3.58) (or k_{ts} and k_{tl} are substituted into (3.59) and (3.60)), the variables ω and b always appear together as a product. This is why people often refer to frequency-thickness products when discussing Lamb waves. Note that as the frequency-thickness product approaches zero both equations have only one root. These roots correspond to the zeroth order symmetrical (S_0) and anti-symmetrical modes (A_0). As ωb increases new roots appear that correspond to higher order symmetrical (S_1, S_2, S_3, etc.) and anti-symmetrical (A_1, A_2, A_3, etc.)

modes. A graph of the phase velocity of select modes is shown in Figure 3.13. The total number of symmetrical (N_S) and anti-symmetrical (N_A) modes that are possible in a plate of given thickness b at a frequency ω is [96]:

$$N_S = 1 + \left[\frac{b}{\lambda_t}\right] + \left[\frac{b}{\lambda_l} + \frac{1}{2}\right] \tag{3.63}$$

$$N_A = 1 + \left[\frac{b}{\lambda_l}\right] + \left[\frac{b}{\lambda_t} + \frac{1}{2}\right] \tag{3.64}$$

The brackets are used here to indicate a rounding to the nearest integer.

3.2.3 Lamb Wave Properties

As described in Chapter 2, Lamb waves can be excited using a number of different methods. One of the most popular is the wedge method where a Lamb wave is excited by a wave generated from an ultrasonic beam that intersects the plate's surface. The angle at which the beam hits is important in that a Lamb wave will only propagate if the horizontal component of the incident beam's spatial frequency vector (k) is equal to that of the Lamb wave [102]. Using the illustration in the upper part of Figure 2.1 for the orientation of θ, assigning the constant V for velocity and the subscripts $Lamb$ and Med to represent the Lamb wave and surrounding medium, respectively, the following expressions can be derived:

$$\sin\theta = \frac{k_{Lamb}}{k_{Med}} \tag{3.65}$$

$$k_n = \frac{2\pi f}{V_n} \tag{3.66}$$

$$\sin\theta = \frac{V_{Med}}{V_{Lamb}} \tag{3.67}$$

This derivation is in effect an application of Snell's Law [45] where θ_1 is the incident angle of the wave in the medium and θ_2 is equal to 90° and represents the transmission angle of the Lamb wave:

$$k_1 \sin\theta_1 = k_2 \sin\theta_2 \tag{3.68}$$

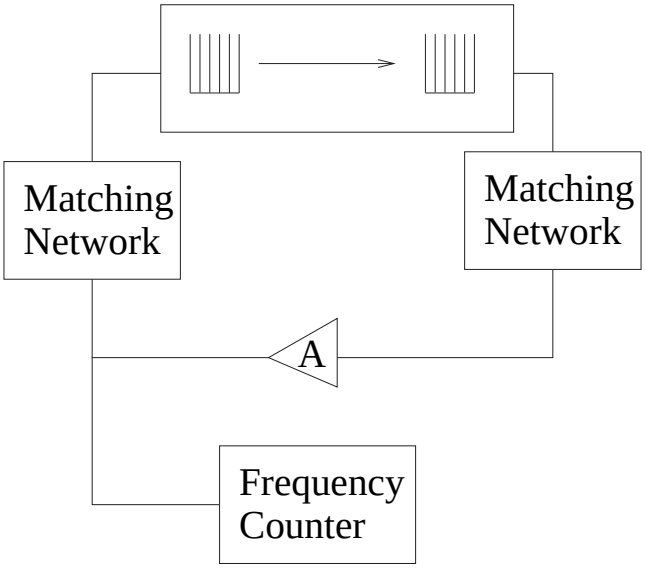

Figure 3.14: Experimental setup of the delay-line oscillator.

$$\frac{\sin\theta_1}{V_1} = \frac{\sin\theta_2}{V_2} \tag{3.69}$$

Equations 3.67 and 3.69 mathematically describe one other interesting property of Lamb waves. The previous chapter's description of the work of Stuart Wenzel described his reliance on the minimal leakage of acoustic energy from the plate to the surrounding medium. This phenomenon occurs when the velocity of sound in the plate is less than it is in the environment. If V_{Lamb} is less than V_{Med}, $\sin\theta$ will be greater than one which is not possible. The wave energy will therefore not escape from the plate into the environment.

One commonly used figure of merit for a Lamb wave device is its insertion loss. This parameter describes the power loss resulting from the insertion of a device in a transmission line. The minimum value that can be obtained for a Lamb wave device is 6 dB. This value assumes perfect electromechanical coupling both into and out of the A_0 mode of the Lamb Wave. The losses that do exist are the result of a splitting of the wave into two directions at both the transmitting and receiving membranes. This insertion loss can be measured from the S-parameters of the system or from the amplifier setting when the device is wired as a delay-line oscillator. The diagram in

Fig. 3.14 outlines the setup for the latter case; the amplifier is used to compensate for losses in the device and as such its gain is equal to the device insertion loss. The frequency of oscillation is determined by (3.70) which is derived from the condition that the total phase shift around the loop be an integral number of wavelengths [101]. In this equation,

$$f = \frac{v_p}{2\pi L}\left(2\pi N - \phi_E\right) \tag{3.70}$$

v_p is the phase velocity of the mode being observed, L is the acoustic path length (defined as the distance between the centers of the transmitting and receiving membranes), N is an integer greater than zero, and ϕ_E is the electronic phase shift through the amplifier. For a device in which the geometry and amplifier phase shift are fixed, the oscillation condition is determined by the value of N that corresponds to the frequency with the lowest insertion loss.

It is clear from (3.70) that the oscillation frequency is a function of the phase velocity of the Lamb wave in the channel. This relationship provides the basis for using such devices as sensors. When the velocity is influenced by any number of measurands (such as mass loading of the substrate or a change in its elastic stiffness) a shift in the operating frequency will result. By measuring the value of this shift, characteristics of the influencing factor can be determined.

3.3 Lamb Waves and CMUTs

The excitation of Lamb wave modes in CMUTs was first discovered during the characterization of 1-D CMUT arrays for medical imaging [43]. In the experiment a dip was noted in the radiation pattern of a single array element indicating a spurious radiating mode in the structure. The angle of this dip varied with frequency suggesting that energy was coupling into a wave mode with dispersive characteristics. Figure 3.15 shows the pattern at 3.5, 4, and 4.5 MHz. Further analysis concluded that this mode belonged to a Lamb wave. The presence of Lamb waves in devices built for the purpose of transmitting an acoustic signal into the surrounding medium (e.g., air, water, oil) has a deleterious effect on the system behavior [62, 73]. This is

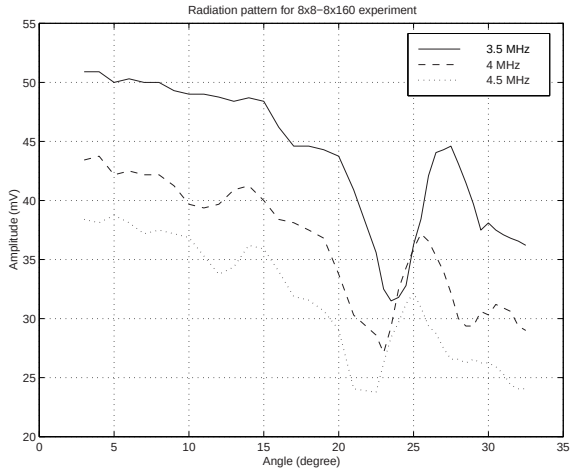

Figure 3.15: Radiation pattern of a CMUT for different operating frequencies. The substrate thickness is 500 μm. After [43].

because the wave that is excited presents an energy loss mechanism to the membrane and creates a cross-coupling of energy between otherwise independent cells. If this excitation of Lamb waves is instead exploited and optimized, however, the foundation for a new device is created. A proof of principle of this idea, along with a preliminary theoretical analysis of the concept, has been reported in [8, 105, 106]. Details on the second generation Lamb wave devices using CMUTs can be found in [7]; in this paper the foundation of the theory used to analyze the Lamb wave devices is discussed along with information on the manufacturing process and device performance. This dissertation covers all of the information in these papers in much more detail and adds to it with a presentation of the most recent work done in the field of capacitive micromachined ultrasonic Lamb wave transducers.

Chapter 4

Modeling

The theoretical models of the Lamb wave devices described in this dissertation use the skeleton of the CMUT equivalent circuit. This is appropriate since the CMUT is the transducer used to actuate the acoustic waves. The derivation of this circuit, based on that of a standard electromechanical transducer, was presented in Section 3.1.2. Since most devices fabricated using CMUT technology have membranes that closely approximate circles, theoretical models for devices with this membrane shape are relatively well developed [13, 54]. Furthermore, the equivalent circuits that result from these models have proven to match well with experimental results [16, 42]. The membranes in the devices described in this dissertation, however, are rectangular, and as a result a different set of equations is necessary to describe their behavior.

The first task of this chapter is therefore to derive and present the set of describing equations for rectangular membranes in order to create an equivalent circuit model of a Lamb wave device built using CMUT technology. In this effort two types of models are presented: piston and distributed. During the subsequent analysis, the limitation of these models with respect to the modeling of Lamb wave transduction is demonstrated. In order to accommodate this limitation, the structure is analyzed numerically using the finite element method. The legitimacy of this method is demonstrated by comparing the results of a limiting case to those obtained from the analytical model. The finite element model is then expanded and used to investigate aspects of device behavior, including the preferential coupling of power into the

A_0 mode, bounds on the device efficiency, and an analysis of the specific excitation mechanism through with Lamb waves are excited in the substrate.

4.1 Analytical Analysis: The Piston Model

As explained in Section 3.1.2, the equivalent circuit model (copied in Figure 4.1 for reference) is based on the standard equivalent circuit of a transmitting electromechanical transducer. The electrical side is on the left of the figure and consists of an input voltage V_{AC} and current I_{AC}. This is converted into a force F and corresponding velocity v by the transformer. Mathematically, it is through this transformer that the electromechanical transduction occurs. The force is measured in Newtons and is defined to be uniform over the surface of the membrane; the velocity is in units of $\left[\frac{m}{s}\right]$ and is defined as the average velocity over the width of the membrane. It is important to note that in this model the equations that describe the transformer assume that the movement of the membrane follows that of a piston. The sections that follow describe the various elements that make up the circuit. Note that all of the expressions below treat the case of a single rectangular membrane.

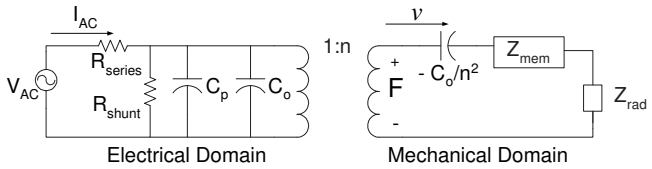

Figure 4.1: Equivalent circuit model of a transmitting CMUT derived in Section 3.1.2.

4.1.1 Membrane Impedance: $\mathbf{Z}_{mem}$

The membrane impedance is defined as the ratio of an applied uniform sinusoidal force on a membrane to the average velocity over the membrane of the resulting motion. Texts that derive the expression for a rectangular membrane generally do so for either a thin stretched membrane wherein the bending stiffness is negligible, or for thick geometries in which the tension is assumed to be insignificant. The membrane

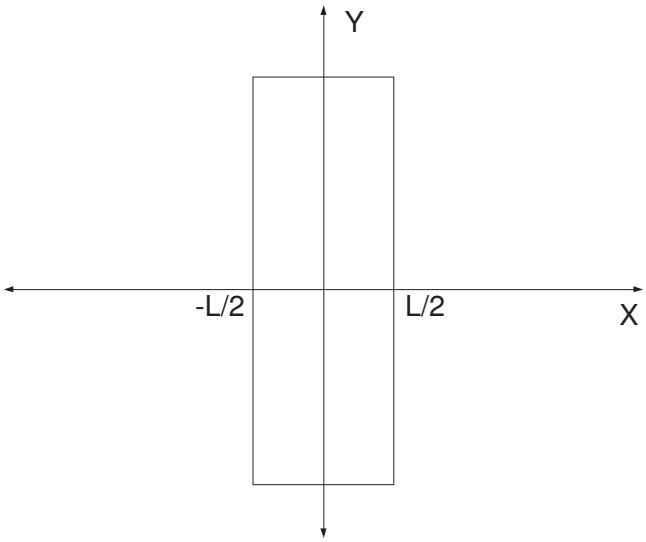

Figure 4.2: Orientation of the rectangular membrane used to solve (4.1).

thickness of the devices presented in this dissertation are between these two extremes. The derivation that follows thus takes the effects of both bending stiffness and tension into account.

Consider a stretched membrane with Young's Modulus Y_0, Poisson's Ratio σ, under a tensile stress T, with an applied uniform net pressure over the membrane surface of P, a density of ρ, and a thickness l_t. The differential equation governing the normal displacement $u_{AC}(x)$ of this membrane (derived from energy considerations) can be written as [54]:

$$\frac{(Y_0 + T)l_t^3}{12(1-\sigma^2)}\nabla^4 u_{AC} - Tl_t\nabla^2 u_{AC} - P + l_t\rho\frac{d^2u_{AC}}{dt^2} = 0 \tag{4.1}$$

Assuming that the aspect ratio of the membrane is large, and using the steady state condition, the membrane response and thus (4.1) can be reduced to a one dimensional problem in the x-direction. The clamped boundary condition (both the displacement and slope of the displacement of the membrane at the edges is zero) is used to solve this problem under the orientation shown in Figure 4.2. The resulting

solution for $u_{AC}(x)$, the displacement as a function of position, is:

$$u_{AC}(x) = 2c_{12}\cosh(k_1 x) + c_3\cos(k_3 x) - \frac{P}{\rho l_t \omega^2} \tag{4.2}$$

$$c_{12} = \frac{k_3 P \sin\frac{k_3 L}{2}}{l_t\rho\omega^2\left(2k_1\cos\frac{k_3 L}{2}\sinh\frac{k_1 L}{2} + 2k_3\sin\frac{k_3 L}{2}\cosh\frac{k_1 L}{2}\right)}$$

$$c_3 = \frac{\sinh\frac{k_1 L}{2} k_1 P}{l_t\rho\omega^2\left(k_1\cos\frac{k_3 L}{2}\sinh\frac{k_1 L}{2} + k_3\sin\frac{k_3 L}{2}\cosh\frac{k1 L}{2}\right)}$$

$$k_1 = \sqrt{\frac{d+\sqrt{d^2+4c\omega^2}}{2c}} \qquad k_3 = \sqrt{\frac{-d+\sqrt{d^2+4c\omega^2}}{2c}}$$

$$c = \frac{(Y_0+T)l_t^2}{12\rho(1-\sigma^2)} \qquad d = \frac{T}{\rho}$$

The next step in determining the membrane impedance is to find the average displacement over the short dimension of the membrane and to find its time harmonic derivative (the equivalent of multiplying by $j\omega$) to obtain the velocity v. Finally, using the initial assumption of a pressure P applied to the membrane, the impedance $Z_{mem} = \frac{P}{v}$ [mks-Rayls] can be written as

$$Z_{mem} = j\left(\frac{k_1 k_3 L l_t P\rho\omega}{k_1 k_3 LP - 2c_3 k_1 l_t\rho\omega^2\sin\frac{k_3 L}{2} - 4c_{12}k_3 l_t\rho\omega^2\sinh\frac{k_1 L}{2}}\right). \tag{4.3}$$

The constants k_1, k_3, c_{12}, and c_3 are defined in (4.2). Although it is not immediately obvious, (4.3) is independent of pressure as the P terms cancel out. They are left in the equations above in order to avoid redefining the previously listed constants. Note that the conventions set forth in Figure 4.1 use force and velocity relationships in the mechanical domain. As a result, the expression in (4.3) should be multiplied by the device area before it is applied to the equivalent circuit.

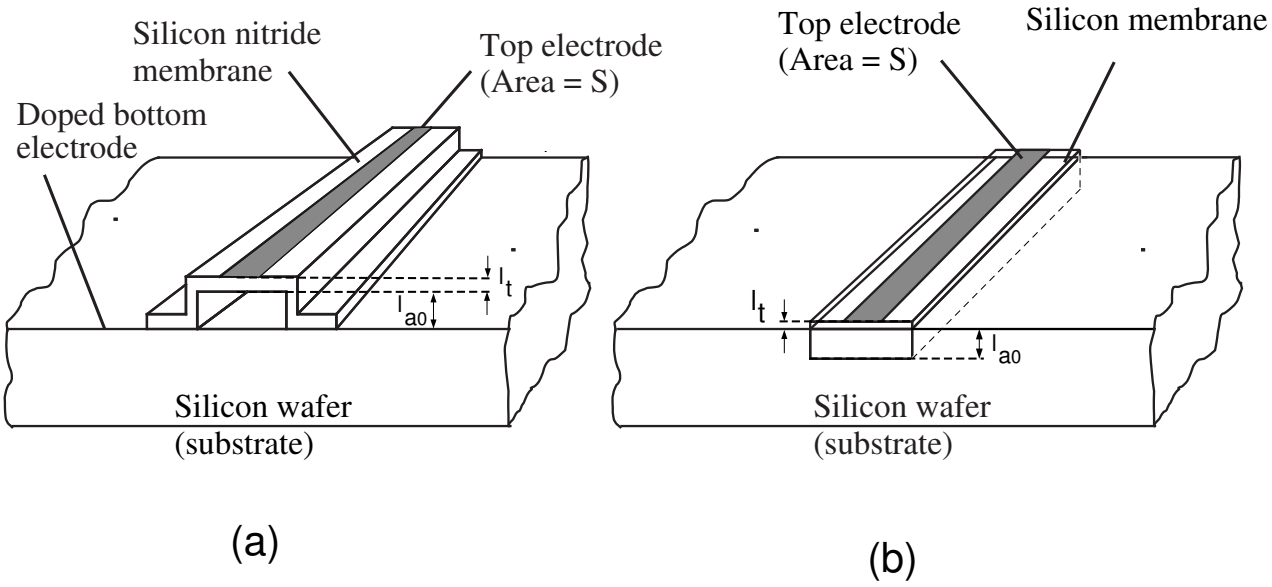

Figure 4.3: Diagram of a single CMUT membrane for the (a) sacrificial layer method and (b) wafer bonding method.

4.1.2 Device Capacitance: C_0

The element C_0 represents the static (DC) capacitance of the CMUT. As shown in Figure 4.3, a rectangular CMUT membrane consists of a metalized layer with an area S, a membrane of thickness l_t, and a vacuum gap of thickness $l_a(x)$. The latter term is actually a function of the lateral dimension, x, and thus can also be written as $(l_{a0} - u_{DC}(x))$ where l_{a0} is the thickness of the gap without any membrane deflection, and u_{DC} is a measure of the static deflection. Also present on the device but not shown in the figure is a thin insulation layer directly above the botton electrode of thickness l_i; in Figure 4.3a it is composed of silicon nitride while in Figure 4.3b it is made up of oxide. Neglecting fringing fields, the parallel plate capacitance of this structure is given by

$$C_0 = \frac{\epsilon_0 \epsilon_r S}{l_t + l_i + \epsilon_r (l_{a0} - u_{DC}(x))} \tag{4.4}$$

where ϵ_0 is the dielectric constant in air and ϵ_r is the relative permittivity constant of the insulating material.

An expression for $u_{DC}(x)$, the static deflection of the membrane due to an applied pressure, is thus necessary to accurately model the static device capacitance. While this can be done by taking the expression from (4.2) and finding its limit at very small frequencies, it is easier to find a qualitative expression by redoing the derivation starting with (4.1) and setting the frequency term to zero. After some mathematical steps similar to those used to derive the membrane impedance, the following expression for the membrane deflection is obtained:

$$\begin{aligned} u_{DC}(x) &= \frac{LP}{8d'k_3'}\left(k_3'L - 4\coth\frac{k_3'L}{2}\right) \\ &\quad + \frac{LP}{2d'k_3'}\frac{\cosh k_3'x}{\sinh\frac{k_3'L}{2}} - \frac{Px^2}{2d'} \\ k_3' = \sqrt{\frac{d'}{c'}} \quad c' &= \frac{(Y_0+T)l_t^3}{12(1-\sigma^2)} \quad d' = Tl_t \end{aligned} \tag{4.5}$$

4.1.3 Radiation Impedance: Z_{rad}

As a result of the motion of the rectangular membrane, the surrounding acoustic medium exerts a reaction force on it that is related to the velocity of the membrane through the radiation impedance. The derivation of this impedance treats the structure as a piston in a rigid infinite baffle and evaluates the expression as a function of the aspect ratio r of the piston where $r = \frac{a}{b} \geq 1$. Approximate expressions for the impedance reported in [83] are repeated here and used in the model of Figure 4.1. These expressions were obtained by relating the radiation impedance of a rectangular membrane to the Fourier transform of its impulse response.

$$Z_r(kb) = \rho c S_r[R_r(kb) + jX_r(kb)] \tag{4.6}$$

$$\begin{aligned} R_r(kb) \sim 1 &- \left(\frac{2}{\pi r(kb)^2}\right)\left(1 - \cos kb - \cos rkb + \cos\left([r^2+1]^{\frac{1}{2}}kb\right)\right) \\ &+ \left(\frac{2}{\pi}(kb)^3\right)^{\frac{1}{2}}\cos\left(kb + \frac{3\pi}{4}\right) + \left(\frac{2}{\pi}(rkb)^3\right)^{\frac{1}{2}}\cos\left(rkb + \frac{3\pi}{4}\right) \end{aligned}$$

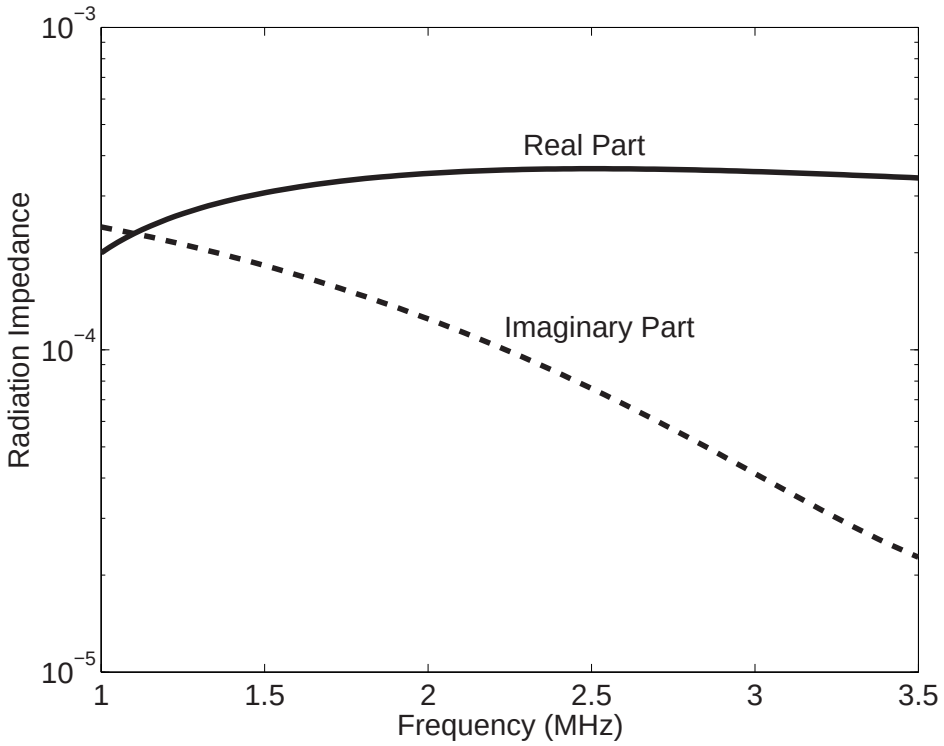

Figure 4.4: Real (solid) and imaginary (dashed) parts of the impedance presented by air to a membrane 1 cm long and 77 μm wide. Constants for air are taken from [45]: $\rho = 1.24$ kg/m^3, $v = 344$ m/s.

$$X_r(kb) \sim \left(\frac{2(1+r)}{r\pi kb}\right) - \left(\frac{2}{r\pi(kb)^2}\right)\left(\sin kb + \sin rkb - \sin kb\left(r^2+1\right)^{\frac{1}{2}}\right) - \left(\frac{2}{\pi}(kb)^3\right)^{\frac{1}{2}} \sin\left(kb + \frac{3\pi}{4}\right) - \left(\frac{2}{\pi}(rkb)^3\right)^{\frac{1}{2}} \sin\left(rkb + \frac{3\pi}{4}\right)$$

In (4.6), k is the wave number, S_r is the membrane surface area, and ρ and c are the density and speed of sound in the surrounding medium, respectively. The graph in Figure 4.4 applies this equation to a membrane 1 cm long and 77 μm wide.

4.1.4 Transformer Ratio: n

The transformer ratio n transforms the electrical quantities on the left side of the circuit to mechanical quantities on the right side. It is purely a mathematical construct but can be used analytically as a circuit element. Its origins are described by Hunt [38] where he analyzes the energy constraints of a physically realizable system and assumes that the membrane deflection is identical to that of a piston. Half metalization of the upper electrode is taken into account by this variable; Bozkurt [15] shows that this is the optimal metal coverage, for it maximizes the device bandwidth without significantly decreasing the membrane deflection. In the equation below V_{DC} represents the DC bias voltage on the transducer. It is equivalent to (3.25) but looks different due to substitution of the capacitance terms for the variable C_0.

$$n = \frac{V_{DC}\epsilon_0\epsilon_r^2 S}{(l_i + l_t + \epsilon_r l_a)^2} \tag{4.7}$$

4.1.5 Spring Softening Capacitance: $-C_0/n^2$

The negative capacitance present on the mechanical side of the circuit models the spring softening phenomenon described in Section 3.1.1. Since the physical phenomenon is built into the fundamental force equations used to derive the equivalent circuit model, it is appropriate that this term manifest itself in the final model. As expected, an increase in applied bias voltage decreases the value of the capacitance and therefore increases the absolute value of the element's impedance. Since the capacitor is in series with the membrane it acts to subtract from its capacitance, effectively decreasing the membrane spring constant.

$$C_{soft} = \frac{-C_0}{n^2} \tag{4.8}$$

4.1.6 Parasitic Impedances: C_p, R_{series}, and R_{shunt}

The parasitic capacitance C_p refers primarily to the effects of the traces on the Lamb wave device that lead from the bond pads to the membranes. In the devices described in this paper, C_p is typically 20% of the total CMUT capacitance. R_{series} and R_{shunt}

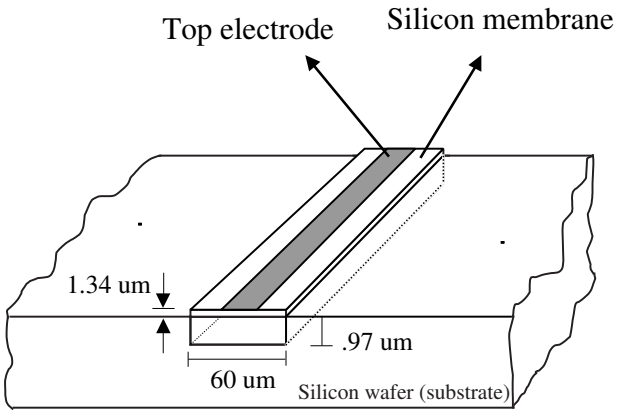

Figure 4.5: Geometry used in obtaining data presented in this chapter.

model lead resistances and membrane conductances in the transducer, respectively, that are typically insignificant in the model.

4.1.7 Using The Piston Model

This section presents the results obtained by applying the equations above to the schematic presented in Figure 4.1. It is assumed that the device is operating without parasitics in a vacuum and therefore the effects of R_{series}, R_{shunt}, C_p, and Z_{rad} can be ignored. The results presented are the membrane deflection, the membrane impedance and the device input impedance plotted using the appropriate equations in relation to the geometry shown in Figure 4.5. It is important to note that the schematic does not account for the presence of a substrate in the device geometry. A method for dealing with finite substrate values will be introduced later in this chapter.

A plot of the membrane deflection due to a pressure of one atmosphere, drawn using the expression in (4.5), is shown in Figure 4.6. Note that it is clear from the figure that the boundary conditions are satisfied in that both the first and second derivatives of the curve are zero at each end. Furthermore, as is intuitively expected, the membrane has its maximum displacement in the middle.

The membrane impedance, derived using the formula presented in (4.3), is shown

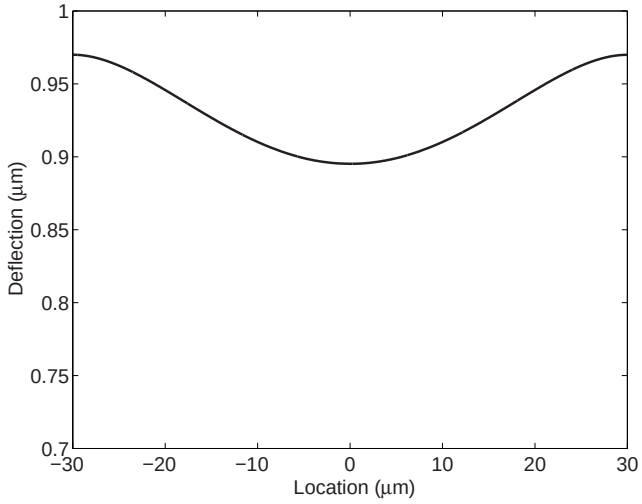

Figure 4.6: Static membrane deflection as a function of location for the structure shown in Figure 4.5. The ambient pressure on the membrane in this simulation is 1 atmosphere = 101.3 kPa. The constants used in this simulation are Y_0 = 1.67 x 10^{11} Pa, σ = .053, ρ = 2332 kg/m^3, and T = 100 MPa.

in Figure 4.7. Only the imaginary part is shown as the real part of the impedance is zero. Note that for the geometry in question, the resonant frequency is 3.25 MHz. Below this value the membrane is capacitive while above it is inductive. The dashed line in the graph reflects the impedance of a series inductor-capacitor circuit with values chosen to curve fit to the membrane impedance. They match very well both around and below the resonant frequency, confirming that a CMUT membrane can in fact be represented by an LC circuit as was suggested in Section 3.1.2.

Finally, the input impedance of the structure is shown in Figure 4.8. Again, only the imaginary part of the curve is shown as the real part is equal to zero due to the absence of lossy elements in the circuit. The shape of this curve can be intuitively understood by analyzing the transducer's equivalent circuit. At both low and high frequencies the shape of the curve is that of a capacitor. The value of this capacitor is equal to the device capacitance C_0 modified slightly (usually around 30%) by the reactance from the mechanical side. Away from these two extremes, however, the input impedance exhibits two resonances: a short circuit resonance at 2.99 MHz and an open circuit resonance at 3.25 MHz. The source of these two resonances

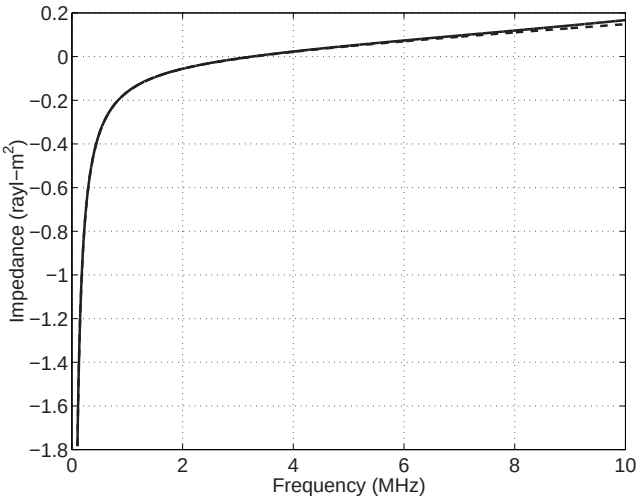

Figure 4.7: Membrane impedance for the structure shown in Figure 4.5. The solid line was obtained using the analytical equation in (4.3); the dashed line is a curve fit from a series LC circuit where L = 2.65 nH and C = 891.6 nF.

can be understood by analyzing the schematics shown in Figure 4.9. The upper schematic is a scaled down version of the electromechanical equivalent circuit where, in concordance with the assumptions presented at the beginning of this section, the parasitic elements and Z_{rad} have been left out. When the mechanical (right) side is converted to the electrical (left) side through the transformer, the bottom schematic is obtained. The short circuit resonance occurs when the impedance of the right branch of Figure 4.9b goes to zero, thus shorting out the input. This occurs slightly below the membrane resonant frequency due to the effect of $-C_0$ on Cn^2. The open circuit resonance occurs exactly at the membrane resonance; at this frequency the schematic in Figure 4.9b is reduced to two parallel capacitors of equal and opposite value which cancel each other out resulting in an open circuit. Note that the open circuit resonance at 3.25 MHz in Figure 4.8 is consistent with the membrane resonance of 3.25 MHz shown in Figure 4.7.

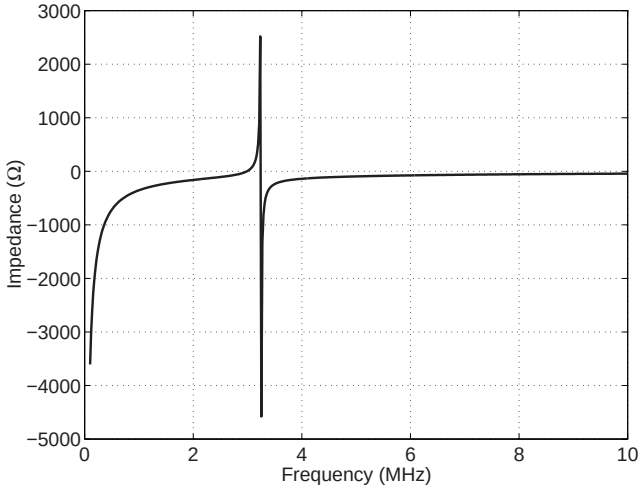

Figure 4.8: Input impedance for the structure shown in Figure 4.5.

4.2 Analytical Analysis: The Distributed Model

The foundation for the distributed model of the CMUT is based on work by Professor Harrie A.C. Tilmans, currently at the Katholieke Universiteit Leuven in Belgium [85]. He, in turn, based his work on that of Eugen J. Skudrzyk [82]. This model is different from the piston one in that the equation for the transduction coefficient in the describing equivalent circuit allows for the actual membrane shape. The goal of this section is to use Tilman's methods, and in some cases his equations, to modify selected expressions derived in the previous section. This is done primarily in the mechanical domain by performing modal analysis using the equation of motion for a membrane. Specifically, the terms in the equivalent circuit model that relate to the transduction coefficient, and are therefore affected, are the transformer turns ratio n and the spring softening capacitor -C_0/n^2.

4.2.1 Distributed Expressions for Spring Softening and the Transformer Turns Ratio

The equivalent circuit of a CMUT is shown in Figure 4.10. It is identical to the schematics derived above except for a change in nomenclature; the element variables

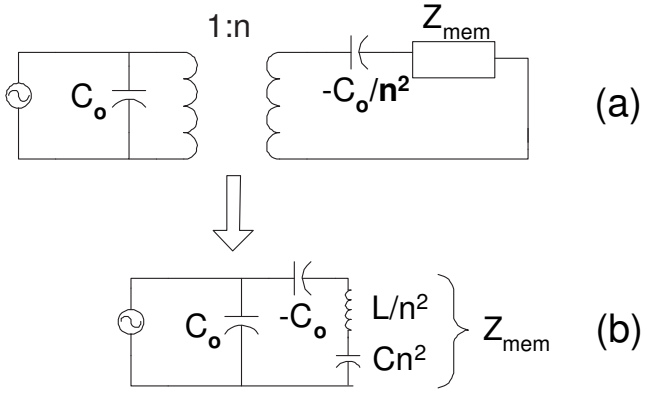

Figure 4.9: Schematics used in the discussion to explain open and short circuit resonance phenomena.

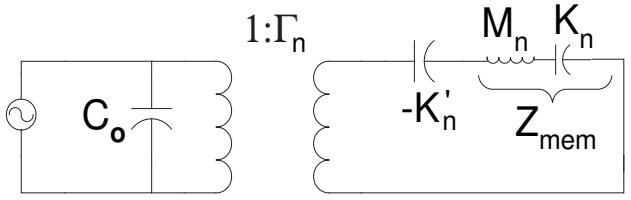

Figure 4.10: Equivalent circuit of a transmitting CMUT using the nomenclature of [85].

have been modified to match those used by Tilmans in [85]. This will help in differentiation between expressions relating to the piston and distributed models. The elements relevant to this discussion are the spring softening capacitor ($-K_n'$) and the transformer turns ratio Γ_n.

The linearized differential equation of motion that governs the transverse deflections $u_{AC}(x,t)$ of a prismatic beam (membrane) with rectangular cross-section can be written as shown in (4.9) where b is the plate thickness and h is its length. Note that the tension in the membrane is ignored in this formulation.

$$EI\frac{\partial^4 u_{AC}(x,t)}{\partial x^4} + \rho bh\frac{\partial^2 u_{AC}(x,t)}{\partial t^2} = 0 \tag{4.9}$$

According to [79, 85], modal analysis techniques show that the solution to (4.9) can be written as

$$u_{AC}(x,t) = \sum_{n=1}^{\infty} \phi(x)\,\xi(t) \tag{4.10}$$

where $\phi_n(x)$ are the normalized mode shapes and $\xi(t)$ are the generalized coordinates. A characteristic of normalized mode shapes relevant to this derivation is that they follow the relation

$$\frac{1}{L}\int_0^L \phi_n(x)\,\phi_m(x) = \delta_{mn} \tag{4.11}$$

Therefore, if the series expansion of (4.10) is introduced into the equation of motion, each term will be multiplied by a normal mode function $\phi_m(x)$. When the terms are integrated over the length of the beam, the following equation is obtained:

$$\rho bh\int_0^L \phi_n^2(x)\,dx\,\frac{\partial^2\xi(t)}{\partial t^2} + \int_0^L \phi_n(x)\,EI\frac{\partial^4\phi_n(x)}{\partial x^4}dx\,\xi(t) = 0 \tag{4.12}$$

or, equivalently,

$$M_n\ddot{\xi}(x) + K_n\xi(t) = 0 \tag{4.13}$$

where M_n is the generalized mass corresponding to mode n and K_n is the generalized stiffness ($\frac{1}{k}$) corresponding to mode n. Recall from the discussions associated with Figures 3.8 and 4.9 that the membranes can be modeled as the series combination of an inductor and a capacitor. The values of these elements relate directly to M_n and K_n, respectively. Evaluation of the integrals shows that $M_n = \rho bhL$ and $K_n = \omega_n^2 M_n$ where ω_n is the undamped natural frequency associate with mode n or, equivalently, the square root of the eigenvalue of the function ϕ_n.

Note that the equation of motion used thus far in the derivation does not take into account the presence of electrostatic forces. If the membrane impedance is to be correctly modeled, the effect of spring softening and therefore electrostatic forces must be included. The equation of motion can be modified by adding two terms into the equation. The first is on the left side of (4.9) to model the spring stiffness arising from electrostatic coupling. It is best thought of as a small signal force found by taking the derivative with respect to x of the force on the capacitor's electrodes under a static bias. The equation that describes this can be derived using (3.4) as a starting point

but with $u(x,t) \rightarrow u_{DC}(x)$; furthermore, the area term (S) is replaced with that of the width of the membrane (b) in order to be consistent with the equations in this section that deal with forces per unit length:

$$\frac{\partial F}{\partial u} = -\frac{b\epsilon V_{DC}^2}{\left(d_0 - u_{DC}(x)\right)^3} \tag{4.14}$$

The second term that modifies (4.9) represents the external applied electrostatic force and is added to the right side of the equation. This force can once again be found starting with (3.4) but this time the derivative is taken with respect to the applied voltage:

$$\begin{aligned} \frac{\partial F}{\partial V} &= \frac{\epsilon b V_{DC}}{\left(d_0 - u_{DC}(x)\right)^2} \\ F_{ac} &= \frac{\epsilon b V_{DC}}{\left(d_0 - u_{DC}(x)\right)^2} V_{ac}(t) \end{aligned} \tag{4.15}$$

With these changes, the equation of motion in the presence of an electrostatic field becomes

$$EI\frac{\partial^4 u_{AC}(x,t)}{\partial x^4} - \frac{b\epsilon V_{DC}^2}{\left(d_0 - u_{DC}(x)\right)^3} + \rho bh\frac{\partial^2 u_{AC}(x,t)}{\partial t^2} = \frac{\epsilon b V_{DC}}{\left(d_0 - u_{DC}(x)\right)^2} V_{AC}(t) \tag{4.16}$$

According to Tilmans the mode shapes continue to display the orthogonality property in the presence of electrostatic forces. Therefore, using a method similar to the one described above when solving (4.12), the equation is rewritten as:

$$M_n^* \ddot{\xi}_n(t) + K_N^* \xi_n(t) = \Gamma_n v(t) \tag{4.17}$$

where the asterisk denotes the presence of electrostatic forces.

Tilmans shows that when the equation above is solved, $M_n^* = M_n$ and that

$$K_n^* \approx K_n - K_n' \tag{4.18}$$

where

$$\begin{aligned} K_n' &= \int_0^L \frac{b\epsilon V_{DC}^2 \left[\phi_n^* (x)\right]^2}{\left(d + u_{DC}(x)\right)^3} dx \\ &\approx \frac{bL\epsilon V_{DC}^2}{d^3} \end{aligned} \tag{4.19}$$

The solution also introduces the electromechanical transduction factor, Γ_n:

$$\Gamma_n = \int_0^L \frac{b\epsilon V_{DC} \phi_n^* (x)}{\left(d + u_D C(x)\right)^2} dx \tag{4.20}$$

Under the assumption that the bias deflection is much smaller than the zero-voltage gap spacing ($u_{DC}(x) \ll d$), $\phi_n^*(x) \approx \phi_n(x)$. Note that the natural frequencies are affected by the presence of electromechanical coupling even though the mode shapes are not.

The expression for the eigenfunction, ϕ_n, included in equations (4.19) - (4.20) is obtained by taking a series of steps outlined in [79]:

1. Write the differential equation of motion for the structure.
2. Use the separation of variables method to obtain a new equation.
3. Turn this new equation into two separate ordinary differential equations.
4. Write the general solution to these equations.
5. Apply boundary equations to solve for the constants in the general solution.

Starting with (4.9) as the equation of motion and following the steps outlined above, the eigenfunctions of the structure in question (often referred to as a clamped-clamped beam) is [79]:

$$\phi_{nCC}(x) = \cos(k_n x) - \cosh(k_n x) + \frac{\cos(k_n L) - \cosh(k_n L)}{\sinh(k_n L) - \sin(k_n L)} \left(\sin(k_n x) - \sinh(k_n x)\right) \tag{4.21}$$

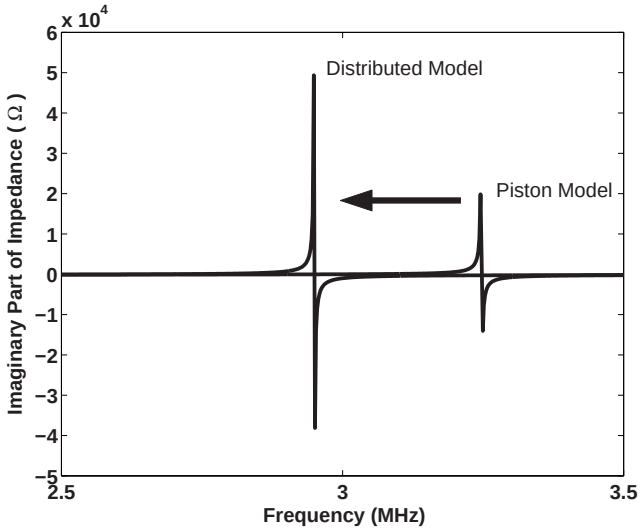

Figure 4.11: A comparison between the CMUT input impedance results obtained using the piston and distributed models. The curve representing the piston model is identical to the one shown in Figure 4.8.

4.2.2 Using The Distributed Model

The input impedance of a rectangular CMUT using the distributed model is shown in Figure 4.11. For comparison purposes, the input impedance obtained from the piston model is superimposed on the graph. Again, only the imaginary part is shown as the real part is equal to zero. In terms of the equivalent circuit model, the differences between the two graphs lie in the expressions for the circuit elements shown in Table 4.1. Note that in modeling the distributed nature of the transducer, both resonance frequencies have shifted to the left. It should be noted that while the magnitude of the impedances appears to have also increased, they are in fact infinite for both models. The finite values shown are the result of the sampling by MATLAB in the creation of the plots.

	Piston Model			Distributed Model	
Element	Variable	Equation	→	Variable	Equation
Spring Softening Capacitor	$\frac{-C_0}{n^2}$	(4.4) and (4.7)	→	K'_n	(4.19)
Transformer Turns Ratio	n	(4.7)	→	Γ	(4.20)

Table 4.1: Circuit element modifications between the piston and distributed models.

4.3 Equivalent Circuit Modeling of Lamb Wave Transduction

The piston and distributed models are both accurate and efficient in their efforts to describe the behavior of a CMUT. They are accurate in that they clearly show how device characteristics are affected by changes in the electrical and mechanical characteristics of the device; they are efficient in that said characteristics can be determined in a time span on the order of a few seconds when the appropriate equations are coded in a mathematical software package such as MATLAB. The two models in question do, however, have a significant shortcoming when it comes to the modeling of Lamb wave devices: they do not model the transfer of energy from the vibrating membrane to the substrate.

Recall from the discussion in Section 3.1.2 that the mechanical load presented to the device is placed in series with the membrane impedance on the secondary side of the transformer. In the subsequent discussion, that load was labeled Z_{rad} to represent the radiation impedance of the environment surrounding the transducer. For Lamb wave devices built using CMUTs, an additional construct is necessary to model the transfer of energy from the vibrating membrane into the substrate. This construct would ideally be modeled both by a transformer that would represent energy transfer from the membrane to the substrate, and a load on the secondary side representing the impedance presented to the acoustic wave. The approach described in this section analyzes said load after it is transformed to the primary and, as shown in the schematic of Figure 4.12, treats it like a resister labelled $R_{substrate}$. A resistor is chosen in this instance because the substrate effectively acts as a source of energy loss to the membrane. While it is not a resistor in the true sense of the word since its value

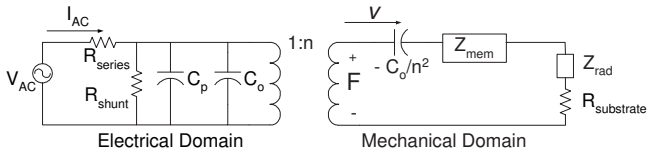

Figure 4.12: Equivalent circuit of a transmitting CMUT modified to include the coupling effect of energy into a Lamb wave in the substrate.

changes with frequency, this analysis is only concerned with the real part of its value. Note that while loss usually has a negative connotation, it is used in a positive sense in this case since a higher loss translates to an increase in energy in the Lamb wave. Significant coupling will result when this resistance is much greater than that of other dissipative elements in the circuit. Since the membrane impedance (Z_{mem}) is reactive, the impedance of air (Z_{rad}) is the only other element in this particular model that has a finite real part. The value of Z_{rad} cannot easily be changed as it is primarily a function of physical constants. Thus, the design goal is to maximize the resistance presented by the silicon substrate. It will later be shown that this goal is achieved by minimizing the thickness of the substrate upon which the device is built. As with Z_{rad}, the resistor is in series with the membrane impedance because an increase in the value of $R_{substrate}$ corresponds to a larger energy sink into the substrate.

A necessary condition for the elements in both the piston and distributed models is that they must be described by expressions with closed form solutions. These solutions are available for various acoustic loads but one does not yet exist for the load presented to a CMUT membrane by the substrate. As a result, while both models derived above can model a CMUT in its effort to transmit energy into air, neither can account for the energy that is coupled into the substrate. A third modeling method is therefore necessary in order to properly describe the transduction of Lamb waves using capacitive micromachined ultrasonic transducers: the finite element method.

4.4 The Finite Element Model

The finite element method (FEM) is used because a closed form solution is not available that could describe the energy transfer from a vibrating membrane into the substrate as modeled by the circuit element $R_{substrate}$ (see Figure 4.12), does not exist. This section describes the resulting finite element model built to aid in the effort to better understand Lamb wave devices fabricated using CMUT technology. It begins with some background on finite element analysis (FEA) and a discussion of how it is used in conjunction with the equivalent circuit model described earlier in this chapter. In this effort, a verification of the finite element model of a CMUT is presented. This is done by comparing the analytical and FEA results of a structure built to match the geometry and assumptions associate with the piston model of a CMUT. Finally, a complete finite element model is used to provide an in-depth understanding of the Lamb wave device including membrane behavior, the coupling mechanism, and the properties of the Lamb wave that is generated.

4.4.1 Introduction to Finite Element Analysis

Finite element analysis is a numerical technique that is traditionally used to solve problems in the fields of engineering and mathematical physics. These problems generally involve complicated geometries that cannot be described using ordinary or partial differential equations for which analytical solutions can be found. Rather, a system of simultaneous algebraic equations are written that yield values for the unknowns at different points in the continuum. There are two general approaches associated with FEA: the force method and the displacement method. The formulation of the latter is much simpler for most structural analysis problems and is the one used by ANSYS 5.7, the commercially available finite element package used in this dissertation [51].

In the displacement method of FEA, a structure is broken into small interconnected elements which consist of a series of nodes. Using known stress/strain properties for the material(s), a set of equations can be written to describe the behavior of each node in terms of every other node in the structure. The system of equations

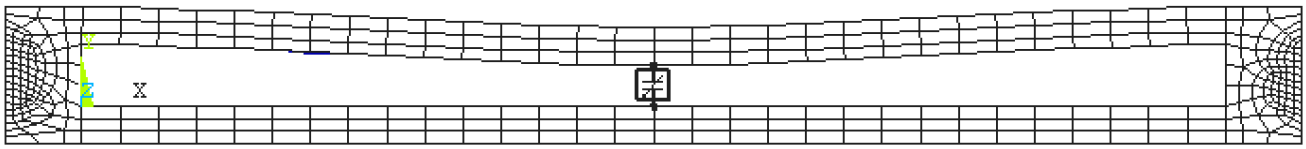

Figure 4.13: Element used in FEA model verification.

is best written in matrix notation and can be solved by a computer.

While this is a very powerful tool, it has one serious drawback: long computation times. While the simulations associated with the piston and lumped models can be run on a standard PC in a matter of seconds, the analyses associated with FEA can easily run for a few hours or days.

4.4.2 Model Verification: A Piston CMUT

Before using FEA to study capacitive micromachined ultrasonic Lamb wave devices, effort was put into verifying that the technique could appropriately model the structure and that the resulting data could be properly analyzed. This was done by building a CMUT (without a substrate) using ANSYS 5.7 that could be accurately modeled using the piston equivalent circuit model shown in Figure 3.5. As shown in Figure 4.13, the structure consists of a rectangular membrane broken into numerous elements. The cross-sectional geometry is identical to the one presented in Figure 4.5; the length in the finite element model is assumed to be one meter. The element type for the transducer material is Plane82 and the electromechanical element is Trans126. Although it is not apparent from the figure, the mechanical structure is held in place by a zero-displacement constraint along all of the device boundaries except for on top of the membrane. This is important as it prohibits energy transfer from the membrane to other parts of the structure. Furthermore, the width of the transducer element is equal to the width of the device, yet the element is mechanically coupled only to the center node of the device. It is this arrangement that causes the structure to acts as a piston transducer.

The input impedance of the transducer can be found in ANSYS by extracting the current drawn by the transducer element and determining its ratio to the known

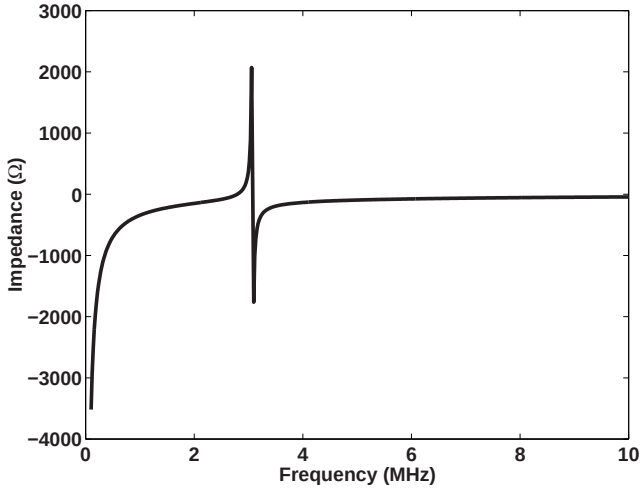

Figure 4.14: Input impedance obtained from ANSYS and analytical expressions in conjunction with the equivalent circuit. While there are two curves in the above graph, only one is discernable. This is because results from the two methods are the same and their resulting curves superimpose exactly. The device geometry is the same as that described in Figure 4.5 and the device is assumed to be operating in vacuum.

applied AC voltage. Note that this simulation can be performed in the presence of any DC bias below the transducer's collapse voltage. This constraint is inherently met by the finite element model as the solution will not converge if the applied DC voltage is greater than collapse. The graph in Figure 4.14 shows the input impedance obtained from ANSYS superimposed on a prediction of the curve obtained from an equivalent circuit that models the same geometry. The applied DC voltage in this instance was 60 V. Note that the two curves match perfectly, confirming that the model appropriately represents a piston transducer and that the data obtained from said model can be accurately interpreted.

The chart in Table 4.2 lists the elements used in the calculation of the equivalent circuit prediction of Figure 4.14 and the equations that describe them. Since only one transducer element is used in the finite element model, the equation for C_0 represents a single capacitor with an air gap $l_{a0} - u_{DC}$. Furthermore, note that all expressions are analytical except for that of the membrane impedance. This impedance was measured in ANSYS for the structure in question and imported into the equivalent circuit

Element	Variable	Equation
Parasitics	R_{series}, R_{shunt}, C_p	Assumed insignificant
Device Capacitance	C_0	$\frac{\epsilon_0 A}{l_{a0}-u_{DC}}$
Turns Ratio	n	(4.7)
Spring Softening Capacitor	$\frac{-C_0}{n^2}$	(4.8)
Membrane Impedance	Z_{mem}	Obtained Numerically

Table 4.2: Analytical expressions used in the calculation of the equivalent circuit prediction in Figure 4.14. Variables names reference schematic in Figure 4.1.

model. It was necessary to do this in order to obtain a perfect match as the analytical expressions for the membrane impedance do not take the effect of an applied DC voltage into account. This does not imply, however, that the expression derived in (4.3) yields values that are significantly different from their actual values under DC bias. This point is made in the graph of Figure 4.15a where the analytically derived membrane resonance is shown to deviate from the one obtained using FEA when under bias by less than 6%.

The results of a further study into the behavior of a CMUT membrane under various conditions is shown in Figure 4.15b - d. First, in (b), a verification of the analytical equation for membrane impedance under zero bias is presented. Here again the curves generated analytically and from finite element results match so well that they are difficult to distinguish from one another. In order to facilitate the comparison, the region from 100 kHz to 1 MHz is plotted in (c). Note that the agreement improves as the frequency increases. This can be understood by considering the series inductor-capacitor model of a CMUT membrane alluded to in Figure 4.7 and 4.9. At lower frequencies the impedance is dominated by the capacitor which represents the stiffness of the membrane. Conversely, at higher frequencies the impedance is dominated by the inductor which represents the mass of the membrane. In both the analytical and finite element simulations, the mass of the membrane can be accurately modeled; the stiffness is a function of the assumptions inherent to each model and is therefore different. Therefore, the results converge when the inductive term dominates the equation.

In order to drive this point home the curve in (d) is shown where the membrane

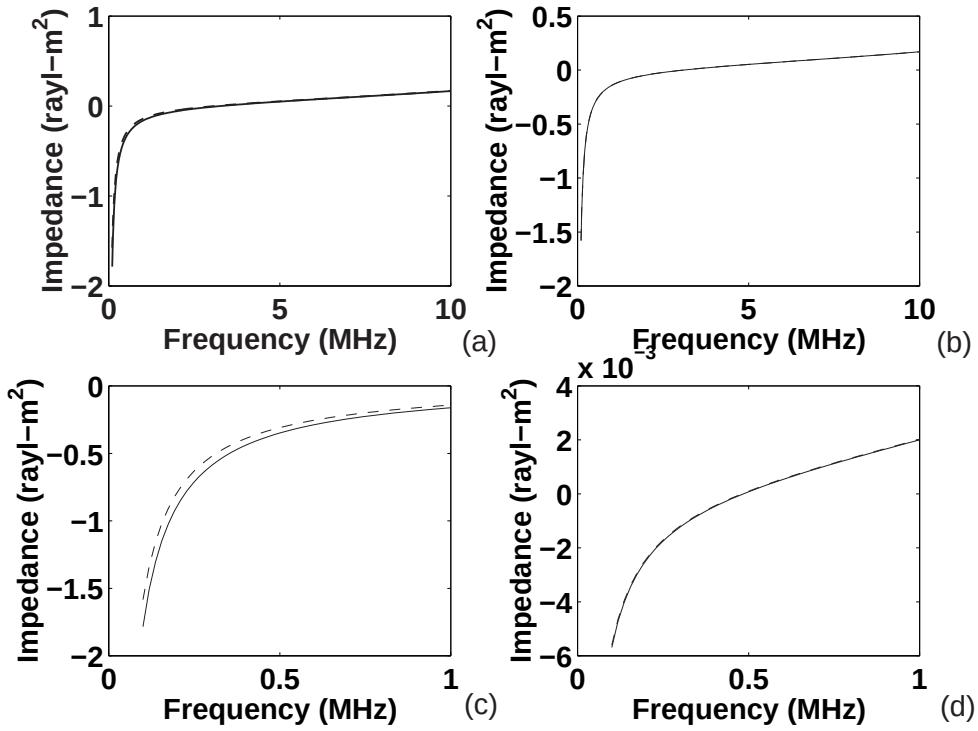

Figure 4.15: Membrane impedance under various conditions. In all cases the membrane width is 60 μm and is assumed to be vibrating in a vacuum. For (a) - (c) the membrane thickness is 1.34 μm. (a) Analytical (solid) and FEA (dashed) results when the membrane is under bias; (b) Analytical (solid) and FEA (dashed) results when the membrane is *not* under bias. Although only one curve is discernable, there are two present in the figure; (c) A zoom of the previous graph to show the two curves; (d) Analytical (solid) and finite element (dashed) result when the membrane thickness is reduced to 0.2 μm.

thickness is .2 μm. Compared to the thicker membrane, the agreement in impedance between analytical and finite element simulations is significantly better in the low frequency region. This is because the membrane stiffness becomes less significant as the membrane thickness decreases.

4.4.3 Expanding the Finite Element Model

With confidence in the finite element model of a CMUT, the next step is to expand the model in order to make it more realistic. This is done in two ways. First, the

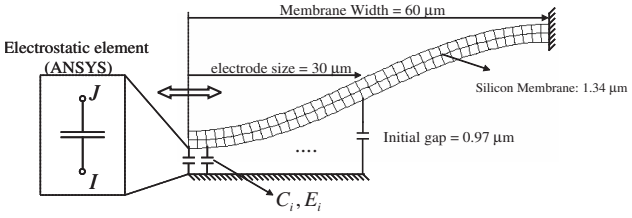

Figure 4.16: A series of TRANS126 elements are used in ANSYS to correctly model a CMUT.

single transducer element coupled to the membrane center is replaced by a series of elements along the membrane. The width of each element corresponds to the distance between the nodes to which they attach. This process is illustrated in Figure 4.16 and the resulting data is considered to be the most accurate of the three models (piston, distributed, finite element) described in this dissertation. As a point of reference, the input impedance obtained using the finite element method is superimposed on the impedance plots obtained from the other two methods and is shown in Figure 4.17. Again, the real part is not shown because there is no loss in the system and it is therefore equal to zero.

One thing to note in this last figure is the position of the distributed curve in relation to the other two. Recall that it was derived in an effort to create an analytical model more accurate than the piston model. Working under the assumption that the finite element result is the most accurate of the three, the effort appears to have been successful. This conclusion is based on the fact that the distributed result is both in between the other two and the resonances are much closer in value to those obtained from the finite element model. Quantitatively, the open circuit resonances differ by only 2.5%.

The second step in model expansion is to put the transducer on top of a substrate. This is done using a finite element mesh similar to the one depicted in Figure 4.18. Since the purpose of the analysis is to characterize wave propagation in the substrate, a lossy section is included at the ends to absorb the incoming energy. This is necessary in order to prevent a reflected wave from interfering with the acoustic wave of interest [14, 61, 105]. The loss coefficient of the lossy region is carefully chosen to minimize

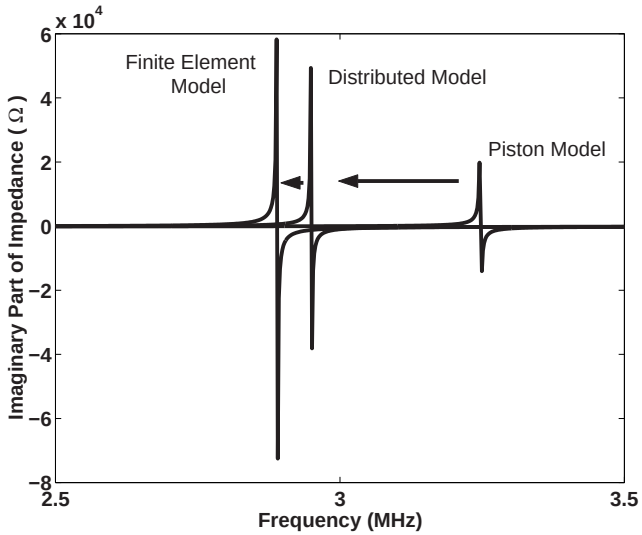

Figure 4.17: A comparison between the CMUT input impedance results obtained using the piston, distributed, and finite element models. The curves representing the piston and distributed models are identical to the ones shown in Figures 4.8 and 4.11.

the creation of a standing wave pattern due to reflections at the silicon/lossy-silicon interface. This is difficult to do for Lamb wave devices with smaller substrate thicknesses if both the A_0 and S_0 modes are to be detected; the latter mode has a relatively longer wavelength than the former which necessitates a longer lossy region to fully absorb its propagating wave. The short wavelength of the A_0 mode, however, requires a finer mesh to fully capture its behavior. These two requirements would result in a long lossy region with a fine mesh, in effect a recipe for exorbitantly long computation times. In order to avoid this situation, a compromise is reached using a fine mesh in conjunction with a larger loss coefficient and a slightly shorter lossy region.

The presence of the substrate introduces a source of loss to the membrane as energy from its vibrations transfer into the substrate. This transfer is of course important for this dissertation as it allows for the transduction of Lamb waves in the silicon substrate. From a theoretical point of view, adding a substrate to the model allows for finite values of $R_{substrate}$ in the equivalent circuit model of 4.12. As shown in the next section, this allowance results in finite values for the real part of the device input impedance.

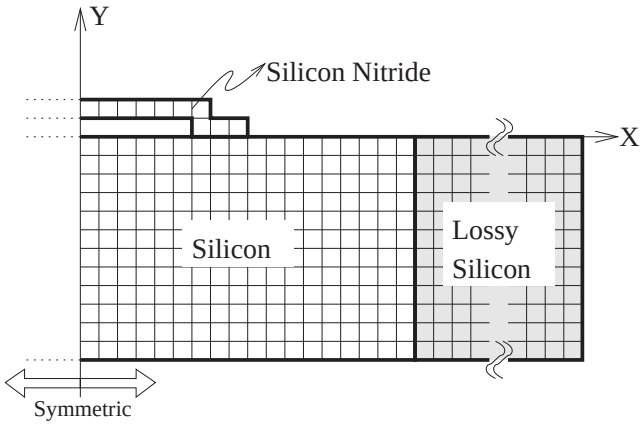

Figure 4.18: Abstract finite element representation of a CMUT placed on a substrate. This particular model is for the sacrificial layer method of device fabrication. A similar one can be made for the wafer bonding method.

4.5 Using The Finite Element Model

The goal of this section is to present the data obtained from a finite element model used to describe the Capacitive Micromachined Ultrasonic Lamb Wave transducer. The model follows from the previous section where a series of transducer elements is used to model the electrostatic effects of the CMUT and the device is placed on a substrate of finite thickness.

A tool often used to aid in the analysis presented in this section is normal mode decomposition. This section therefore begins with an introduction to normal mode theory and how it can be used to decompose FEA results to solve for the power in propagating Lamb wave modes. The section continues with a discussion of the finite element structure and some tricks associated with modeling the Lamb wave device in the presence of air. The data presentation then begins with impedance graphs that show the familiar resonance behavior of a CMUT as well as the effects of a device substrate. This electrical characteristic is related to the mechanical behavior of the device by analyzing both the membrane displacement and the power in the two Lamb wave modes present in the substrate. The electrical and mechanical data are then manipulated to obtain values for the device conversion loss. The section continues with a derivation of values for $R_{substrate}$ for various substrate thicknesses.

FEA	Analytical
V_x	V_{x_n}
V_y	V_{y_n}
T_{xx}	T_{xx_n}
T_{xy}	T_{xy_n}

Table 4.3: Values for variables in (4.31) are available from finite element analysis (FEA) or analytically.

The results lend credence to the claim that device efficiency improves as the substrate thickness decreases. A discussion of the Lamb wave excitation mechanism in relation to device posts is then presented, followed by an analysis of reflections along the device substrate.

4.5.1 Normal Mode Theory and Decomposition

According to normal mode theory [5, 19], any arbitrary velocity field $\mathbf{v}$(x,y) and associated stress distribution $\mathbf{T}$(x,y) with mode amplitude a_n can be expressed as a sum of normal modes (each denoted with the subscript n)

$$\mathbf{v}(x,y) = \sum_{n=0}^{\infty} a_n(x)\mathbf{v}_n(y) \tag{4.22}$$

$$\mathbf{T}(x,y) = \sum_{n=0}^{\infty} a_n(x)\mathbf{T}_n(y) \tag{4.23}$$

that obey the orthogonality relation

$$\int_{x-section} (-\mathbf{v}_n^* \cdot \mathbf{T}_m - \mathbf{v}_m \cdot \mathbf{T}_n^*) = \begin{cases} 4P_{nn} & \text{if } n = m \\ 0 & \text{otherwise} \end{cases} \tag{4.24}$$

In this equation P_{nn} represents the total time average power flow in the lateral direction associated with the nth mode in the plate at the plane of integration. Mathematically,

$$P_{nn} = -\frac{1}{2}\mathcal{R}e\left(\int_{-h}^{0}\left(v_{x_n}^{*}T_{xx_n} + v_{y_n}^{*}T_{xy_n}\right)dy\right) \tag{4.25}$$

Note that tensor notation is used here. This means that in the term T_{ab}, the first subscript (a) denotes the coordinate axis normal to a plane upon which the stress is placed, while the second denotes the axis to which the source of the stress is parallel.

In an effort to solve for the mode amplitudes, the mathematical progression below is used. Recall that the terms without subscripts are the arbitrary velocity and stress fields described in (4.22) - (4.23).

$$\begin{aligned}
\int\limits_{x-section}(-\mathbf{v}_n^{*}\cdot\mathbf{T}-\mathbf{v}\cdot\mathbf{T}_n^{*}) &= \int\limits_{x-section}\left(-\mathbf{v}_n^{*}\cdot\sum_{m=0}^{\infty}a_m(x)\mathbf{T}_m\right. \\
&\quad \left.-\sum_{m=0}^{\infty}a_m(x)\mathbf{v}_m\cdot\mathbf{T}_n^{*}\right) && (4.26)\\
&= \int\limits_{x-section}(-a_n\mathbf{v}_n^{*}\mathbf{T}_n - a_n\mathbf{v}_n\mathbf{T}_n^{*}) && (4.27)\\
&= a_n\int\limits_{x-section}\underbrace{(-\mathbf{v}_n^{*}\mathbf{T}_n-\mathbf{v}_n\mathbf{T}_n^{*})}_{4P_{nn}} && (4.28)
\end{aligned}$$

Therefore, if $\mathbf{v}$ and $\mathbf{T}$ can be written as a sum of normal modes,

$$\int\limits_{x-section}(-\mathbf{v}_n^{*}\cdot\mathbf{T}-\mathbf{v}\cdot\mathbf{T}_n^{*}) = 4a_nP_{nn} \tag{4.29}$$

$$a_n = \frac{1}{4P_{nn}}\int\limits_{x-section}(-\mathbf{v}_n^{*}\cdot\mathbf{T}-\mathbf{v}\cdot\mathbf{T}_n^{*}) \tag{4.30}$$

$$a_n = -\frac{1}{4P_{nn}}\int_{-h}^{0}(\mathbf{v}_{x_n}^{*}\mathbf{T}_{xx}+\mathbf{v}_{y_n}^{*}\mathbf{T}_{xy}+\mathbf{v}_x\mathbf{T}_{xx_n}^{*}+\mathbf{v}_y\mathbf{T}_{xy_n}^{*})dy \tag{4.31}$$

As illustrated in Table 4.3, the variables in (4.31) are comprised of two categories: orthogonal mode field distributions (denoted with the subscript n), and propagating wave field distributions. Equations describing the former category are available in the

literature[1]. Values for the latter are available from results obtained using Finite Element Analysis. Using the above expressions, [19] shows that the average propagating power in a wave mode, P_n, can be written as

$$P_n = |a_n|^2 P_{nn} \tag{4.32}$$

The fundamental assumption in this formulation is that the propagating wave modes are orthogonal to one another; Lamb wave modes obey this relationship. In the frequency range of interest for relevant device geometries, only A_0 and S_0 modes can propagate. The power contained in these modes have been calculated using the relationships described above and will be presented in the next section.

4.5.2 Modeling The Lamb Wave Device In Air

When electrical energy is applied to the input of a Lamb wave device, some fraction of it is lost into air. It is therefore important to understand how the geometry of the device can be optimized in order to minimize this loss and therefore maximize the energy coupled into the substrate. This section describes how the modeling is done.

The traditional way to model a 2-D structure in the presence of air using Ansys is to surround it by a hemisphere of Fluid29 elements. While this approach significantly adds a large number of elements to the model (and therefore equations that describe it), the original structure is normally quite small and the computation time involved is feasible. In the case of the Lamb wave devices described in this chapter, however, the hemisphere approach cannot be used. This is because the large lossy regions described in Section 4.4.3 have already pushed the computation time to its feasible limits. As a result, an alternate method to model a Lamb wave device in air is investigated.

The loss of energy from the membrane into air can be modeled by applying the damping material property to the membrane elements in Ansys. While this method affects the terms in the equations that are used to analyze the structure, it does

[1]Expressions for the particle velocity for both symmetric and anti-symmetric modes are given in [5] (equations 10.22-23). Expressions for $\mathbf{T}$ can be calculated from this velocity using the expressions $\mathbf{S} = \nabla\ \mathbf{u}$ and $T_{ij} = c_{ij}\ S_j$.

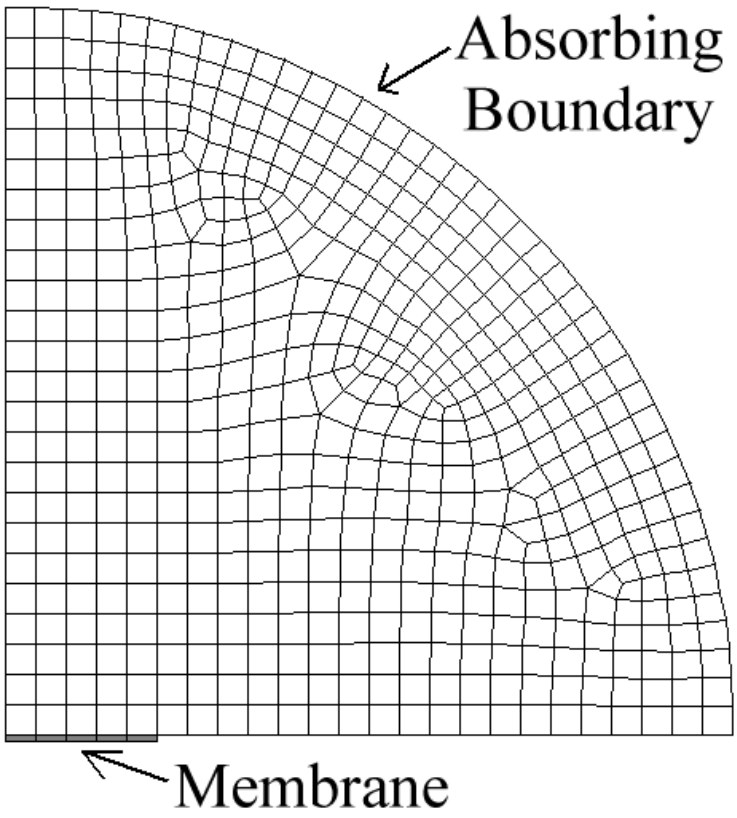

Figure 4.19: Mesh used in the finite element representation of a membrane in air.

not increase the number of equations. The key to this approach, of course, is to determine the value of the damping coefficient that is applied to the model. This is done using the finite element mesh shown in Figure 4.19 where a CMUT membrane of the appropriate dimensions is surrounded by Fluid29 elements. The displacement of the membrane as a function of frequency is then measured and considered to be the correct response of a membrane in air. The fluid is then removed and the simulation is repeated to obtain the displacement characteristic of the membrane in a lossless environment. The simulation is then re-run in a vacuum but now the damping coefficient is introduced and adjusted so that the first membrane displacement curve is replicated. A graph containing the results of the three simulations is shown in Figure 4.20.

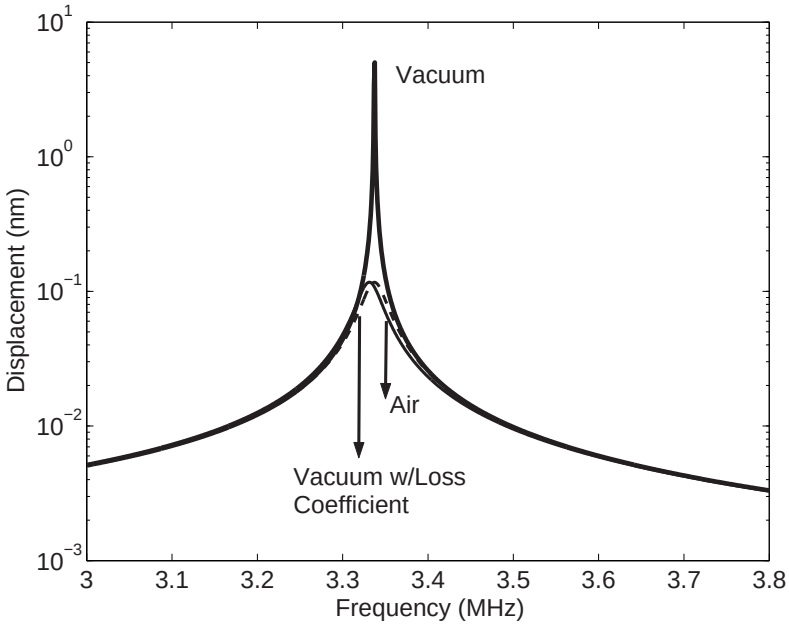

Figure 4.20: The three curves used to determine the value of the damping coefficient for the membrane material property in Ansys.

4.5.3 Basic Electrical and Mechanical Characteristics

The input impedance of a CMUT on an 8 μm substrate is shown in Figure 4.21. As before, this curve was found using ANSYS by extracting the current drawn by the transducer elements and determining its ratio to the known applied AC voltage. Note that the short circuit resonance is equal to 2.73 MHz. Furthermore, as expected the real part of the impedance is no longer equal to zero.

The displacement of the CMUT membrane as a function of frequency has also been obtained and is shown in Figure 4.22. The curve exhibits the familiar resonant characteristic and has its maximum displacement at 2.73 MHz, the short circuit resonant frequency of the device.

The normal mode decomposition technique described in the previous section is used here to calculate the power in the two Lamb wave modes along a cross-section of the substrate. Recall that energy from the vibrating membrane couples energy through the supporting posts into the substrate. One would therefore expect that the frequency of maximum Lamb wave power be equal to the frequency of maximum

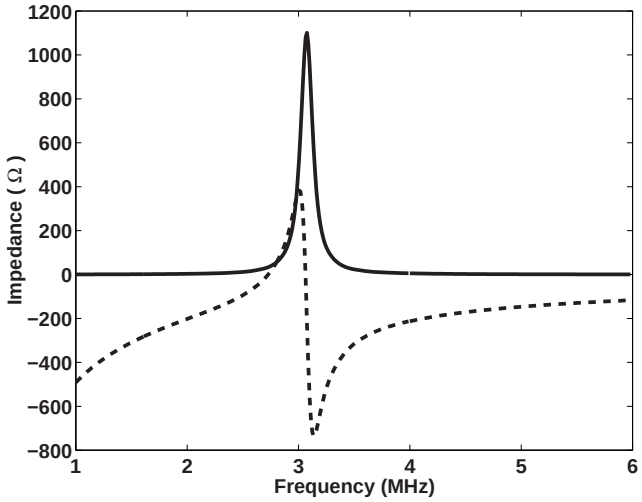

Figure 4.21: Real (solid) and imaginary (dashed) parts of the input impedance of a Lamb wave device consisting of a CMUT on an 8 μm substrate with a 60 μm wide membrane. The short circuit resonance is at 2.73 MHz.

	Harmonic	Modal
First-Order	1.18 MHz	2.43 MHz
Second-Order	12.3 MHz	13.05 MHz

Table 4.4: Resonant frequencies using harmonic and modal analyses.

membrane displacement. The curves in Figure 4.23 show that this is indeed the case with the curves for both the A_0 and S_0 modes peaking at 2.73 MHz. This graph shows that the method of excitation greatly favours the A_0 mode; over 95% of the Lamb wave power is in this mode.

While most of this dissertation is concerned with the fundamental resonance of the CMUT, one should understand that higher order modes do exist. Using a structure similar to the one considered above, but neglecting the effect of the insulation oxide on the device capacitance, a harmonic analysis was performed to obtain both the first and third order resonances of the Lamb wave power along a substrate cross-section. The results are presented in Figure 4.24.

This plot exhibits a number of interesting characteristics. First, it contains evidence of spring-softening. Recall from the discussion in the previous section that

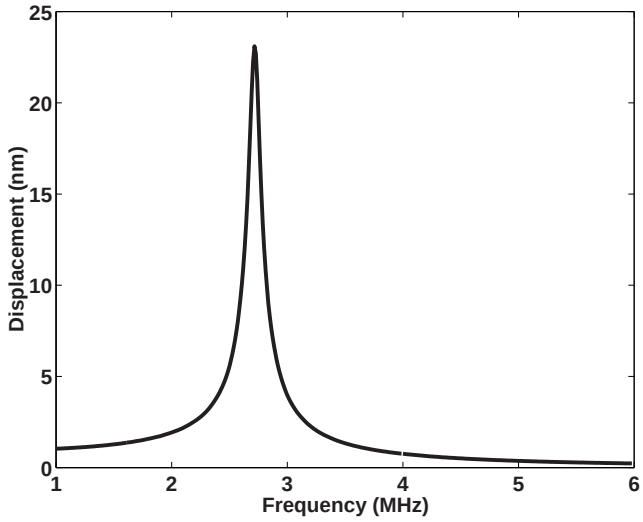

Figure 4.22: Membrane displacement of a Lamb wave device consisting of a CMUT on an 8 μm substrate. The frequency of maximum displacement is 2.73 MHz.

the maxima in this graph correspond to the resonant frequencies of the membrane. However, as shown in Table 4.4, the resonant frequencies predicted from a modal analysis of the membrane are higher than the frequency of the peaks in the Lamb wave power. This difference is the result of an applied DC voltage that decreases the resonant frequency of the device.

Second, the resonant frequencies are not integer multiples of each other. This is because the membrane resonates at frequencies where the wavelength is a half-integer multiple of its width. The membrane is a thin plate, and as a result its wavelength is described by the dispersive Lamb wave equations. Therefore, since there is a non-linearity between frequency and wavelength, the values of $\frac{\lambda}{2}$, λ, and $\frac{3\lambda}{2}$ will be non-linear as well.

Finally, this curve does not exhibit any evidence of a second-order resonance. This is because the excitation mechanism (uniform force over half the membrane) does not support the flexure corresponding to the membrane shape of this resonance.

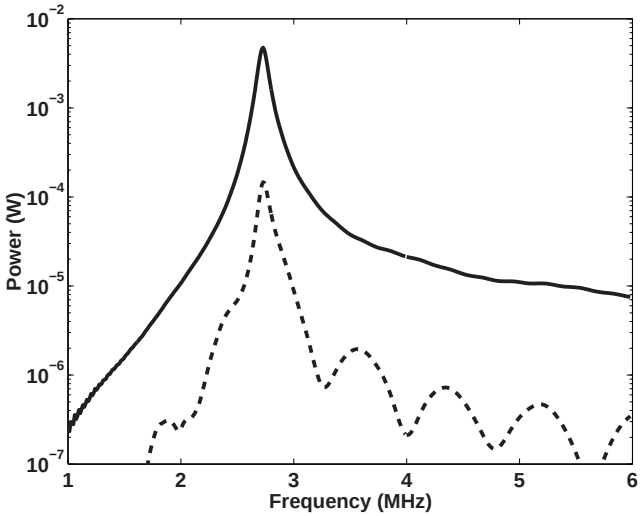

Figure 4.23: Power in the A_0 (solid) and S_0 (dashed) modes along a cross-section of the device. The frequency of maximum Lamb wave coupling is 2.73 MHz. Furthermore, over 95% of the power is in the A_0 mode.

4.5.4 Device Conversion Loss

This dissertation defines the device conversion loss as the ratio between the electrical power put into the device and the mechanical power measured along its cross-section. The former is determined from a measurement of the electric current sourced by a known AC voltage while the latter is obtained using normal mode analysis as reflected in the data of Figure 4.23. A graph of both curves superimposed on one another is shown in Figure 4.25. As expected, the value of the input electrical power is greater than the output acoustic power. Quantitatively, they differ by approximately 5.5 dB at the resonant frequency. Note that since acoustic energy is launched in both directions away from the transmitting CMUT, the minimum loss that can be obtained along any cross-section is 3 dB.

Assuming that the device is reciprocal in terms of electro-mechanical conversion, the total device conversion loss is the sum of the two one-way values, or 11 dB. This suggests that under optimal conditions, the miminum insertion loss that can be attained for a Lamb wave device built using CMUT technology with the dimensions shown in Figure 4.5 on an 8 μm substrate is also 11 dB.

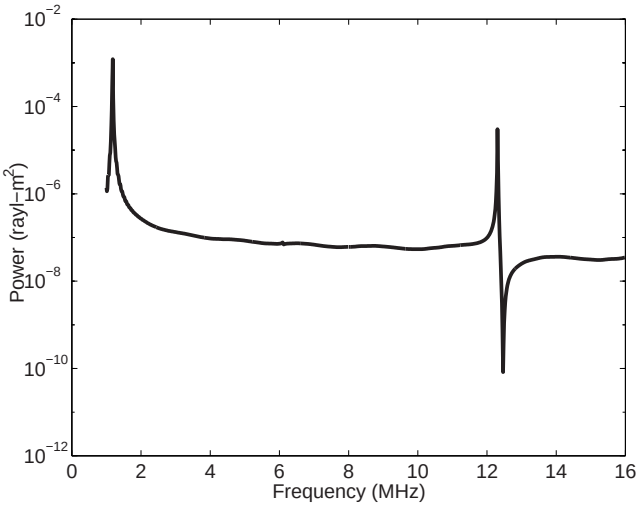

Figure 4.24: Total Lamb wave power showing both first and third order resonances.

4.5.5 Analyzing the Transduction Mechanism

Recall from Section 4.3 that the impetus behind using the finite element method to analyze capacitive micromachined ultrasonic Lamb wave devices is the lack of a closed form solution describing the load presented to the CMUT membrane by the substrate. While the data presented in the recent figures represent the effect of substrate loading on the device, it is instructive to obtain values for $R_{substrate}$, the circuit element in the schematic of Figure 4.12 that describes this loading. The method used to extract these values is described below. The most important result is confirmation that device performance improves with decreasing substrate thickness.

Note that since the "current" in the mechanical part of the circuit in Figure 4.12 is the membrane velocity, it is important that the definition of $R_{substrate}$ be consistent with this convention. To that end, if P_n is the average propagating power of the nth Lamb wave mode excited by a membrane with average velocity $\overline{v}$, the expression in (4.33) can be written for $R_{substrate}$. The assumption in this formulation is that all of the energy coupled to the substrate is in the form of a propagating mode; for this reason the right hand side of (4.33) is purely real. The subscript n corresponds to

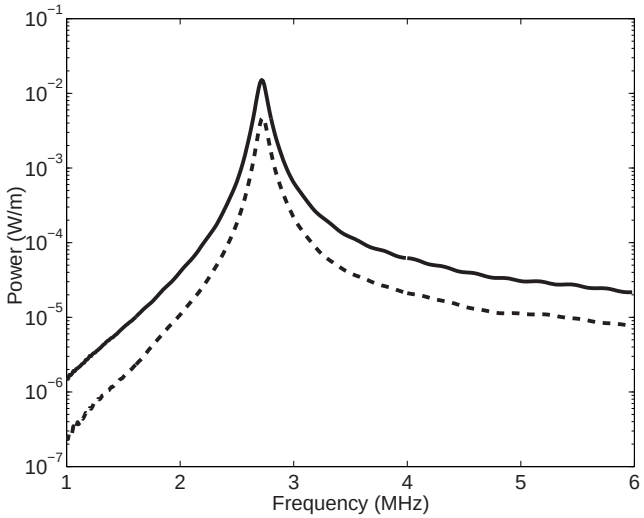

Figure 4.25: Electrical power (solid) into the device and acoustic power (dashed) along a cross-section of the substrate.

the Lamb wave mode for which the resistance is being solved.

$$R_{substrate_n} = \frac{2P_n}{|\overline{v}|^2} \tag{4.33}$$

Numerical values for the power and the velocity in this equation can be obtained through a two-step process. The first step involves the use of finite element analysis where both the membrane particle velocity v and the stress distribution T across the thickness of the silicon wafer are determined. In the second step this data is used to determine the power in the Lamb wave by applying it to the Poynting vector for a propagating Lamb wave:

$$\begin{aligned} P_{avg} &= \frac{1}{2}\mathcal{R}e\left\{-\mathbf{v}^* \cdot \mathbf{T}\right\} \cdot \mathbf{x} \\ &= -\frac{1}{2}\mathcal{R}e\left\{v_x^* T_{xx} + v_y^* T_{xy}\right\} \end{aligned} \tag{4.34}$$

The graph in Figure 4.26 shows the resistance presented to the membrane by the A_0 mode for Lamb wave devices built using the sacrificial layer method (the graph has similar shape and values for wafer bonded devices) for various substrate thicknesses.

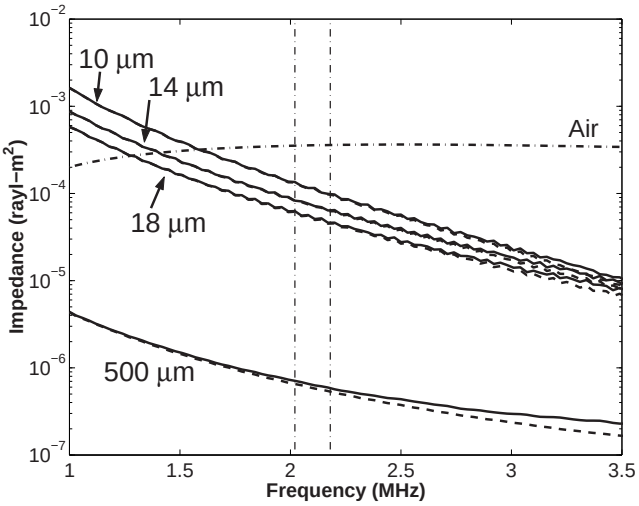

Figure 4.26: Resistance presented to the membrane by the Lamb wave (solid) and A_0 mode (dashed) for 10, 14, 18 and 500 μm substrates. The real part of the air impedance as expressed in (4.6) is also shown as a point of reference. The vertical lines represent the resonant region of the device.

The slight ripple present on some of the curves is a manifestation of reflections due to the compromise between the larger loss coefficient and the shorter lossy region. For reference, the real part of the air impedance as described by (4.6) is also shown on the graph. The 10 μm plate presents a resistance that is two orders of magnitude larger than that of the thicker 500 μm substrate. Furthermore, the device impedance for the thinner case is now significant relative to the air impedance. This strongly suggests an increase in the amount of energy coupled into the Lamb wave mode and thus better device performance. This finding is consistent with the design of other Lamb wave devices described in the literature that have substrate thicknesses much thinner than the ultrasonic wavelength.

Inherent to the definition presented in (4.33) for $R_{substrate}$ is the fact that the vibrating membrane is source of energy of the Lamb wave. This can be verified using FEA/normal mode analysis on the structure illustrated in Figure 4.18. The graph in Figure 4.27 shows the power coupled into the A_0 mode when forces act on the device electrodes in three different configurations. In the first configuration, where the forces are on both the top and bottom electrodes, the curve shows a resonant behavior

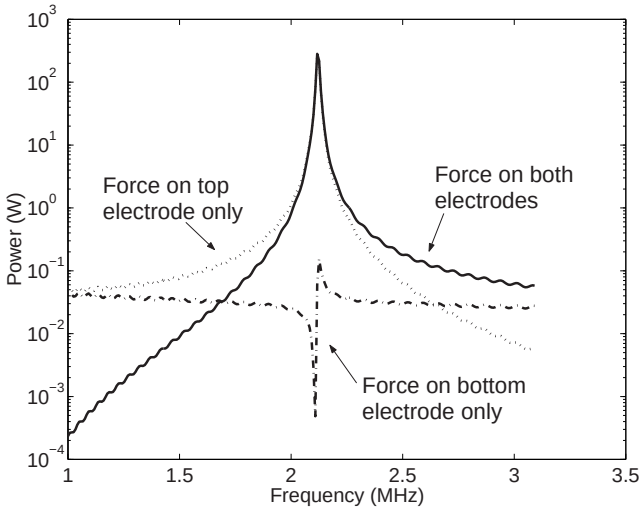

Figure 4.27: Power coupled into the A_0 mode of the substrate using three different excitation mechanisms. Only the relative value of the different curves is important in this figure. The absolute numbers are a function of the arbitrarily chosen forces applied in the finite element model.

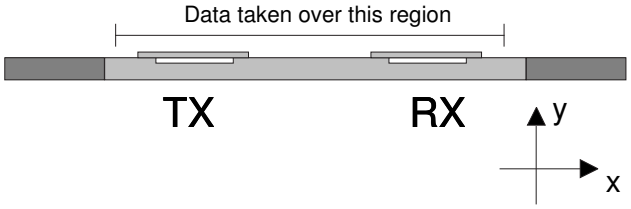

Figure 4.28: Data in Figure 4.29 is taken along the membrane/substrate interface over the region specified above.

with maximum power delivered to the substrate at the resonant frequency of the membrane. In the second configuration, where the forces act on the top membrane only, almost the same amount of power is transferred to the substrate at frequencies at and around the membrane resonance. In contrast to these two cases, the energy coupled into the Lamb wave is at least three orders of magnitude smaller when the force is applied to only the bottom electrode. This graph thus clearly shows that the source of most of the energy in the Lamb wave is indeed the vibrating membrane, and that the energy is coupled through the supporting posts into the substrate. Since 95% of the energy coupled into the Lamb wave is in the A_0 mode, the curves for the

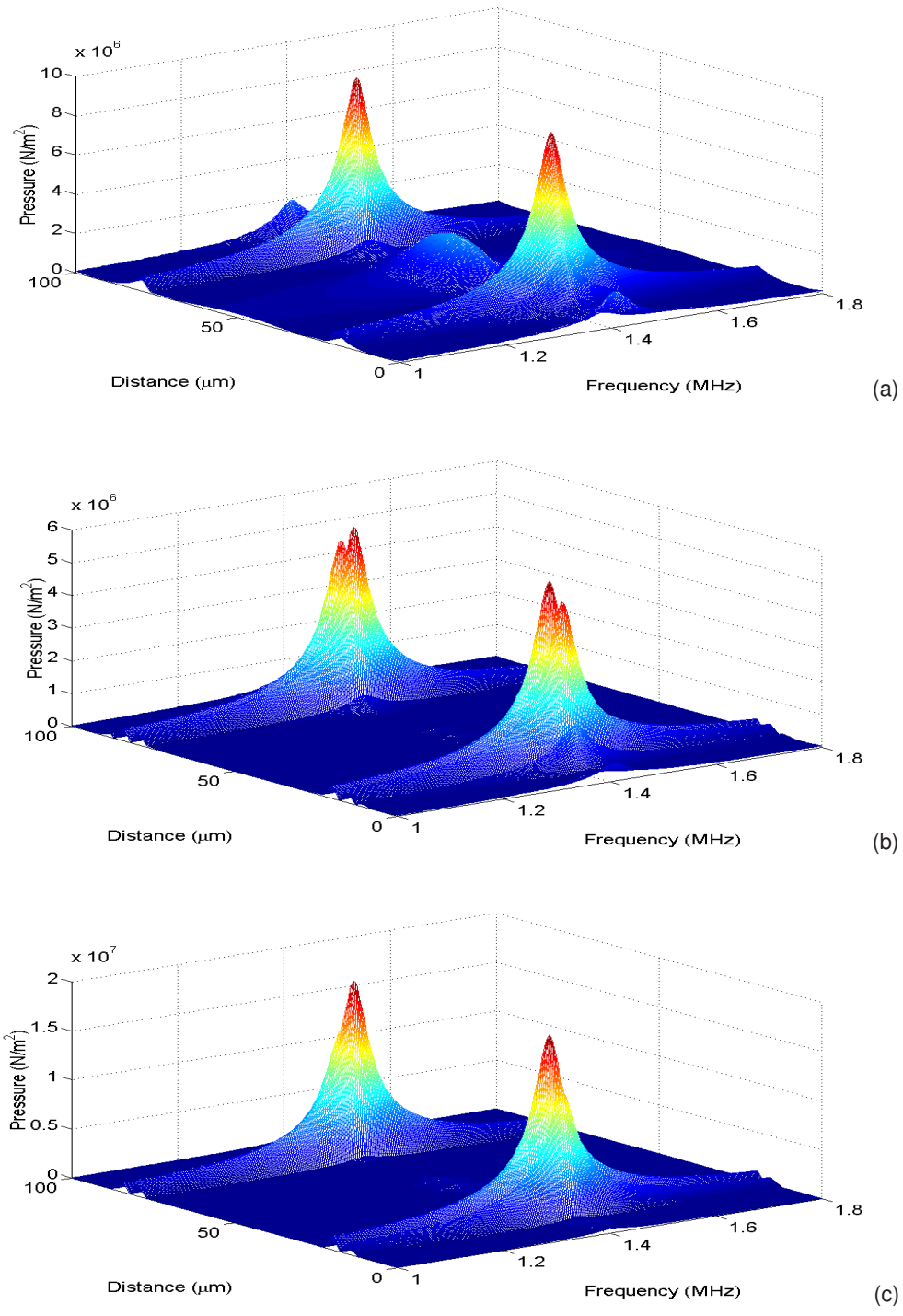

Figure 4.29: Stresses measured along the membrane/substrate interface as shown in Figure 4.28. (a) T_{xx}, (b) T_{xy}, (c) T_{yy}.

S_0 case are not included in Figure 4.27.

Further analysis of the behavior relating to the posts of the device yields stress data along the membrane/substrate interface shown in Figure 4.29. The peaks in each graph correspond to the region around the two posts, reflecting the high stress introduced to that area by the vibrating membrane. It is this stress that acts as the source of the Lamb waves that are launched into the substrate. The data in the region between the two peaks represents the bottom of the membrane. Values for T_{xx} reach a maximum in the middle, reflecting the inherent tension in the membrane as a result of membrane deformation. Although it is not apparent from the graph of T_{yy}, it has similar values in this region; here the pressure is due to the electrostatic attraction of the membrane to the substrate introduced by the applied DC voltage.

4.5.6 Effect of Absorbing Boundaries

As discussed in Section 4.4.3, an absorbing boundary is added to the finite element model in an effort to prevent reflected waves from interfering with the acoustic waves launched from the transmitting CMUT. This section demonstrates the effectiveness of the added boundary.

The graph in Figure 4.30 includes a prediction of the device insertion loss from a transient analysis using FEA. Note that the solid curve, representing the case where the absorbing boundaries are included, is smooth (as are most of the curves presented in this chapter). The dashed curve is not, however, demonstrating the effect of removing the absorbing boundaries and allowing the incident wave to be reflected off of the edge of the device. The peaks that result are due to standing wave patterns that are formed between the edge of the device and various structures on top of the wafer as well as between the structures themselves. For example, many of the peaks are separated by 132 kHz; for a Lamb wave on an 8 μm substrate this corresponds to a velocity of 127 m/s, a wavelength of 962 μm, and therefore a half-wavelength of 0.481 mm. Not surprisingly, the distance between the edge of the device and the CMUT closest to the edge in the finite element model is 0.48 mm.

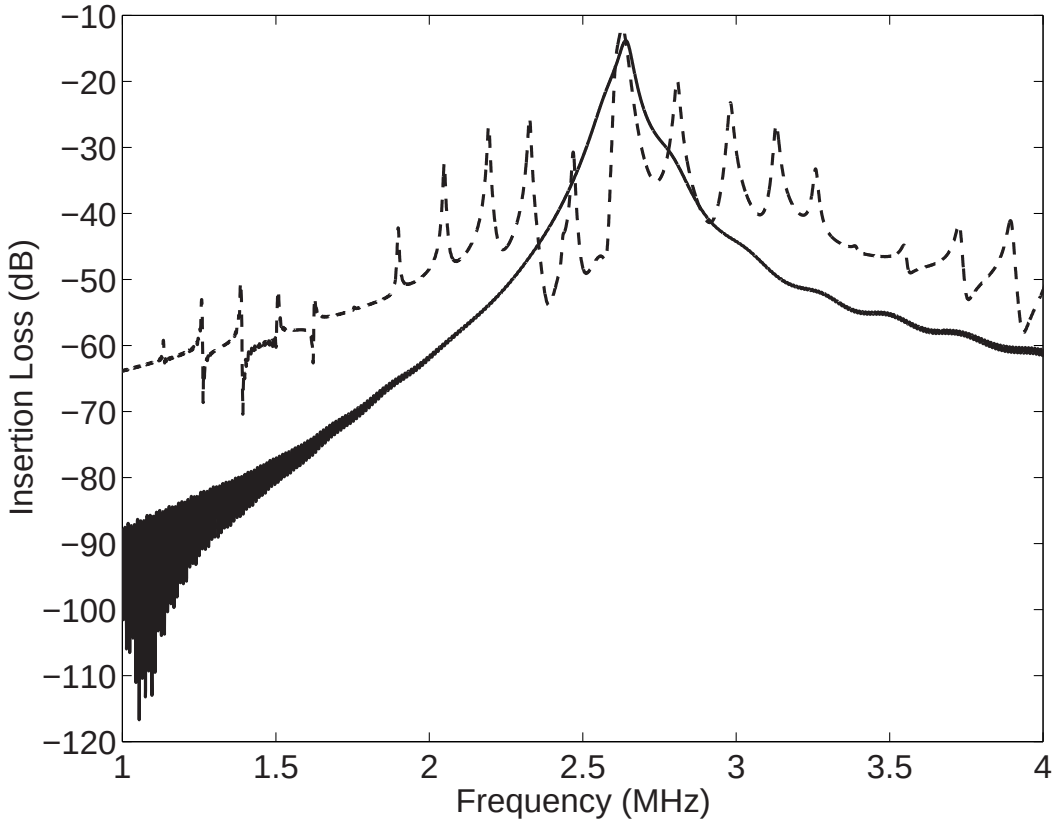

Figure 4.30: Insertion loss predicted from a transient analysis using FEM. Data is presented for a structure with absorbing boundaries (solid) and without (dashed).

Chapter 5

Manufacturing Process

The manufacturing process of the Capacitive Micromachined Ultrasonic Lamb Wave Transducer borrows significantly from CMUT technology. This chapter describes the two main manufacturing methods used to create the devices described in this dissertation: the sacrificial layer method and the wafer bonding method. The goal of both methods is to create a thin membrane over a gap of a designed thickness. The sacrificial layer method is the surface micromachined process used to build CMUTs. It involves the removal of a layer of patterned polysilicon after having deposited the silicon nitride membrane [7, 25, 42]. The wafer bonding method, a newer and superior process, uses bulk micromachining and involves the fusion bonding of the device layer of an SOI wafer on top of a trench created in a base wafer [36].

It should be understood that the main differences between the process flows of a CMUT and the Lamb wave devices described in this dissertation lie in the final steps where the substrate around the CMUT membranes are wet etched to a specified thickness. This added step does affect the rest of the process, however, as the materials and geometry that make up the CMUTs must be compatible with the final etch. In the course of this research numerous process runs were completed, each involving changes in the device geometry in an effort to optimize the manufacturing process and the performance of the Lamb wave device. To facilitate the explanations of the two manufacturing methods, this chapter presents illustrations, microscope stills, and SEM pictures of wafers processed from these different runs. The chapter concludes

with a comment on the merits of the wafer bonding method through an analysis of the mask count, membrane yield and membrane performance. Unless specifically noted, all processing steps were performed in the Stanford Nanofabrication Facility (SNF) at Stanford University.

5.1 The Sacrificial Layer Method

The processing steps of the sacrificial layer method are shown in Figure 5.1 and outlined in Appendix A. The base substrate of the device is a (phosphorous) n-type (100) 4-inch silicon wafer with a resistivity in the 1-10 Ω-cm range. The TTV (total thickness variation) specification of the wafer is less than 3 μm, a necessity for a uniform finish of the thinned substrate upon which the Lamb waves will propagate. The first step in the process is to heavily dope the wafer using a liquid source of phosphorous oxychloride ($POCL_3$) to lower the sheet resistance at the wafer surface to 1-2 Ω/square. This layer acts as the bottom electrode of the capacitor structure, and although it is very important, it has been left out of the drawings in Figure 5.1 for the sake of clarity. The doping is followed by a short HF dip to remove any oxide that is grown while the wafers are in the tube. As illustrated in Figure 5.2, the doping reaction leaves behind an unknown by-product on the wafer surface. The microscope stills show that this by-product has a finite height over the surface of the wafer and that it is brittle; it can be scratched off by a pair of tweezers. This action is of course not the ideal way to remove the growth. Trial and error has demonstrated that the best way to remove it is with a 20 minute piranha (sulfuric acid:hydrogen peroxide ratio of 9:1) dip.

After the doping step and subsequent piranha clean, films of LPCVD low stress silicon nitride (dichlorosilane (DCS) to ammonia (NH_3) ratio of 14:1) and polysilicon are deposited on to the wafer surface [Figure 5.1a]. The former layer has a thickness of 2500 Å and acts as both the etch stop for an upcoming potassium hydroxide (KOH) sacrificial etch, as well as an insulation layer between the ground plane and the membrane of the completed device. The latter film has a thickness of 1 μm and is the material that will be removed in the sacrificial etch . The reaction formulas for

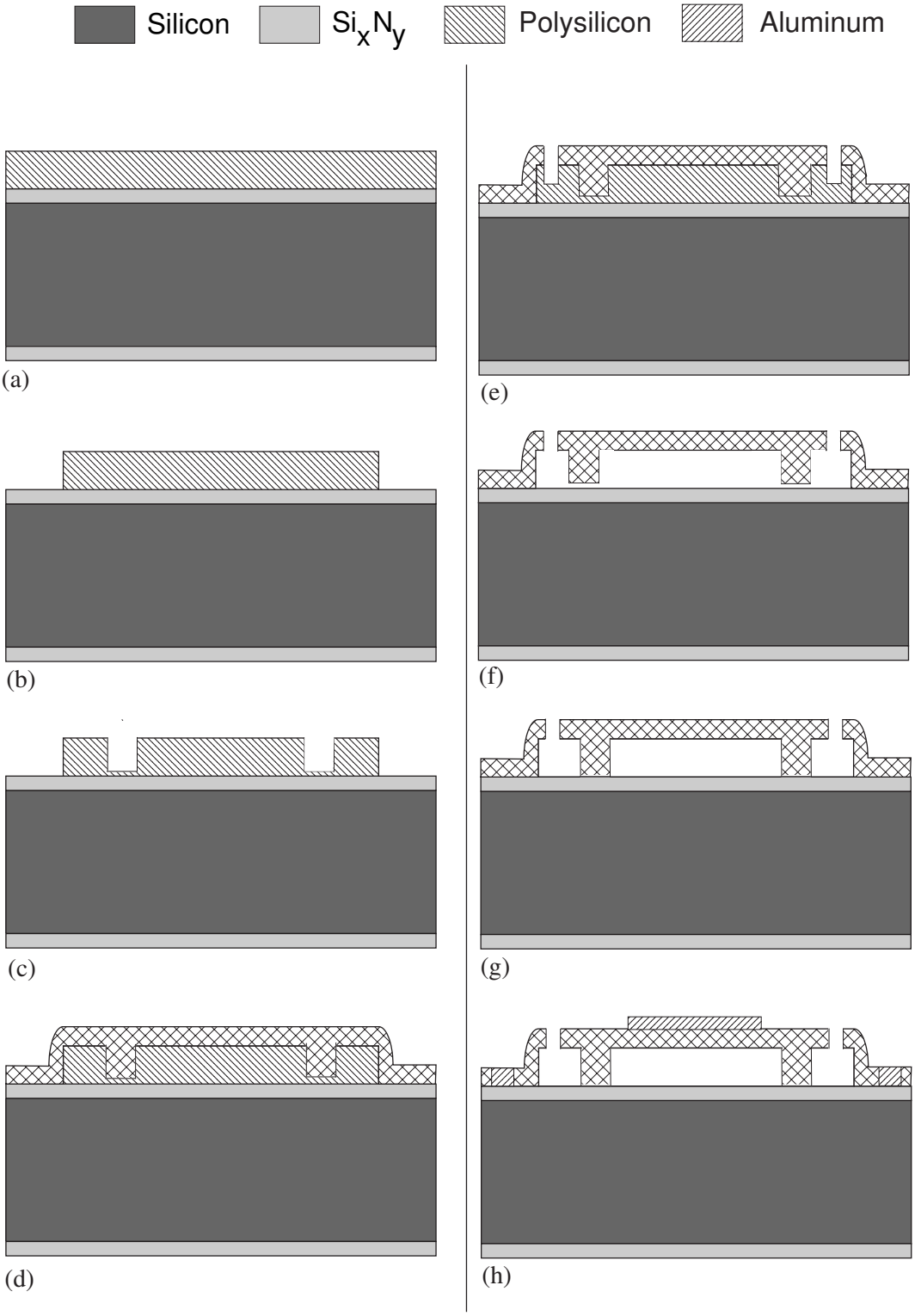

Figure 5.1: Process steps of the capacitive micromachined ultrasonic transducer manufacturing process using the sacrificial layer method. A single transducer is shown in the picture above.

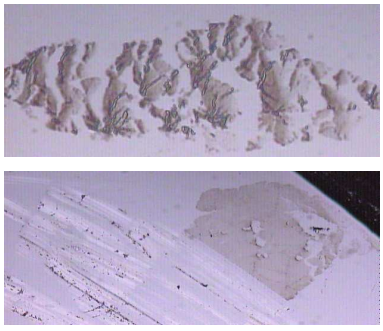

Figure 5.2: Stills of the wafer surface after doping; (a) A 20X magnification of the growth on the wafer surface left by the doping process; (b) The surface after being scratched by a pair of tweezers.

both films are shown below [68].

$$3SiH_4 + 4NH_4 \rightarrow Si_3N_4 + 12H_2 \quad (5.1)$$

$$SiH_4 \rightarrow Si + 2H_2 \quad (5.2)$$

The first mask (MASK #1) is now introduced and the polysilicon layer is patterned to define the shape of the transducer [Figure 5.1b]. Next, a reactive ion etching (RIE) system is used to create a trench in the polysilicon [Figure 5.1c, MASK #2]. This acts to reduce the thickness of the channel through which KOH will flow during the sacrificial etch, making the subsequent sealing of the channel significantly easier. This concept will be discussed in more detail in relation to Figure 5.1g. A final channel thickness of 1000 Å is usually appropriate. The backside polysilicon is now removed by a blanket RIE system.

At this point in the process a second layer of LPCVD nitride is introduced that will act as the membrane material. The thickness of the film is on the order of 1 μm [Figure 5.1d]. Next, a pattern of etch holes approximately 2 μm in diameter are created through the nitride and part of the polysilicon using an RIE system [Figure 5.1e, MASK #3]. The etching of the sacrificial layer is performed with potassium hydroxide (KOH) that enters the area under the membrane through these holes [Figure 5.1f].

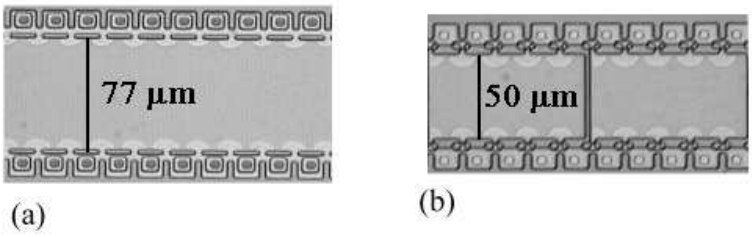

Figure 5.3: Stills of membrane fingers from two different runs at the beginning of the release process. (a) The finger consists of a single membrane 1 cm long; (b) The finger consists of many small membranes 98 μm long, separated by 2 μm.

	Temperature (°C)				
% KOH	20°	40°	60°	80°	100°
10	1.49	6.7	25.2	82	233
20	1.57	7.1	26.7	86	246
30	1.44	6.5	24.4	79	225
40	1.17	5.3	19.9	64	184
50	0.84	3.8	14.2	46	131
60	0.50	2.2	8.4	27	78

Table 5.1: Etch rates of (100) silicon in (μm/hr) for various KOH concentrations and temperatures, after [78].

Microscope stills in Figure 5.3 show sample IDT fingers during the release process. The etching of polysilicon occurs through the following reaction [47]:

$$Si + 2OH^- + 2H_2O \rightarrow SiO_2\,(OH)_2^{2-} + 2H_2 \tag{5.3}$$

It is important that this etch occur at room temperature. This is because the reaction rate is exponentially related to the temperature of the KOH solution (see Table 5.1) [78]. Since hydrogen gas is a by-product of the etch, as the temperature increases so does the pressure underneath the membrane before the gas escapes through the etch holes. Thus, in order to avoid excessive pressure that could break the membrane, it is essential that the reaction occur relatively slowly. For reference, pictures showing examples of this breakage are shown in Figure 5.4.

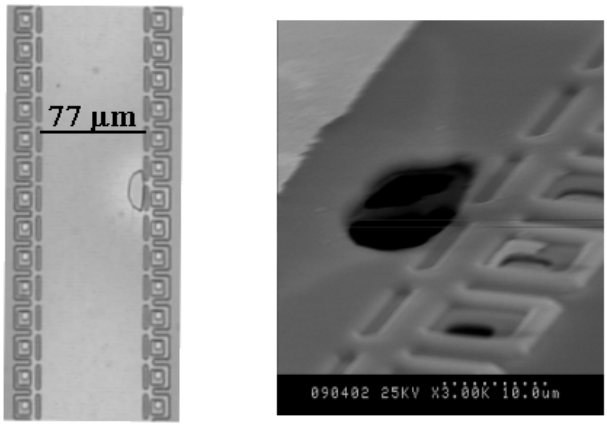

Figure 5.4: (a) Microscope still of membrane breakage; (b) SEM of the same.

The concentration of the potassium hydroxide solution is 22.5%. This value is used because the bottles of KOH purchased from the manufacturer have a concentration of 45%[1]. Since the reaction rate around 20°C is a maximum near 20% KOH (but not so fast as to result in membrane breakage as described above), the available solution is diluted 1:1 with water.

When KOH is used, most device runs that are performed in integrated circuit facilities require that wafers go through a decontamination step before returning to mainline equipment. The most common procedure calls for the second half of the RCA clean procedure, also known as SC-2. This cleaning environment is hostile to membranes with large aspect ratios in that it causes them to break. As a result, an alternative was used in the process run of the devices presented in this dissertation. The key to this alternative is the fact that at this point in the process, the structure on the wafer is comprised entirely of silicon nitride. This is important because according to Aslam [3], the concentration of potassium ions in silicon nitride after an SC-2 clean is $4 \times 10^{11}/\text{cm}^2$, while a rinse in deionized (DI) water results in only a slightly higher concentration of $5 \times 10^{11}/\text{cm}^2$. For reference, a full RCA clean and a piranha

[1] 45% KOH, Mallindrodt Baker, INc., Phillipsburg, NJ08865.

clean reduce the potassium ion concentrations to 1 $\times 10^{11}/\text{cm}^2$ and 2 $\times 10^{11}/\text{cm}^2$, respectively. Both DI-water and piranha solutions were found to be much less hostile to the device's membranes than were those of the SC-2 procedure and were therefore used for the decontamination step.

In order to evacuate and seal the volume underneath the membranes, the wafer is put into the LPCVD nitride furnace one last time. Since the sticking coefficient of silane based chemical vapor deposition systems is between 0.2 and 0.4 [68], the incident silicon nitride atoms will bounce around in the area under the via a few times before finding their final resting place [Figure 5.1g]. It is because of this property of CVD systems that the reduced channel was formed in Figure 5.1c. With the thickness of the channel on the order of one thousand angstroms, it will be sealed relatively quickly. This technique prevents a significant number of silicon nitride atoms from entering the gap and thus changing the dimensions of the cavity. Furthermore, since the reaction occurs in a vacuum, all the air underneath the membrane will have been removed. The thickness of this silicon nitride deposition is generally twice that of the channel, or approximately 2000 Å. If it is undesirable to have this added material on the membrane, it can be removed using a reactive ion etch with the aid of a mask to cover the via holes. This mask is necessary to avoid re-opening the sealed channel[MASK #4].

The final steps in the fabrication of the CMUTs involve a patterned etch on the top surface to create ground pads [MASK #5], and the deposition and patterning of 1500 Å of aluminum (with a 1% concentration of silicon) on the surface to act as the capacitor's top electrode [Figure 5.1h, MASK #6]. Once the fabrication of the transducers is complete, the CMUTs can be characterized to determine their resonant frequency. In order to foster constructive interference, devices with multiple membranes at the transmit and receive ports use this frequency, along with the separation of the membranes, to determine the final substrate thickness of the device.

The thinning procedure, outlined in Figure 5.5 can be performed using a wet etchant such as KOH or tetramethyl ammonium hydroxide (TMAH). The former option capitalizes on the perfect masking ability of silicon nitride in KOH [78] and is therefore ideal for use in this process. To prepare the wafer for the substrate etch,

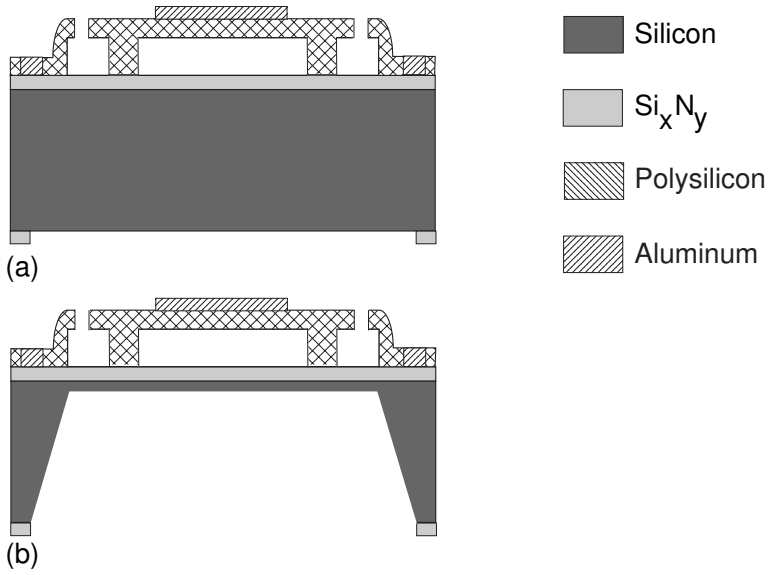

Figure 5.5: Process steps associated with thinning the substrate to complete the Lamb wave device. A single transducer is shown in the picture above.

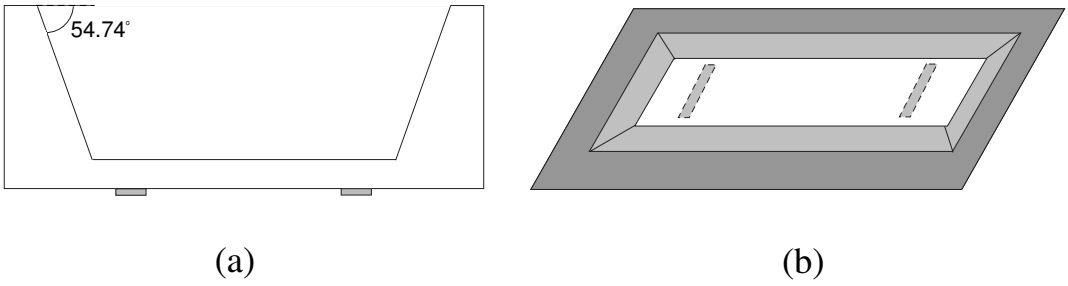

Figure 5.6: (a) 2-D and (b) 3-D representations of the backside of the fabricated device. Note that the wafer is shown upside down and in this particular instance one membrane is used at the transmit and receive ports.

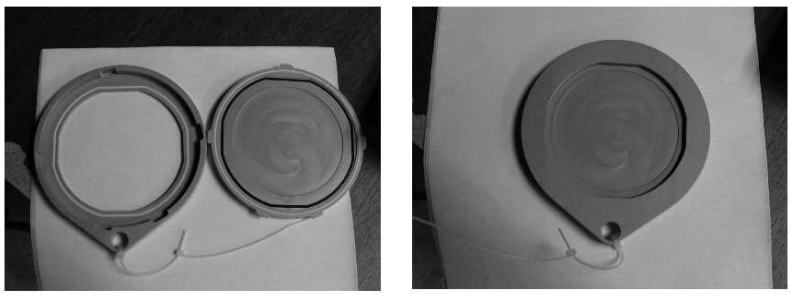

Figure 5.7: Wafer holder used to protect the front side of a 4-inch wafer during etching. (a) The two halves of the holder; (b) The fully assembled holder.

the silicon nitride on the bottom of the wafer is patterned to expose the silicon substrate [Figure 5.5a, MASK #7]. The wafer is then put into a beaker of 22.5% KOH. A drawing of the final shape of the device is shown in Figures 5.5b and 5.6. Note that the etch is anisotropic and that the resulting shape is the familiar pyramidal pit bounded by the (111) planes of the silicon wafer [47].

Due to the high etch rate of aluminum in KOH, the fixture seen in Figure 5.7 was used to shield the device side of the wafer from the etchant. This fixture, similar to others found in the literature [31, 35] is comprised of two halves of PEEK^{TM} that come together over a wafer using a friction o-ring seal. Since most devices incorporated multiple membranes at the transmit and receive ports, the final substrate thickness could not be determined until after the membranes had been built and their resonances had been measured. As a result an etch stop was not incorporated into the wafer. Pictures of the fabricated device are shown in Figure 5.8.

It is worth mentioning that many configurations other than that of the fixture were considered for the described thinning procedure. Since the complications were due to the etching of aluminum in KOH, other options included the use of chrome/gold electrodes instead of Al/Si (1%) or of Apiezon (black) wax as a masking material over the electrodes. The former method did not work because the KOH solution destroyed the adhesion between chrome and silicon in areas where the metal was placed to act as a connection to ground (see Figure 5.9). The latter method failed when high stresses resulting from the applied wax broke the device while it was being thinned in the KOH solution.

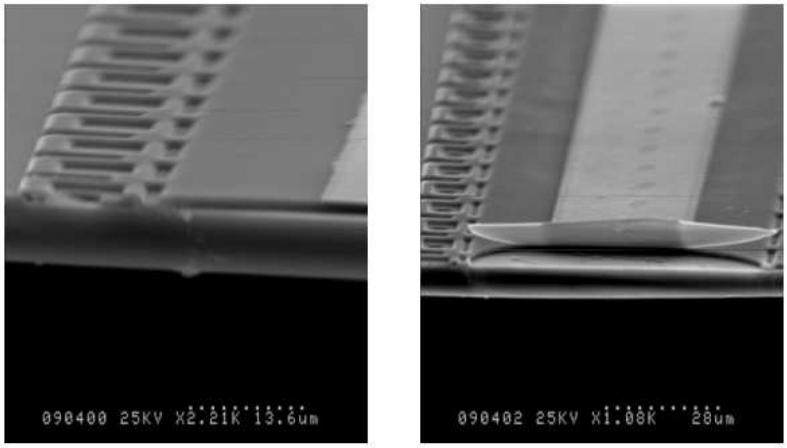

Figure 5.8: SEM stills of the fabricated device using the sacrificial layer method. (a) Left side of the device; (b) Front view of the device with the membrane lifted up to expose the gap area and insulation region.

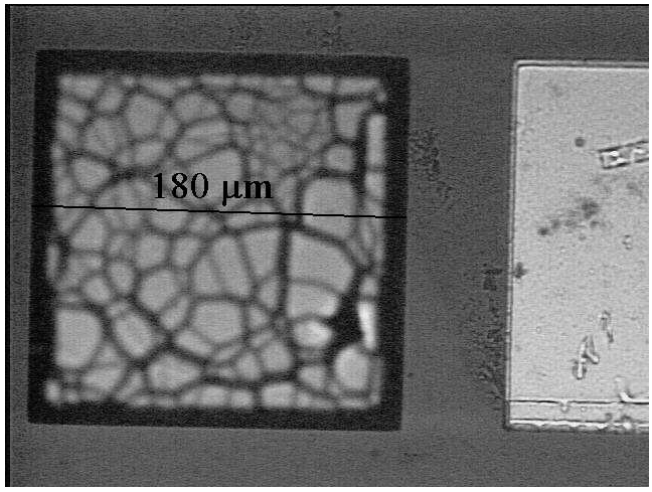

Figure 5.9: The effect of KOH on chrome/gold electrodes. The pad on the left was chrome/gold over silicon while the one on the right is chrome/gold on silicon nitride. The features on the pad on the right are strips of gold that peeled off of other areas of the wafer.

5.2 The Wafer Bonding Method

This process flow uses two wafers. The first is a low resistivity (0.008 Ω-cm) double-side polished 4-inch wafer with a TTV (total thickness variation) specification less than 3 μm and a substrate thickness between 350 and 500 μm. The low resistivity value is necessary as the silicon in this wafer will act as the bottom electrode of the CMUT. In the sacrificial layer method low resistivity was obtained by doping the wafer. In this process doping is highly discouraged as it damages the surface of the wafer and therefore significantly decreases the quality of the subsequent bond. The small TTV value facilitates the finish of the thin plate as it did in the sacrificial layer method. The lower bound of the wafer thickness is determined by the structural integrity of the wafer and its ability to withstand the different processing steps. The upper bound is determined by the etch rate of potassium hydroxide during the final thinning step; as the thickness increases so does the time necessary to perform the etch.

The second wafer is a silicon-on-insulator (SOI) wafer consisting of three layers: a handle silicon wafer that constitutes the bulk of the wafer thickness, a buried oxide layer appropriately called the box, and a thin layer of single crystal silicon referred to as the device layer. For this process the handle wafer should be greater than 350 μm to provide structural integrity, the box needs to be greater than 2000 Å to ensure that it is thick enough to stop a KOH etch from the backside, and the device layer should be on the order of 1 μm as it will act as the CMUT membrane.

The processing steps of the wafer bonding method of device fabrication are shown in Figure 5.10 and listed in Appendix B. The first step is to thermally grow silicon dioxide on the top side of the wafer [Figure 5.10a]. This layer protects the underlying silicon during a subsequent reactive-ion etch (RIE) that will define the active area of the device. This is important because it is this surface that will bond to the SOI wafer and it should not be exposed to polymers that are by-products of the RIE etch. Using the first mask in the process, the oxide is patterned and etched along with

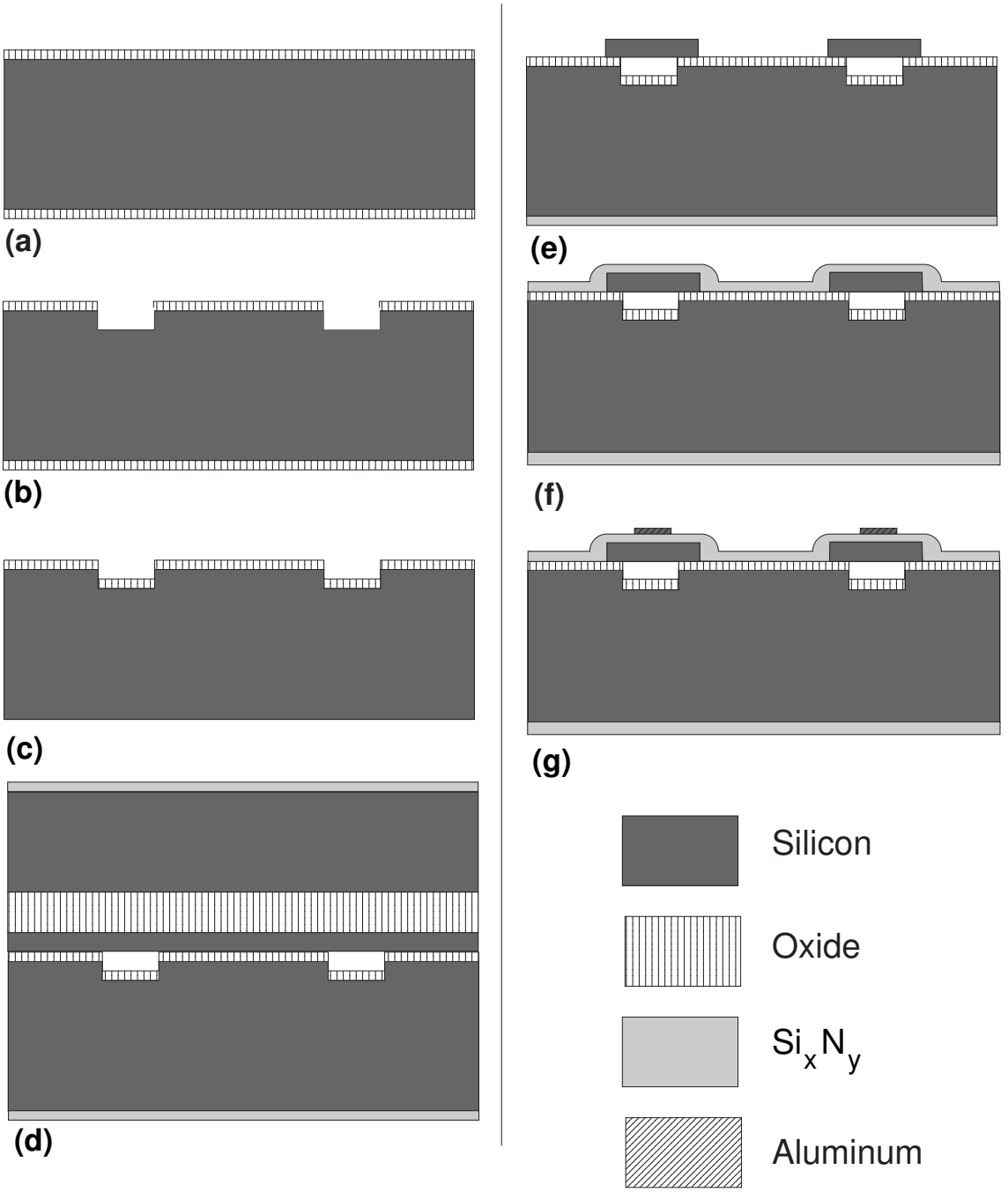

Figure 5.10: Process steps of the capacitive micromachined ultrasonic transducer manufacturing process using the wafer bonding method. Two transducers are shown in the picture above.

	Temperature (°C)				
% KOH	20°	40°	60°	80°	100°
10	0.4	3.5	23	123	551
20	0.88	7.5	50	268	1200
30	1.42	12.2	81	435	1950
40	1.33	11.4	76	406	1820
50	1.08	9.3	62	330	1480
60	0.81	6.9	46	246	1100

Table 5.2: Etch rates of thermally grown silicon dioxide in (nm/hr) for various KOH concentrations and temperatures, after [78].

1 μm of the underlying silicon substrate in an RIE system [Figure 5.10b, MASK #1]. Since the remaining oxide on the surface of the wafer has been exposed to polymers, it is removed using an oxygen plasma and, for good measure, through dry oxidation. The oxide on the surface of the wafer is then removed by an HF dip and is then reintroduced everywhere, including in the newly formed trenches [Figure 5.10c]. The oxide in this trench will act as the device insulation layer while the oxide on the surface will be used for fusion bonding with the device layer of the SOI wafer.

Wafer bonding is performed by a vendor outside of SNF [Figure 5.10d]. Once it is received, 2000 Å of silicon nitride is deposited on both sides of the wafer. This nitride will act as a mask for the wafer thinning step just as it did in the sacrificial layer method. It is introduced here because it acts to protect the backside of the wafer while the handle and box of the SOI are removed through a three step process. First, wafer grinding is performed where all but approximately 50 μm of silicon is removed. Second, the remaining silicon is etched away in a solution of 22.5% KOH at 80°C. The point at which all of the silicon is removed can be determined by inspection as the hydrogen bubbles that is are a by-product of the reaction disappear (see (5.3)). The box has a thickness of a few thousand angstroms and acts as an etch stop, protecting the device layer of the SOI wafer. Etch rates for silicon dioxide in KOH are presented in Table 5.2. Finally, the box is removed with an HF dip.

Once the device layer of the SOI wafer is exposed, the wafer is annealed at 1100°C for two hours to solidify the fusion bond. The top layer of single crystal

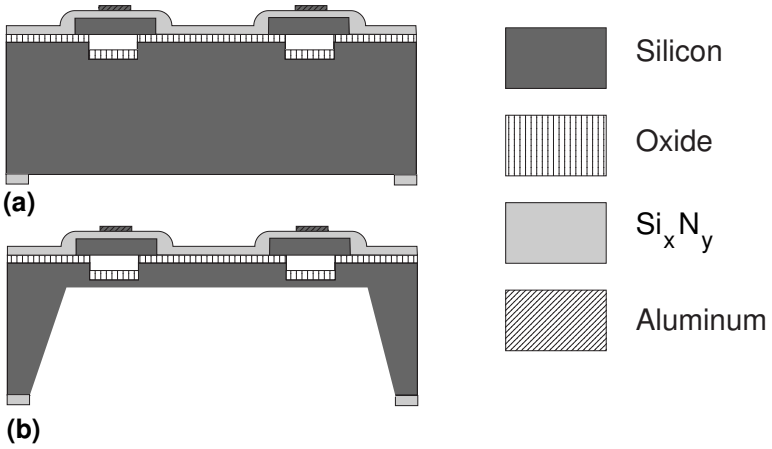

Figure 5.11: Process steps associated with thinning the substrate to complete the Lamb wave device. Two transducers are shown in the picture above.

silicon is then patterned to define the membrane [Figure 5.10e, MASK #2]. For a conventional CMUT process, the next step would be the deposition of metal which would act as the top electrode of the capacitor. In preparation for the upcoming substrate etch, however, a 550 Å layer of LPCVD silicon nitride is deposited on both sides of the wafer [Figure 5.10f]. The purpose of this layer is to protect the top side of the device during the etch. Because of the large thickness of the wafers used in this process, the wafer holder shown in Figure 5.7 cannot be used. The nitride layer is made as thin as possible so as to not significantly affect the behavior of the membrane. After the LPCVD deposition, the metal is sputtered and patterned in the form of 1500 Å of aluminum (with a 1% concentration of silicon) [Figure 5.10g, MASK #3]. The fabrication of the CMUT using the wafer bonding method is now complete.

Note that ground pads are not shown in Figure 5.10g. This is because they have purposely been left out of the design since the thinning procedure described below does not allow for them. Instead of through pads, ground connections are made to the sides of the device after it has been separated from the wafer. This is best done using conductive epoxy to electrically connect ground on the device to ground on the PCB upon which the device is housed.

The process steps relating to the thinning of the device are shown in Figure 5.11.

Again, due to the larger thickness of the wafers used in this process, the wafer holder of Figure 5.7 could not be used. Therefore, an alternate method had to be found to etch the silicon on the backside of the wafer yet protect the metal on the front side. The key to this method is a solution of tetramethyl ammonium hydroxide (TMAH) doped with silicon and ammonium persulfate (APS) $[(NH_4)_2 S_2O_8]$, also referred to ammonium peroxidisulfate. According to Yan et al. [104], this solution will allow for the etching of silicon, low surface roughness, and high selectivity to oxide (1285) and silicon nitride (2000) without attacking exposed aluminum. The optimal mix of the three chemicals is 5 wt% TMAH, 1.6 wt% silicon, and 0.5 wt% APS. The specific mix used in this research was 200 mL TMAH[2], 16 g silicon[3], 5 g APS[4], and 779 mL water at 90°C. To prepare the wafer for the etch, a window is formed in the silicon nitride to expose the substrate [5.11a, MASK #4]. Next, silicon is dissolved in TMAH at around 60°C in order to minimize the bubbles that result from the reaction. The temperature is then raised to 90°C and the APS and wafer to be etched are added. For reasons that are currently unknown, the reaction takes approximately two hours to get started. Once it does, however, the etch proceeds at around 1 μm/min and follows the (111) plane as shown in Figure 5.6. The pictures in Figure 5.12 show stills of the final device.

5.3 Method Comparison

The wafer bonding method of CMUT fabrication has three major advantages over its sacrificial layer counterpart. The first has to do with device fabrication time. The bonding method incorporates significantly fewer processing steps and three less masks which translates to faster device turnaround. Furthermore, because the cavity is formed by bonding an SOI wafer on top of a pre-etched trench, the wait associated with the sacrificial etch is avoided. This is important because for some geometries

[2]25% TMAH, Mallinkrodt Baker, Inc., Phillipsburg, NJ 08865

[3]200 mesh powder, Spectrum Chemical Mfg. Corp., Gardena, CA 90248 • New Brunswick, NJ 08901

[4]Mallinkrodt Baker, Inc., Paris, KY 40361

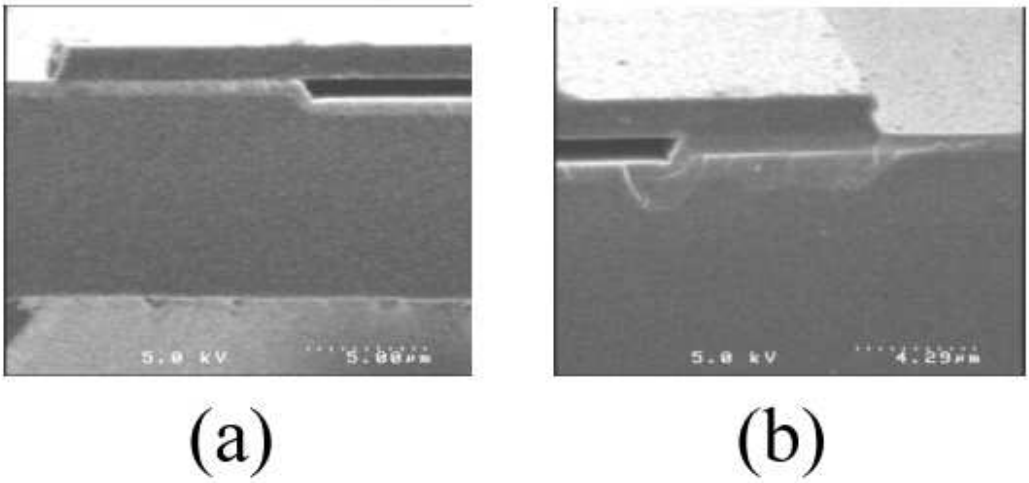

Figure 5.12: SEM stills of the (a) left side and (b) right side of the fabricated device using the wafer bonding method.

this etch can take up to five days to complete.

The second advantage relates to membrane yield. The membrane material in the devices built using the sacrificial layer method is low stress silicon nitride. The low stress recipe involves a DCS:NH_3 ratio of 14:1 which produces an amorphous film with 100 MPa of residual stress but poor mechanical properties. These membranes cannot support the high aspect ratio required for Lamb wave devices and generally break during the fabrication process. The average yield with regards to membrane breakage for the various runs performed in the course of this research was 50%. With the wafer bonding method, the membrane is composed of single crystal silicon which has few internal defects, low internal mechanical loss, as well as very low internal stress. This technology vastly improves the structural rigidity of the membranes and increases the yield with regards to membrane breakage to 100%.

The third advantage of the wafer bonding method lies in uniformity. The geometry of the resulting device is determined by reactive ion etching, oxidation of silicon, and the (100) silicon device layer of an SOI wafer. The mechanics of silicon and these three processes are very well understood, and therefore the geometry of the device can carefully controlled. In contrast, the dimensions of devices built using the sacrificial

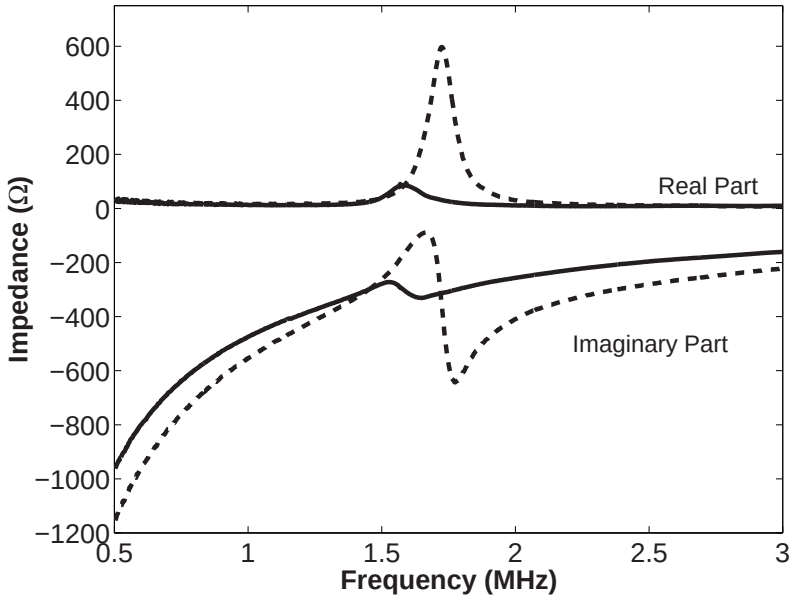

Figure 5.13: Sacrificial layer method: real and imaginary parts of the input impedance of two membranes (solid and dashed) that make up a single device.

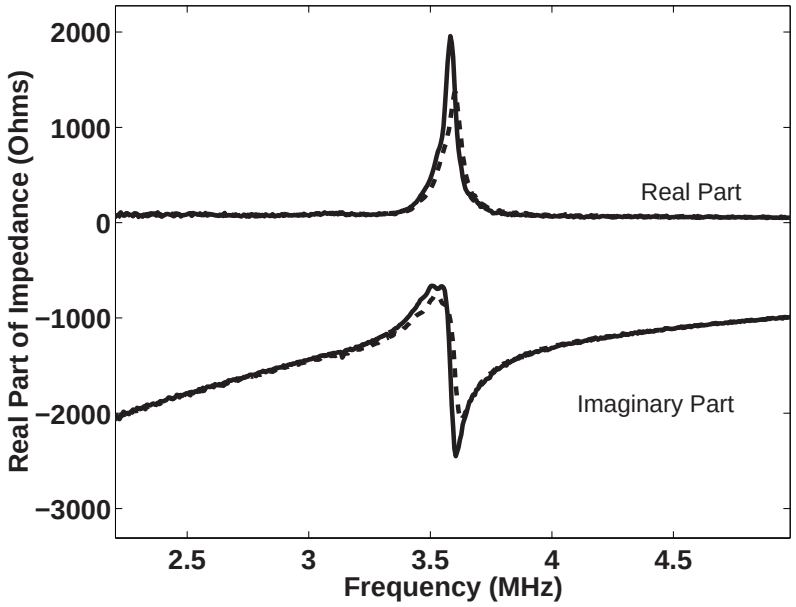

Figure 5.14: Wafer bonding method: real and imaginary parts of the input impedance of two membranes (solid and dashed) that make up a single device.

layer method rely heavily on deposited LPCVD silicon nitride and are at the mercy of its ever-changing film chemistry, material properties, and low stiction coefficient. With tight process control comes device-to-device and wafer-to-wafer uniformity as well as the ability to model and therefore predict device behaviour. Evidence of the effect of the processing method on uniformity is shown in Figures 5.13 and 5.14. The two graphs show representative input impedance curves of two different membranes that make up a single device as measured by an HP8751 vector network analyzer. Note that the data from the wafer bonded membranes suggest much higher repeatability that does the data from membranes built using the older method. More results, along with comparisons to the theoretical models of Chapter 4, are presented in the next chapter.

Chapter 6

Device Characterization

Using the insight obtained from the models described in Chapter 4 and the manufacturing techniques presented in Chapter 5, Capacitive Mircomachined Ultrasonic Lamb Wave Transducers have successfully been built and characterized. The purpose of this chapter is to present the results of this characterization.

The first step in this effort is to use experimental results to confirm the electromechanical model of the Lamb wave device. This is done through an analysis of both input impedance and laser-doppler-vibrometer (LDV) data. After completing this task, the chapter continues by presenting further LDV data in conjunction with the device impulse response to show that the fabricated CMUTs do indeed propagate acoustic energy, and that this energy is in the form of a Lamb wave. This is followed by an analysis of the factors that determine the device efficiency and an analysis of the insertion loss data that quantifies this efficiency. The chapter concludes by touching on some applications of the Lamb wave device.

6.1 Confirmation of the Electromechanical Model

Recall that the input impedance graph in Figures 4.21 represents the behaviour of a Lamb wave device built using CMUTs as described by the equivalent circuit model of Figure 4.12. Over most of the frequency span, the imaginary part of the graph follows the impedance of a capacitor with a value equivalent to the combination of

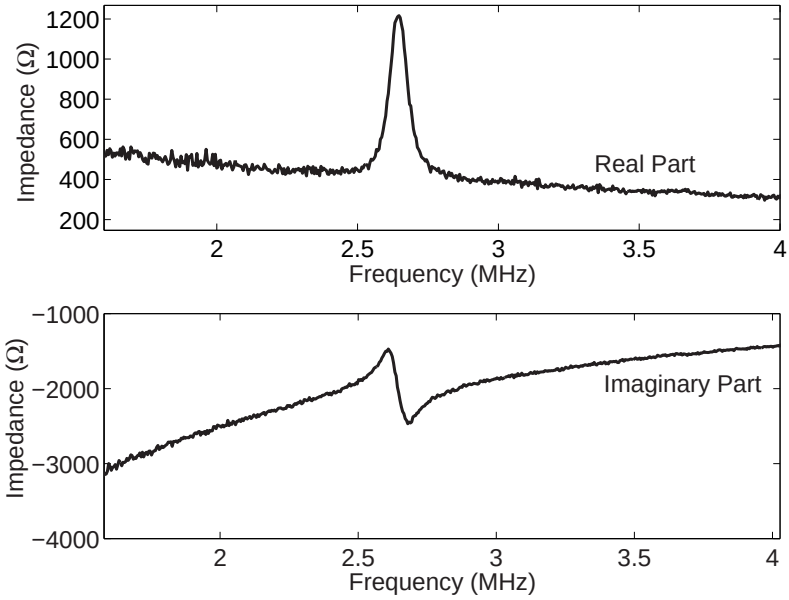

Figure 6.1: Input impedance of a Lamb wave device on a 500 μm substrate with a membrane width of 60 μm, membrane thickness of 1.34 μm, and an air gap of 0.97 μm at a bias of 100 V.

C_0 and a fraction of the reactance on the mechanical side. In the middle, however, the graph exhibits acoustic behaviour in the form of two resonances (open and short circuit). Likewise, the real part of the graph is zero except in the middle where it exhibits acoustic behaviour in the form of a single resonance. The plots in Figure 6.1 show experimental input impedance measurements, as measured by an HP8751A vector network analyzer, for a device with dimensions similar to what was used in the simulations. Both the imaginary and real parts of the plots exhibit acoustic behavior in the manner predicted by theory, confirming the validity of the equivalent circuit model. Note, however, that while the shape of the imaginary part follows that which is predicted by theory, the short circuit resonance does not exist as the impedance no longer crosses the x-axis. This is because parasitics associated with the traces on the device (modeled as C_p in the equivalent circuit) have decreased the overall reactance. Parasitics affect the real part of the data as well, where the baseline resistance varies from 400 Ω to approximately 550 Ω over the frequency span of the graph.

While most of the elements in the equivalent circuit model play a relevant role

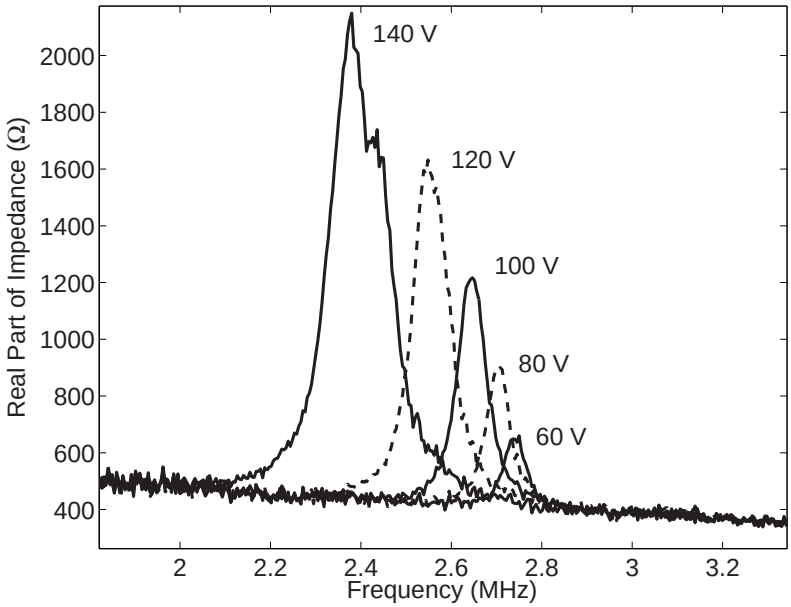

Figure 6.2: Real part of the input impedance of a Lamb wave device on a 500 μm substrate with a membrane width of 60 μm at various bias voltages. The collapse voltage is 150 V.

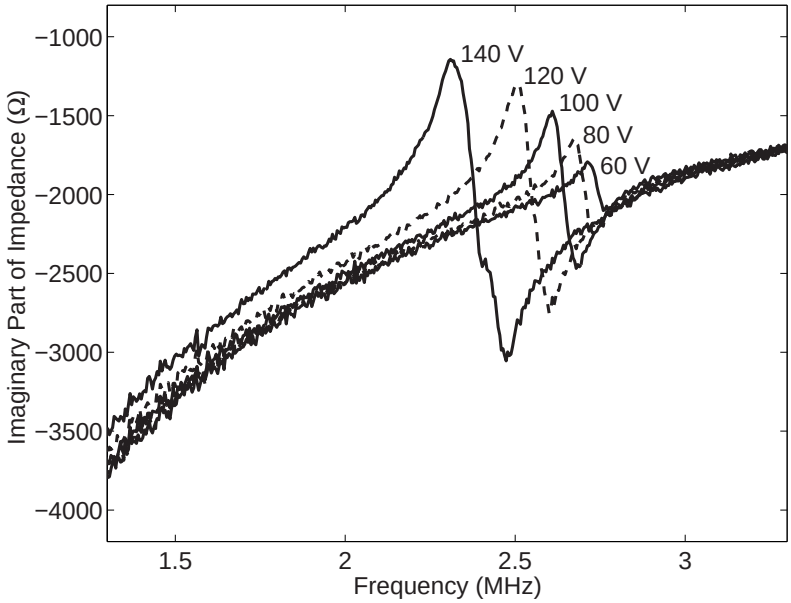

Figure 6.3: Imaginary part of the input impedance of a Lamb wave device on a 500 μm substrate with a membrane width of 60 μm at various bias voltages. The collapse voltage is 150 V.

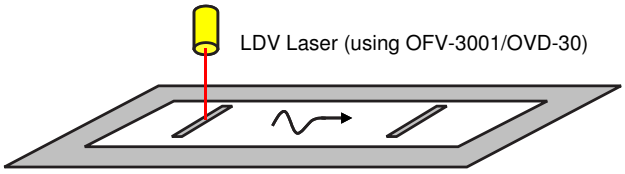

Figure 6.4: Experimental setup of the LDV system. The LDV system comprises of the Poltytec-PI OFV-3001 decoder in conjunction with an OVD-30 sensor head.

in the input impedance graphs described above, the spring softening capacitor does not. Section 3.1.1 describes how the spring softening capacitor decreases the resonant frequency of the device as the applied bias voltage increases. Thus, further confirmation of the equivalent circuit model comes from analyzing the spring softening phenomenon of the device; experimental verification is shown in Figures 6.2 and 6.3.

A fundamental property of any electromechanical transducer is that it converts electrical energy into mechanical energy. In the case of a CMUT, the latter energy is in the form of membrane displacement. In an effort to investigate this transfer of energy, the mechanical response of a CMUT membrane to an input electrical pulse was measured optically by a laser doppler vibrometer (LDV) system using the setup illustrated in Figure 6.4. The data is shown in Figure 6.5 where the output data is superimposed on the input pulse. As expected, the membrane does not begin to vibrate until right after the electrical pulse is applied to the membrane. Furthermore, note that the response decays and then picks up again at around 8 μs. This increase is due to reflections along the substrate of a Lamb wave that was excited by the vibrating membrane. An analysis of these reflections is presented in Section 6.3.1.

The Fourier transform of the optically measured displacement curve yields the response of the CMUT membrane. A theoretical calculation of this response, shown in Figure 4.22, predicts a smooth resonant curve with the peak at the short circuit resonant frequency. The experimental result paints a very different picture. Figure 6.6a shows the response to a 2 V input pulse of a different membrane than was used in the experiment for Figure 6.5 over a longer time span. The normalized shape of the Fourier transform of the response, shown in Figure 6.6b, has the same general trend as the theoretical calculation, but is much more jagged. This abnormality is due to

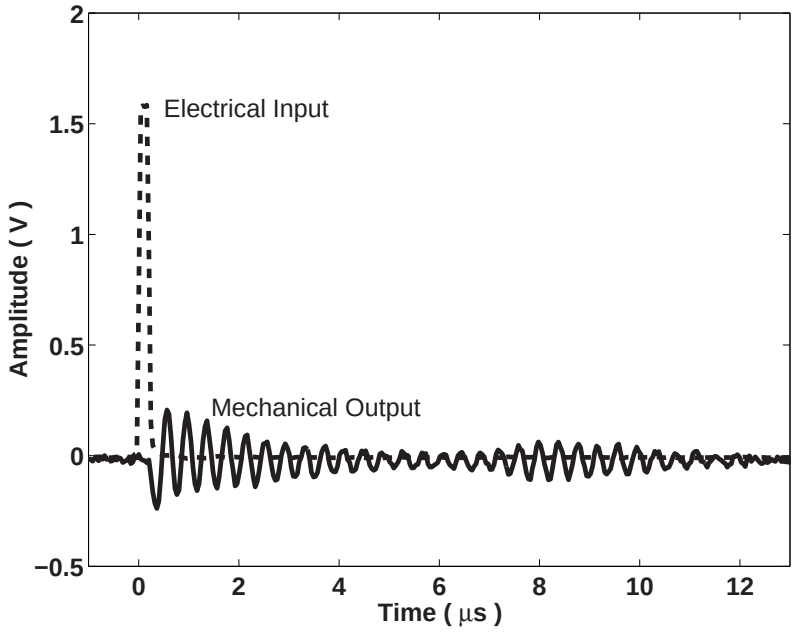

Figure 6.5: Input pulse (applied electrically) and membrane displacement (measured optically) on a CMUT that is on an 8 μm substrate with a membrane that is 60 μm wide. The voltage to displacement conversion factor is 50 nm/V.

reflections of the Lamb wave off different geometries of the device that interfere with the natural vibrations of the membrane.

In order to show that the jagged features of the transform data are not mathematical artifacts, the membrane response was measured using a second technique: rather than mathematically calculating the frequency content of the membrane vibration, the content was measured directly. This was done by sweeping the membrane with a CW source over a range of frequencies and measuring the value of the maximum membrane displacement at each point. The resulting normalized amplitudes are plotted in Figure 6.6c and superimposed on the calculated results in Figure 6.6d. Note that while the transform data has a higher noise content, the shapes of the two curves match very well.

An interesting feature of the LDV data is in the pulse response in Figure 6.6a: the curve appears to be amplitude modulated by a signal that is approximately 30 kHz. It turns out that this is the natural frequency of the thin (8 μm) plate upon which

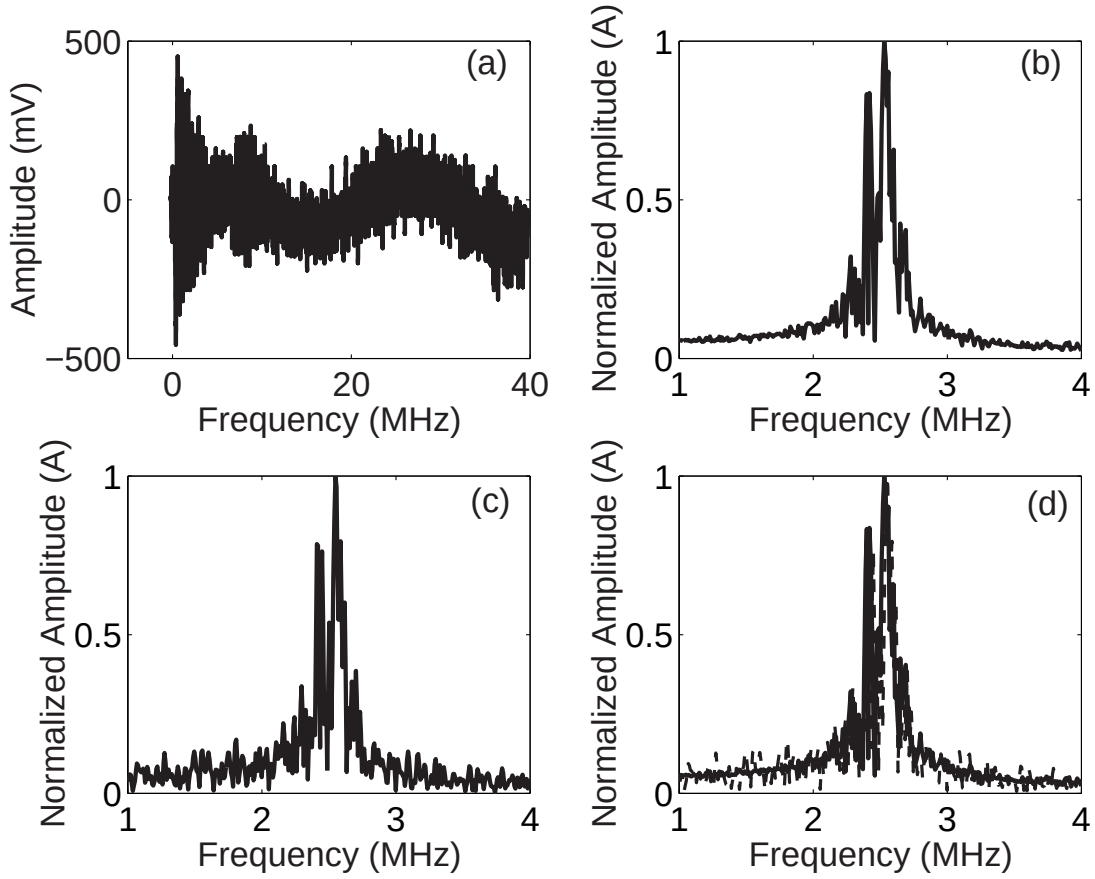

Figure 6.6: (a) Step response measured optically using an LDV system. Voltage and displacement conversion factor is 50 nm/V; (b) Fourier transform of step response; (c) Membrane response measured using a CW source as described in the text; (d) Results of (b) and (c) superimposed on each other.

the CMUT membranes are resting (see Figure 6.7); data in Figure 6.8 confirms this assertion. The step response when the LDV is focused on the plate is shown in Figure 6.8a, while the response over the thicker (500 μm) region is shown in Figure 6.8b. Note that the frequency of the data in the thin region is approximately 30 kHz while the data in the thicker region is much higher.

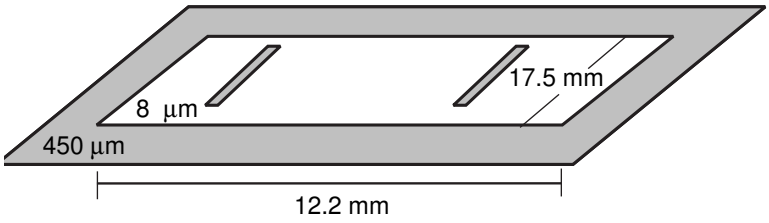

Figure 6.7: Dimensions of the device described by the data in Figure 6.8.

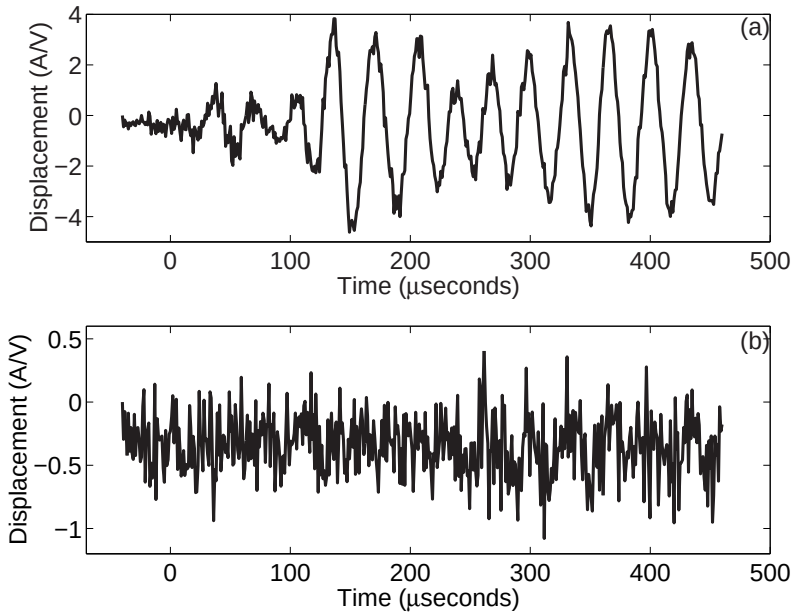

Figure 6.8: (a) Displacement of the thinner region of the device pictured in Figure 6.7; (b) Displacement of the thicker region of the device.

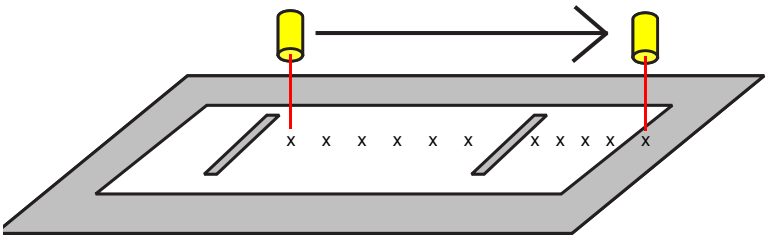

Figure 6.9: Locations along the device substrate where data is taken to create the graph shown in Figure 6.10.

6.2 Confirmation of Lamb Wave Transduction

The next step in the presentation of experimental data is to confirm that the CMUTs propagate acoustic energy in the form of a Lamb wave. This is done through a two step process. The first verifies that waves are indeed launched from the CMUT along the substrate using LDV techniques similar to the ones described in the previous section. The second step is to confirm the flexural[1] nature of these waves by comparing their properties to the well understood behavior of Lamb waves.

6.2.1 Acoustic Wave Propagation

The acoustic energy launched from a vibrating CMUT along the substrate can be monitored by focusing the laser of the LDV system at points along the substrate. Using the setup shown in Figure 6.9, the membrane displacement in response to a 16 V, 0.2 μs pulse was measured at each location marked with an "x." The results are shown in Figure 6.10. Note that since each point is progressively farther away from the transmitting membrane, it takes the wave longer to appear at the measurement location. This is evidence that the wave is propagating from left to right, away from the transmitting membrane.

Various characteristics of this data provide additional insight into the behavior of the Lamb wave device. First, note that the amplitude of each curve is approximately

[1] As predicted in Section 4.5.3 and confirmed in Section 6.2.2, the dilational component of the wave is much smaller than the flexural one and therefore does not manifest itself in the experimental data.

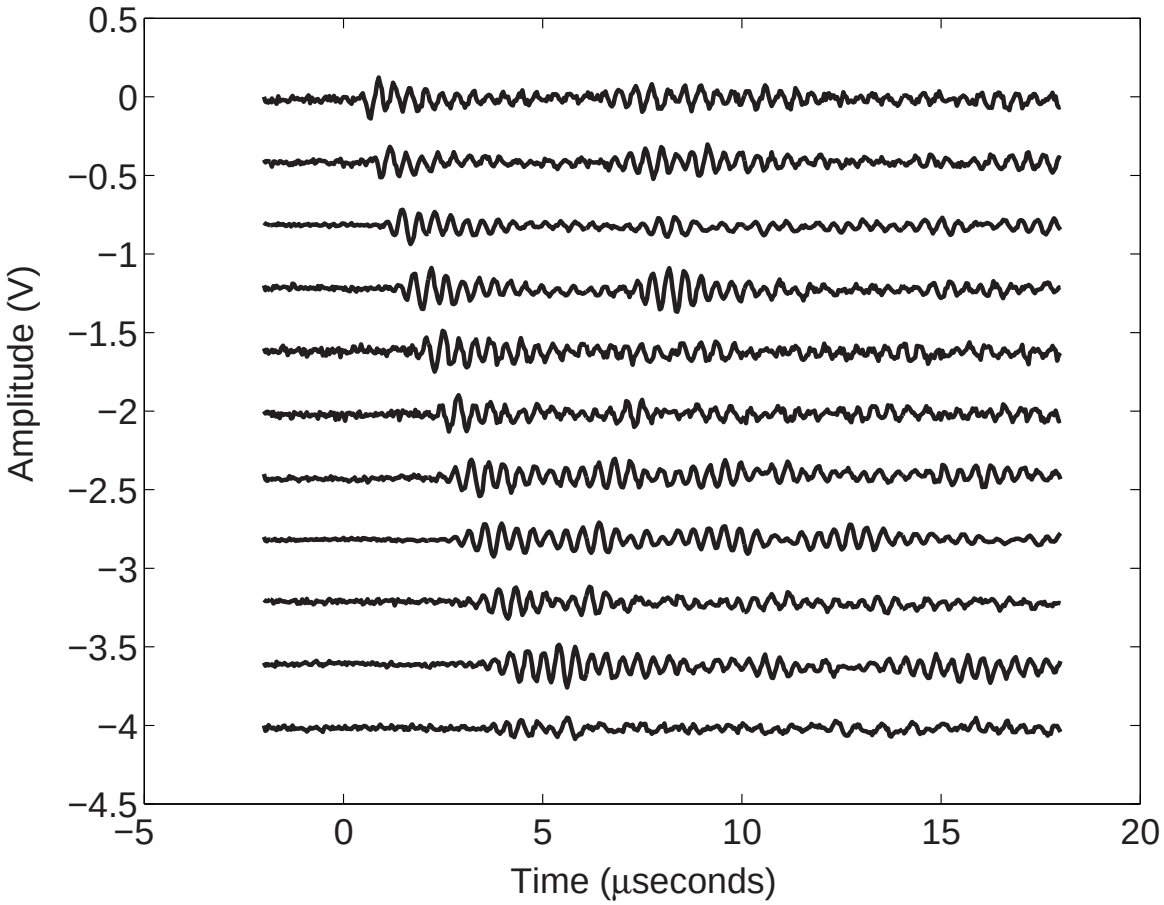

Figure 6.10: Data obtained at each point marked in Figure 6.10. The top curve is obtained at the point closest to the transmitting membrane. The voltage to displacement conversion factor is 50 nm/V.

the same (except for the last one), indicating that the wave does not decay as it propagates along the substrate. This shows that very little acoustic energy is lost into the environment. Second, the amplitude of the last curve is smaller than all the others because its location is on the thick part of the device. This behavior is expected since for a given amount of energy, a more massive material will have a smaller displacement than a lighter one. The decrease is exacerbated by the reflections of the incoming wave at the thin/thick interface of the substrate, prohibiting a significant part of the energy from even getting to the thicker substrate. Third, each data set shows evidence of reflections at the thin/thick interface. For example, the data at the top

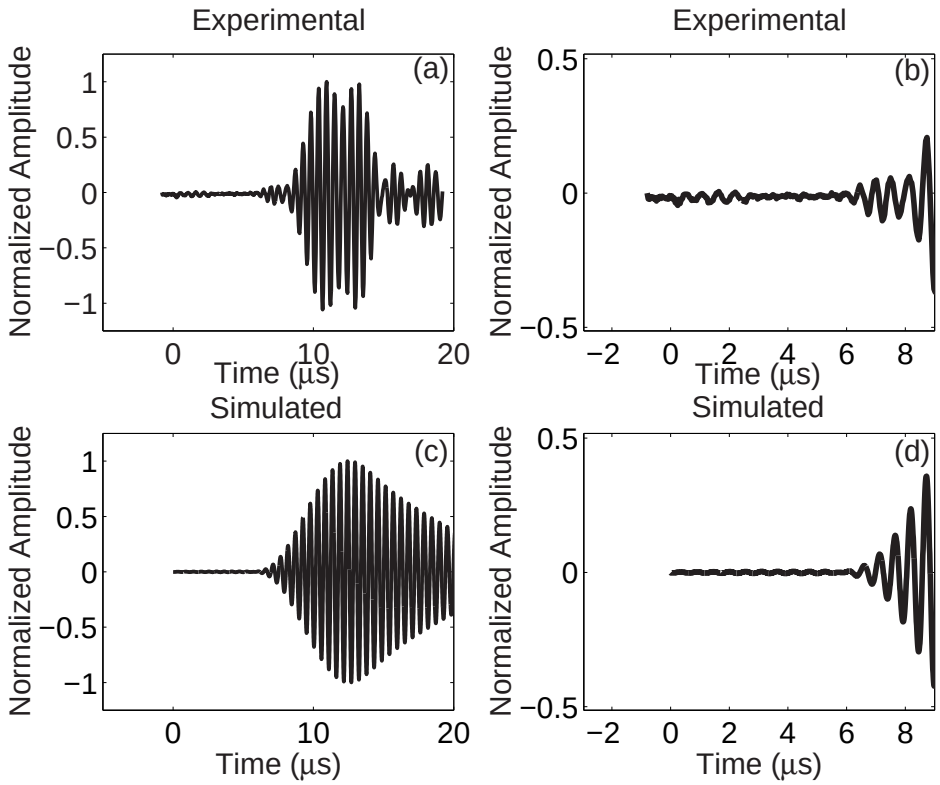

Figure 6.11: (a) Experimental data of the received signal; (b) Zoom in of the received pulse (experimental); (c) Simulated data of the received signal; (d) Zoom in of the received pulse (simulated).

has the initial wave arriving at 0 μs and the reflected wave appearing near 7 μs. As the location where the data is collected progresses to the right, the incident wave takes longer to arrive and the reflected wave shows up more quickly. The second last data set, taken just to the left of the reflecting boundary, shows both waves arriving so close together that it is not possible to discern one from the other.

6.2.2 Comparing Acoustic Behavior to Lamb Waves

Having verified that the CMUTs are launching acoustic waves along the substrate, the next step is to confirm that the energy is in the form of a Lamb wave. This is done by comparing well understood properties of Lamb waves to data obtained from

the fabricated devices.

First, recall from Section 3.2 that Lamb waves are surface waves that have significant particle displacement in the direction of the plane normal to the substrate. The acoustic waves launched from the CMUTs match this description, as LDV results presented in the previous section recorded data from the displacement of the plate in this same direction. Thus, from the perspective of particle mechanics, the wave motion has a characteristic that resembles that of a Lamb wave.

The more compelling argument that the acoustic energy constitutes a Lamb wave lies in the dispersion relation. The graphs in Figure 3.13 show the velocity of the Lamb wave as a function of the frequency-thickness product. These curves can be used to predict the arrival time of a Lamb wave if the distance between the transmitting and receiving membranes is known. The graphs in Figure 6.11 show simulated and experimental results of a Lamb wave propagating along a 18 μm substrate where the transmit and receive ports are 7.8 mm apart (measured from the two closest membranes on each side) and consist of 15 membranes fabricated using the sacrificial layer method and separated by 410 μm. Figures 6.11b and d zoom in on the graphs of Figures 6.11a and c, respectively. The ripples near t = 0 in the experimental data is feedthrough from the input tone bursts. The simulation was performed by obtaining the Fourier components of an input tone burst and propagating them the appropriate distance, using the dispersion relation of the zeroth order antisymmetric (A_0) mode to determine the velocity at each frequency. The agreement of the simulated arrival times is within 2% of what was experimentally measured. This verifies that the propagating wave is indeed a Lamb wave and that most of the propagating mode energy is in A_0 mode.

6.3 Analyzing and Optimizing Device Efficiency

While there are many factors that play a role in optimizing the capacitive micromachined ultrasonic Lamb wave transducer, three stand out as the most significant. These are the electrical matching networks, the thinning of the device substrate, and the use of a single membrane at the transmit and receive ports of the device. In the

sections that follow, the way in which each of these factors affects device efficiency is discussed and the means through which they have been optimized are presented.

6.3.1 Substrate Thinning

Data in Figure 4.26, in conjunction with the discussion in Section 4.5.5, illustrate the expected correlation between substrate thickness and device efficiency. Specifically, the simulations suggest that for smaller substrate thicknesses, the value of $R_{substrate}$, and thus the energy transferred into the Lamb wave, increases. Experimental results are consistent with this prediction. Figures 6.12 and 6.13 show both parts of the input impedance of a Lamb wave device as its substrate is thinned from its original thickness of 350 μm to its final value of 18 μm. The data was obtained from 15 CMUT membranes 77 μm wide, built using the sacrificial layer method and wired in parallel. The wafer was pulled out of the KOH beaker during various points of the etch process and measured using the HP8751A vector network analyzer. The primary feature to note in these graphs is that the quality factor (Q) of the device decreases as the substrate is thinned. This is an indication that there is an increased source of loss in the system; this loss is energy coupled from the vibrating membrane into the substrate in the form of a Lamb wave.

Further evidence that the coupling efficiency has improved with a thinner substrate lies in a comparison of the input impedance graphs shown in Figure 6.14. This data is taken from devices built using the wafer bonding method. They have a single membrane at each port with a width of 50 μm and a substrate of 8 μm. Note that the devices built on a thicker substrate have impedance curves much smoother than their thinner counterparts. As the efficiency of the device increases, so does the energy coupled into the substrate. Thus, the effect of wave reflections become more significant. It is these reflections that create the ripples in the impedance graphs of Figures 6.14c and d.

To help make the case that acoustic wave reflections along the substrate create ripples in the input impedance curves of a CMUT, a dedicated experiment was performed. Using a device similar to the one shown in Figure 6.7, the substrate on

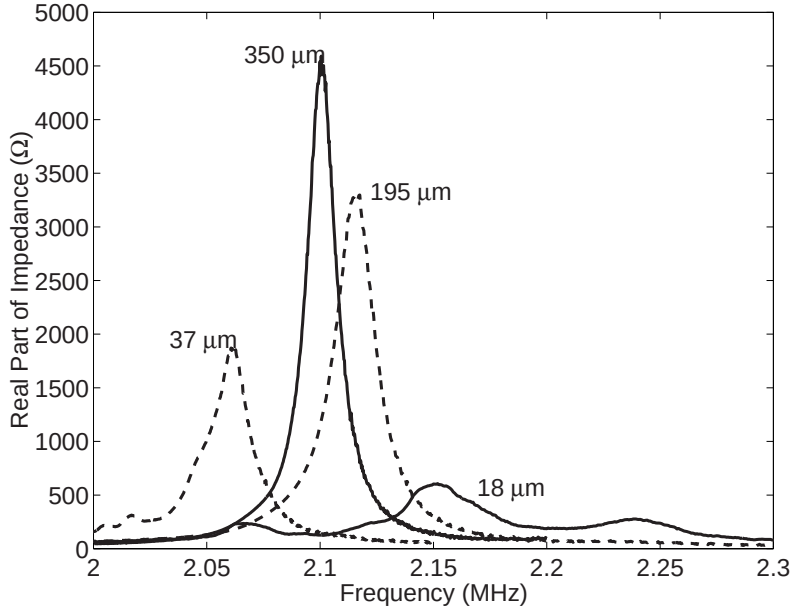

Figure 6.12: Real part of the input impedance for a single device as it is thinned from 350 μm to 18 μm.

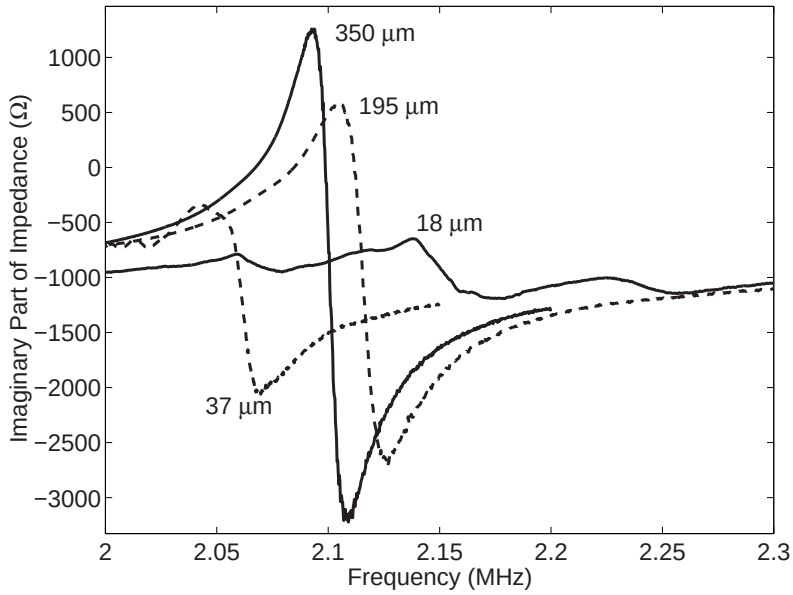

Figure 6.13: Real part of the input impedance for a single device as it is thinned from 350 μm to 18 μm.

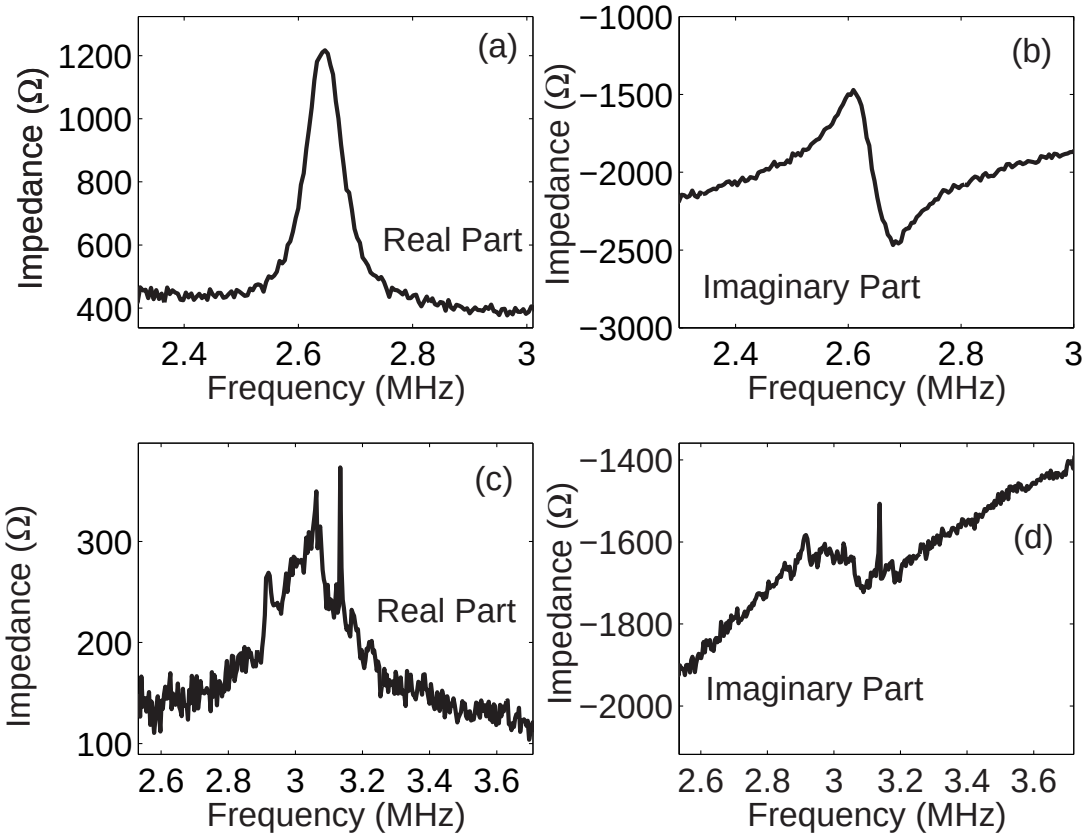

Figure 6.14: (a) Real and (b) imaginary parts of the input impedance of a device on a 450 μm substrate; (c) Real and (d) imaginary parts of the input impedance of a device on an 8 μm substrate.

either side of the transmitting CMUT was covered with epoxy in an effort to absorb the emitted acoustic energy. The input impedance of the transducer was measured with and without the sealant and, as illustrated in Figure 6.15, the curve relating to the structure with mitigated reflections is significantly smoother. Unfortunately, this technique can not be used in practice as most devices are too small for the epoxy to have an effect.

6.3.2 Matching Networks

When a Lamb wave device is wired in an oscillator configuration for use as a sensor, the amplifier that is used generally has input and output impedances of 50 Ω. A

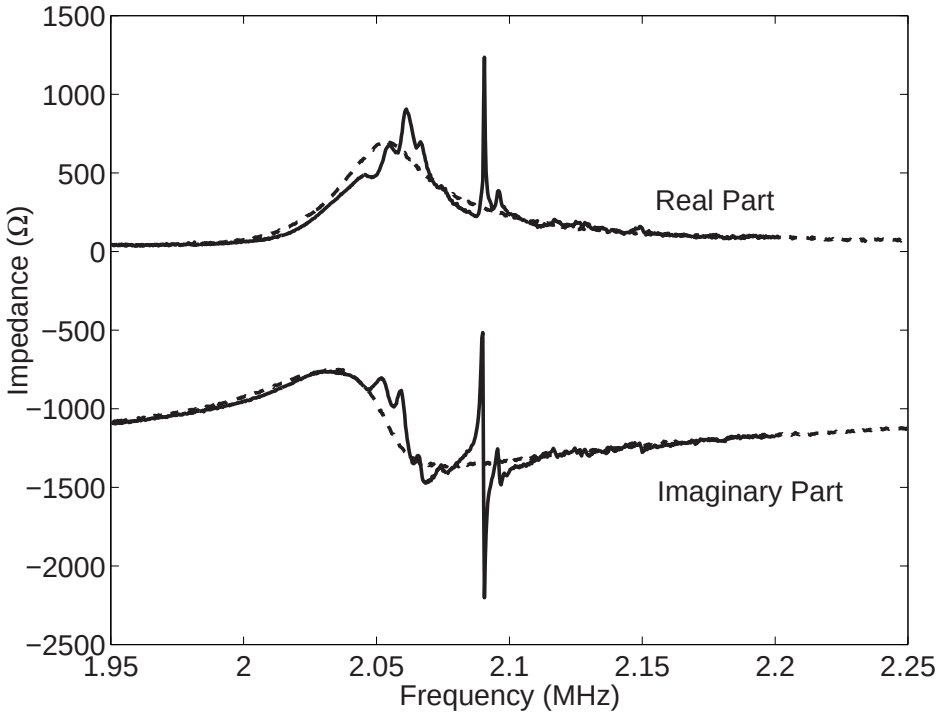

Figure 6.15: Real part of the input impedance with (dashed) and without (solid) epoxy to absorb the reflections.

CMUT that is operating near its collapse voltage will have a significant mismatch with this amplifier as it is a relatively high impedance device. The solution to this problem is to introduce an L-match network tuned to the resonant frequency of the CMUT. This network effectively optimized the conversion of energy from the electrical domain into the mechanical one.

The graphs in Figures 6.17 and 6.18 show the input impedance of the transmit and receive ports of a Lamb wave device built using CMUTs before and after matching. The L-match used is shown in Figure 6.16. The CMUTs were built using the wafer bonding method, are 60 μm wide and 1 cm long, and are on a substrate 8 μm thick. The goal of the network is to minimize the energy loss as it is transferred to the device; the network comes close, yielding the power loss characteristic shown in Figure 6.19. This curve was generated by manipulating the experimentally obtained reflection coefficient Γ using (6.1) - (6.2) [39]. The bandwidth of the match, using the 3 dB

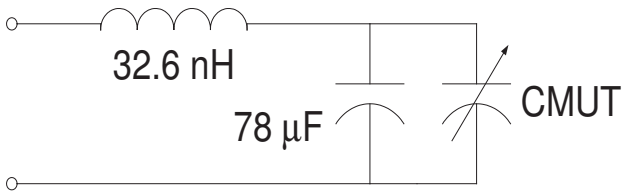

Figure 6.16: L-match used for the input impedance graphs shown in Figure 6.18

criterion, is 450 KHz.

$$\rho = |\Gamma| \tag{6.1}$$

$$P_{loss} = 20 \log_{10} \left(1 - \rho^2\right) \tag{6.2}$$

6.3.3 Using a Single Membrane

The initial design of this device was based on the topology of a conventional piezoelectric interdigital transducer (IDT). In an IDT, multiple transducers separated by one wavelength are used to excite and receive Lamb waves at the two ports. This configuration is necessary as each IDT is broadband and the frequency response of the device is determined by the number of fingers that are used and the spacing between them. Acoustic wave devices built using CMUTs do not need multiple fingers for this purpose since the transducer membrane has its own narrowband frequency response. Lamb wave devices built using CMUT technology can therefore take advantage of this property and use a single membrane at both ports. This configuration is desirable because it mitigates acoustic wave reflections between membranes. These reflections are conceptually the same as those described in relation to Figures 6.14 and 6.15. The interference created by these reflections is difficult to predict and creates significant variation of the device insertion loss along the passband.

Using a single membrane has the added advantage of precluding the device from incurring a frequency mismatch problem. This mismatch occurs when the frequency of maximum membrane displacement is different from the frequency of minimum destructive interference (equivalently, the frequency of maximum constructive interference) as determined by the spacing between CMUT membranes. The root of this

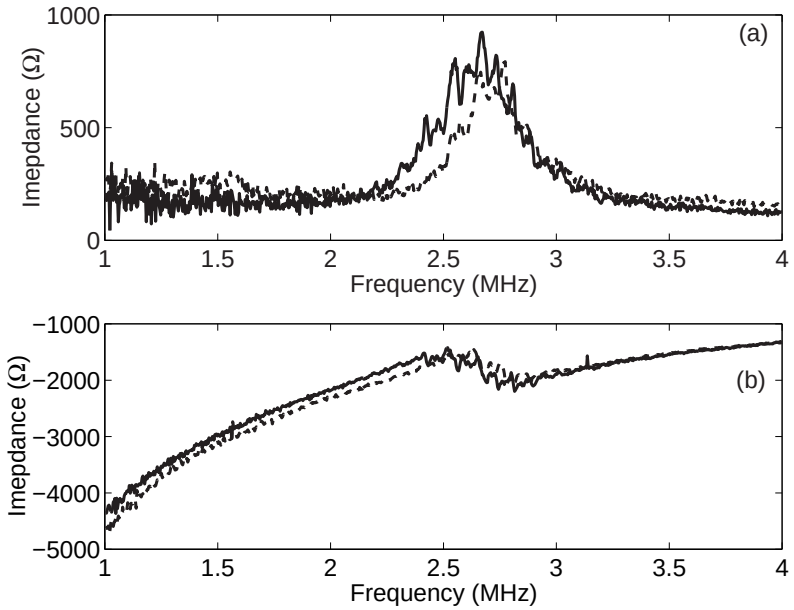

Figure 6.17: (a) Real and (b) imaginary parts of the input impedance. Both transmit (solid) and receive (dashed) ports are shown without the matching network.

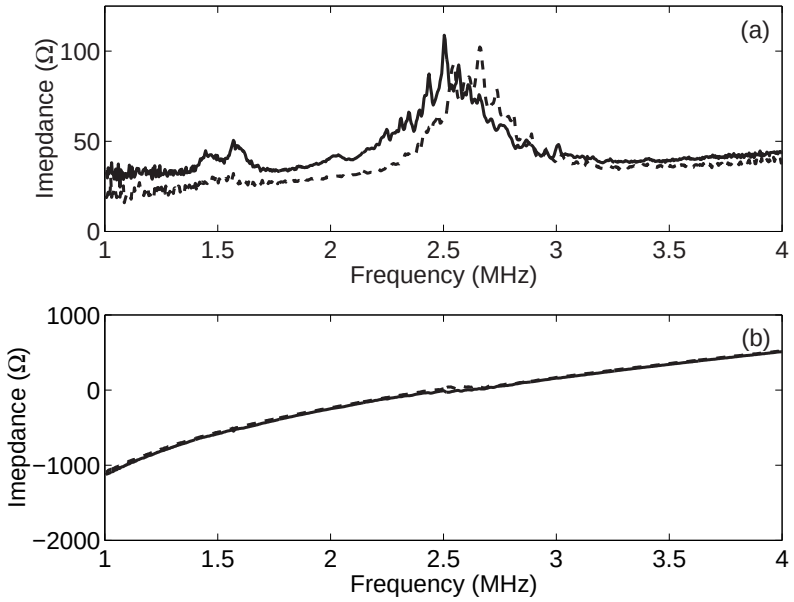

Figure 6.18: (a) Real and (b) imaginary parts of the input impedance. Both transmit (solid) and receive (dashed) ports are shown with the matching network.

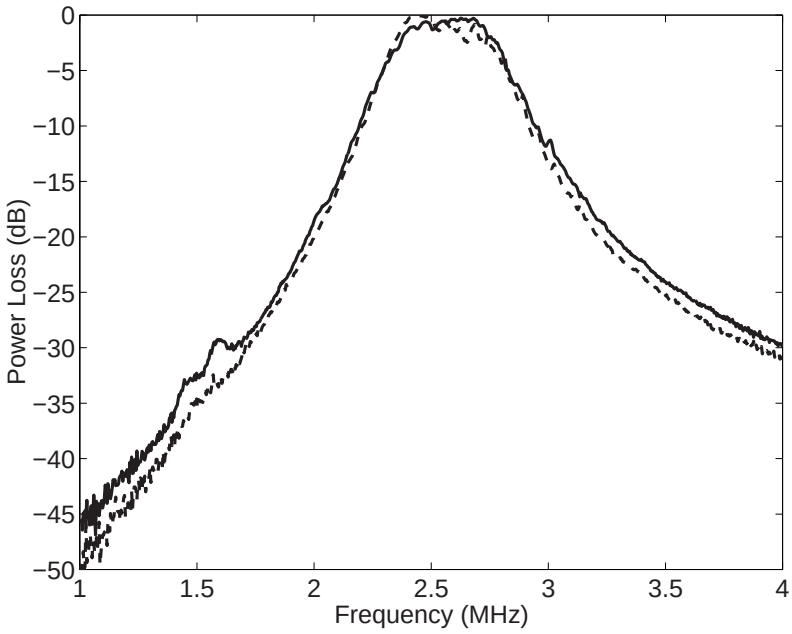

Figure 6.19: Power loss associated with the matching network for the transmit (solid) and receive (dashed) ports using the impedance data of Figure 6.18 in conjunction with (6.2).

problem lies in the difficulty of predicting the resonant frequency of the membrane. The presence of this mismatch is verified by impulse responses obtained from the laser doppler vibrometer system. Using a laser focused on the membrane surface to measure its displacement, a 3 V, 2.1 MHz electrical pulse was applied to the CMUTs and a fast Fourier transform (FFT) of the resulting waveform was taken to find the spectrum. Note from Figure 6.20 that the resonant frequencies of the individual membranes vary from 2.06 to 2.27 MHz while the substrate displacement spectrum peaks near 1.82 MHz. The former values are a function of the structure's geometry as described by (4.2). The latter number is determined by the interference between the Lamb waves excited at each membrane as dictated by the transducer period. To help show the frequency shifts in a more clear fashion, all of the curves on the graph have been both filtered and normalized.

It should be noted that in situations where the membrane yield is low, there is a major disadvantage in using a single membrane at each port. This is because in cases

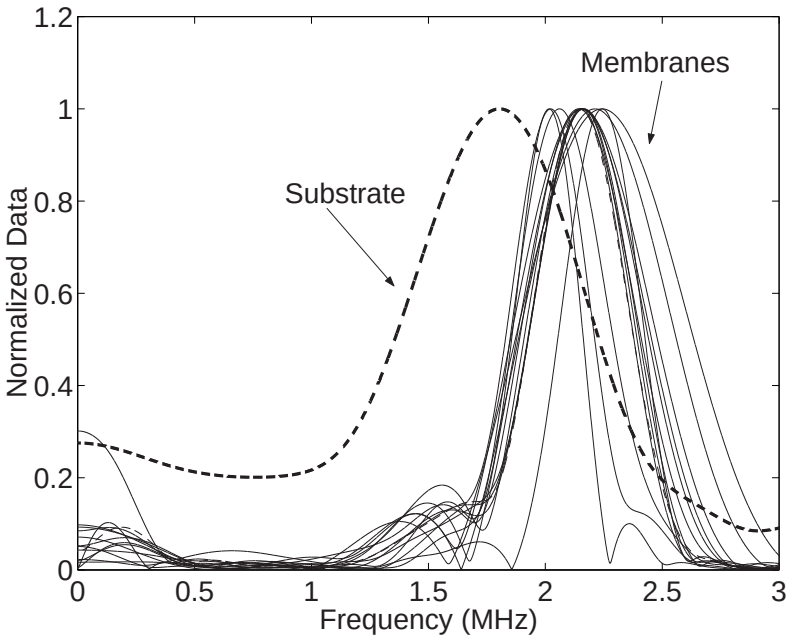

Figure 6.20: Normalized impulse response spectra of the membranes (solid lines) and the device substrate (dashed line).

where there is no redundancy, if a membrane breaks the device is rendered useless. For the sacrificial layer of transducer fabrication, membrane yield is an issue and the implementation of redundancy is encouraged; for the wafer bonding method, the yield is high and using a single membrane at each port is optimal.

6.4 Quantifying Device Efficiency

Section 3.2.3 introduces the concept of insertion loss, the figure of merit used to describe the efficiency of a Lamb device. A graph presenting the insertion loss of three different Lamb wave devices is shown in Figure 6.21, along with Table 6.1 that describes their configurations. Each device represents a major advance in the evolution of efficient Lamb wave devices. It is instructive to follow the progression of the three devices and note the changes that were made in each generation. The insertion loss of Device 3, representing the most efficient structure, is 16 dB. After describing the three different configurations, this section uses both theoretical and

	# of Membranes		Fabrication	Substrate	Membrane	Insertion
	TX Port	RX Port	Method	Thickness	Width	Loss
Device 1	20	1	Sacrificial	500 μm	100 μm	60.5 dB
Device 2	15	15	Sacrificial	18 μm	77 μm	20 dB
Device 3	1	1	Bonding	8 μm	60 μm	16 dB

Table 6.1: Device details for the three curves shown in Figure 6.21.

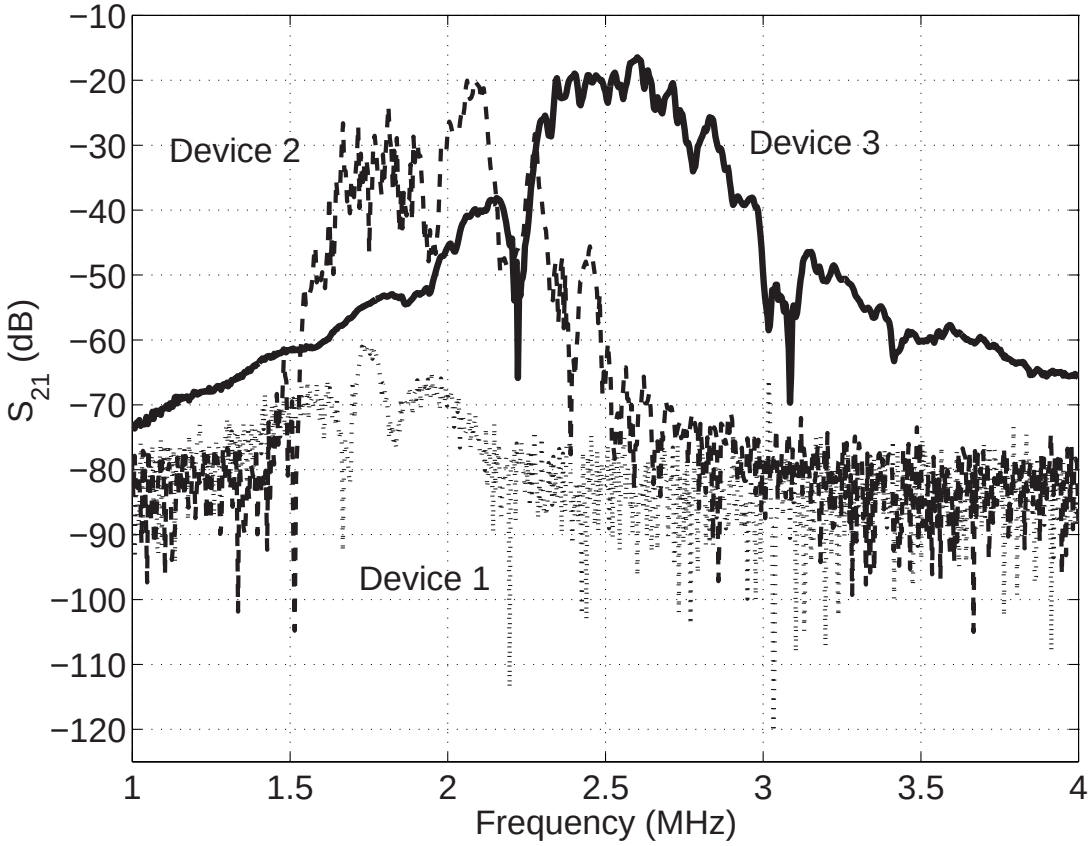

Figure 6.21: Insertion loss of three different Lamb wave devices built using CMUT technology. Details of the device are shown in Table 6.1.

experimental data to account for the losses associated with this device.

6.4.1 Three Generations Of Lamb Wave Devices

Device 1 was built to act as a proof of concept, demonstrating that Lamb waves could be launched and received using CMUTs. It employs rectangular membranes fabricated using the sacrificial layer method and an un-etched 500 μm substrate. The transmit membranes are grouped into four sets of five membranes where the middle of each set is separated by one wavelength. This is a sub-optimal arrangement if the goal is to foster constructive interference of the acoustic wave. The receive side is made of a single transducer separated from the transmitting membranes by 7.8 mm, or approximately 22 wavelengths. The membrane yield for this fabrication run was around 50%; since only a single membrane is used at the receiver, the device yield is also around 50%.

Three major changes were introduced with Device 2, which was also manufactured using the sacrificial layer method. First, in order to increase the device yield, multiple membranes are used at the receive port. Second, the membrane at both ports are spaced evenly with a separation of what was expected to be one wavelength. This is done to optimize constructive interference of the Lamb wave as it is excited at each membrane and travels along the substrate. Third, the substrate is thinned from its original value of 500 μm to a final thickness of 18 μm.

As is evident from both Table 6.1 and Figure 6.21, the device efficiency improved dramatically. There are, however, more improvements that can be made to this structure. The most striking is the frequency mismatch problem described in the previous section (the data in Figure 6.20 is from Device 2). Coupled with this problem is membrane yield. While using multiple membranes at the receive port increases the number of working devices that result from the manufacturing process, almost half of them do not work. In light of the interference effects stemming from the mismatch between the substrate thickness and membrane spacing, the low yield once again makes it difficult to properly predict device behavior. Finally, the effect of the inter-membrane reflections described in the previous section manifest themselves as

ripples in the passband of the device insertion loss.

Device 3 represents the optimal configuration in the device built during the course of this research. The membrane for this structure is 60 μm wide, 1 cm long, and 1.34 μm thick and sits over a 0.97 μm gap. Rather than using the sacrificial layer method of transducer fabrication, the fabrication run for this device employed the simpler wafer bonding method. In addition to saving process time, using this technique dramatically increased the membrane yield from near 50% to 100%. This enables the design to be changed to allow for a single membrane at both the transmit and receive ports, and therefore avoid problems with both reflections and frequency mismatch. In addition, the substrate has been etched to a final thickness of 8 μm. All of these changes result in a very low insertion loss (16 dB at 2.6 MHz) and a much smoother passband.

6.4.2 Accounting For Losses In Device 3

According to the simulations described in Section 4.5.4, under optimal conditions the minimum insertion loss that can be obtained for a Lamb wave device in air built using wafer bonded CMUT technology with the dimensions of Device 3 is 11 dB. Additionally, as shown in Figure 6.19, the losses associated with matching network at 2.6 MHz are 0.4 dB and 1.4 dB at the transmit and receive ports, respectively. Thus, conversion and matching losses add up to 12.8 dB, leaving 3.2 dB unaccounted for. The majority of this loss can most likely be attributed to interference brought about by reflections along the substrate.

6.5 Lamb Wave Sensor Technology

Lamb wave devices work as efficient sensors due to their high sensitivity to various perturbations [10, 97]. Adapting the equation presented by Ballantine et al. [10], the phase velocity of a Lamb wave travelling along a thin plate is determined by (6.3), where T_x is the initial tension in the plate in the propagation direction, B is the bending stiffness of a homogenous, elastically isotropic plate, M is the mass per unit

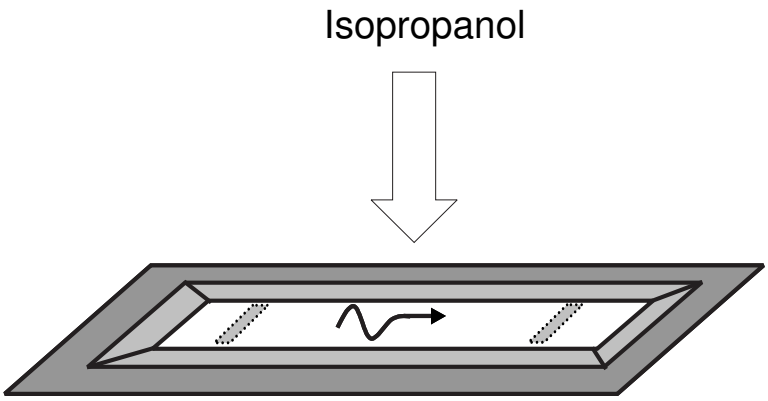

Figure 6.22: Backside of the Lamb wave device where isopropanol is added for the mass loading experiment.

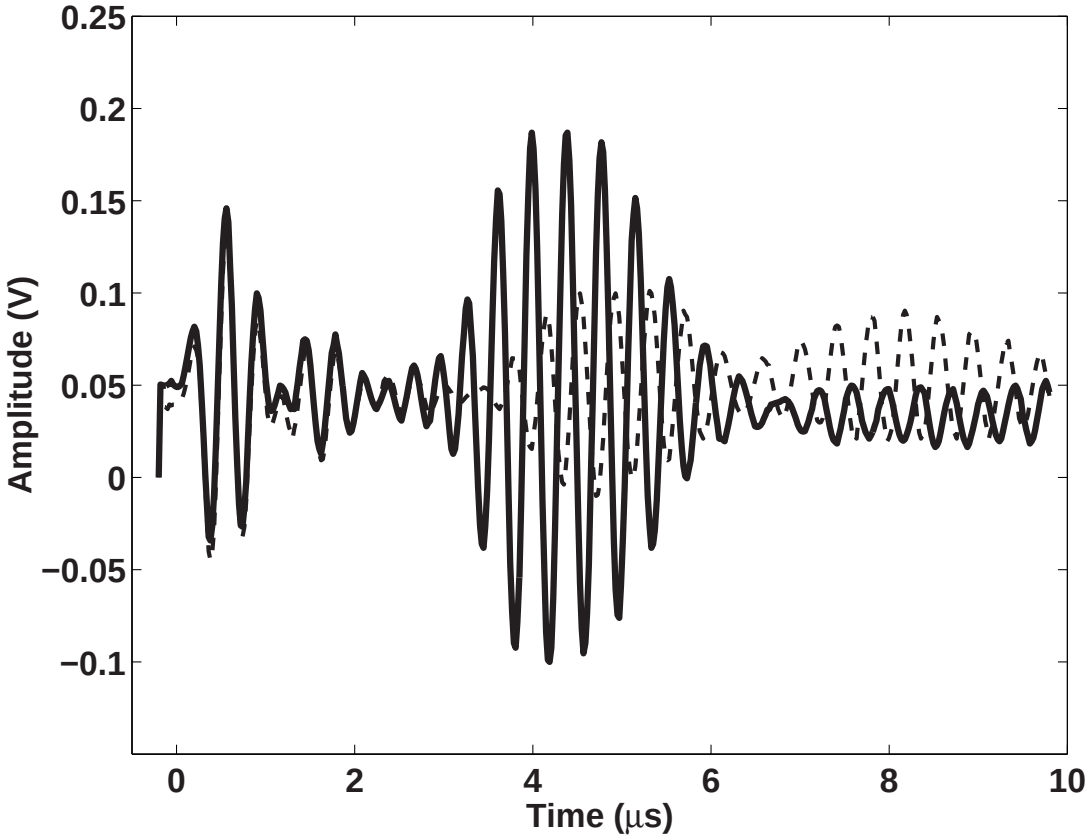

Figure 6.23: Received voltage signal showing the effect of mass loading of a Lamb wave device due to isopropanol. The unloaded (solid) and loaded (dashed) responses are shown.

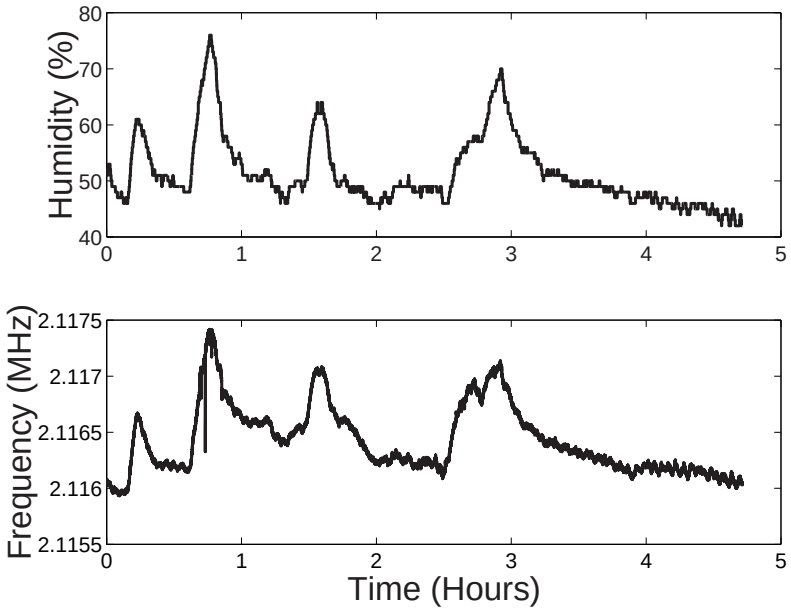

Figure 6.24: Humidity measurement at 23 ^{o}C.

area of the plate, and t' and m' are the changes in the tension and mass of the plate, respectively.

$$v_p = \left(\frac{T_x + t' + B}{M + m'} \right)^{\frac{1}{2}} \tag{6.3}$$

Two experiments were performed in an effort to confirm that the capacitive micromachined ultrasonic Lamb wave transducer has a response similar to that of other Lamb wave devices. In the first experiment, a 16 volt square pulse is applied to the transmit port and the received electrical signal is measured. Isopropanol is then added to the well in the backside of the device as drawn in Figure 6.22; the backside is used so that the solvent makes contact to the substrate but not the vibrating CMUTs. The resulting effect is mass loading of the substrate which, according to (6.3), decreases the phase velocity of the Lamb wave. The curves in Figure 6.23 confirm this behavior. The initial spikes in the graph that are common to both curves is electrical feedthrough; while the Lamb wave arrives near t = 3 μs for the unloaded case and t = 3.8 μs for the loaded case. The amplitude decrease is most likely due

to the leakage of energy from the wave into the isopropanol in the area around the CMUT membrane.

In the second experiment, the device is wired as a delay line oscillator and used to monitor changes in humidity. The velocity of the Lamb wave is affected by changes in the tension of the material on the plate which affect the acoustic wave velocity, and therefore by extension the oscillation frequency as described by (3.70). Figure 6.24 shows the results of an experiment where the Lamb wave device is put into an environment where the relative humidity was changing as a function of time, and the temperature was held constant at 23° C. The top graph shows data taken from an off-the-shelf humidity sensor (Omega-RH411) while the bottom graph shows the frequency of the oscillator. The two curves have a similar shape, although the response of the oscillator is slower than that of the humidity sensor. This behavior is expected because the top of the device channel in this specific case is composed of silicon nitride which is a hydrophilic material that does not easily desorb moisture. The humidity sensor, on the other hand, is designed to respond quickly to moisture changes in its environment. When evaluating Figure 6.24, it is important to remember that the purpose of this experiment was not to show that the Lamb wave device could work as an ideal humidity sensor, but rather that it could respond as one would expect to mass loading.

Chapter 7

Conclusions

The devices developed for this research use capacitive micromachined ultrasonic transducers (CMUTs) to launch and receive Lamb waves along a silicon plate. The dissertation began with a history of Lamb waves and the structures that have been built to facilitate their transduction. After presenting some fundamentals on both CMUTs and Lamb waves, it described how the two concepts could be combined to create a single device. It continued with the derivation of numerous models that describe the device, each representing the effect of $R_{substrate}$, the term used to mathematically describe Lamb wave transduction from a CMUT. The dissertation then went on to describe different manufacturing processes of the structure as well as experimental data obtained from the fabricated transducers.

Based on the results of this research, a number of general conclusions can be made:

• Efficient Lamb wave devices can be built using CMUT technology in the 2 MHz range. Efforts have not yet been put into fabricating them at higher frequencies. The data in Table 7.1 presents a comparison of the device described in this dissertation to others reported in the literature.

• The device is best modeled using finite element analysis. The results of this modeling shows that the device efficiency increases as the substrate thickness decreases. A resistive element, coined $R_{substrate}$, can be added to the standard equivalent circuit model to model the effect of the substrate on the vibrating membrane.

Actuation Method	Frequency	Insertion Loss	Citation
Magnetic	433.2 KHz	23.9 dB	[53]
Optical	2 MHz	Not Given	[103]
Capacitive	2.6 MHz	16 dB	This dissertation
Piezoelectric	4-4.5 MHz	Not Given	[24]
Piezoelectric	4.74 MHz	35 dB	[98]
Piezoelectric	19 MHz	25 dB	[95]
Piezoelectric	19.8 MHz	11.27 dB	[97]

Table 7.1: Comparison of the capacitive microcmachined ultrasonic Lamb wave transducer to other Lamb wave devices.

• Energy from the membrane displacement couples through the posts into the substrate to excite the Lamb wave. Over 95% of the power in the wave is in the first order antisymmetric (A_0) mode.

• The optimal fabrication method for the device uses the wafer-bonding method. It does not employ piezoelectric materials and is IC-compatible.

• The resulting geometry should include a single high aspect ratio membrane at both the transmit and receive ports. Furthermore, an effort should be made to mitigate reflections off of the edges of the device.

• This Lamb wave device can work as both a filter and a sensor.

7.1 Contributions

The contributions of this work span several areas in the field of CMUTs and Lamb waves.

Lamb wave transduction using CMUTs This research demonstrated the first experimental verification of Lamb wave transduction using CMUTs. The initial design resulted in a device with an insertion loss of 60 dB. After a series of steps aimed at increasing device efficiency, a 44 dB improvement was attained, resulting in a final insertion loss of 16 dB.

Modeling As a result of this work the modeling tools of the CMUT have been greatly improved. Analytically, the advances range from expressions for the transducer membrane that account for both bending stiffness and tension, to a distributed

model for electromechanical transduction (modeled by the transformer in the equivalent circuit model). Numerically, for the first time both structural and electromechanical elements were used in a finite element analysis in an effort to analyze the CMUT. The results were used to both verify the various analytical models, and to build on the models in an effort to study the transfer of energy from the vibrating membrane to the substrate.

Manufacturing The manufacturing techniques described in this document can be used in the fabrication of both CMUTs and other acoustic wave devices. They demonstrate that high aspect ratio membranes can be built with high yield, that a substrate less than 10 μm thick and 3 cm long can support both a number of these membranes and acoustic wave propagation, and that both the sacrifical layer and wafer bonding methods can be adapted to create acoustic wave devices.

7.2 Future Research

The results of this work point to a number of avenues that should be explored regarding acoustic wave devices built using the capacitive micromachined ultrasonic transducer. First, effort should be put into making the manufacturing process of the Lamb wave device more robust. Since the wafer-bonding method has such a high membrane yield, redundancy at the transmit and receive ports is not necessary. This helps to avoid the frequency mismatch problem discussed in relation to Figure 6.20. Thus, an SOI wafer should be used for the device substrate so that an etch-stop can be incorporated into the process to aid in the final manufacturing step. The tradeoff here is of course cost, as this approach would require the use of two SOIs in order to process a single wafer.

Second, a thorough study is needed regarding the use of this device as a sensor. Since the fundamentals of the structure are now well understood, it follows that the advantages it may hold in this arena should be investigated. Recall that the sensitivity of Lamb wave devices is greater than that of SAW structures; this underscores the importance of better understanding the merits of sensing with Lamb wave devices built using CMUTs.

Of course the ultimate achievement that could be obtained through the efforts begun by this research is to fabricate SAW devices using CMUTs. The SAW market is very lucrative as surface acoustic wave filters make up an important part of the front end of almost all high frequency communication devices. Recent market surveys, however, show that trends toward miniaturization and higher integration are driving prices lower and reducing profitability. To overcome these prices decreases, SAW device manufacturers will be looking for better performing, less expensive, and more easily integrable materials. Results from this work show that the CMUT may be a viable option in this effort. Adapting the results described in this dissertation to higher frequency acoustic wave devices is therefore a logical step in the evolution of the capacitive micromachined ultrasonic Lamb wave transducer.

Appendix A

Processing Details (Sacrificial Layer Method)

For each step below, standard recipes were used in the operation of tools in the Stanford Nanofabrication Facility (SNF). The process, time, and equipment names are given. Cross-sections relating to the process are presented in Figures 5.1 and 5.5. For reference, the standard piranha clean consists of a twenty minutes in a solution of sulfuric acid:hydrogen peroxide ratio of 9:1. Standard diffusion clean consists of ten minues in 4:1 sulfuric acid:hydrogen peroxide, ten minutes in 5:1:1 water:hydrogen peroxide:hydrochloric acid, and 30 seconds in 50:1 water:hydroflouric acid.

	Process	**Target**	**Setting 1**	**Setting 2**	**Tool**	**Comments**
1	Wafer Clean		Standard Piranha		WBNonmetal	
2	Doping	1.1 Ω/sq	POCL1000	01:27:00	Tylan6	
3	Oxide Etch		50:1 HF	00:01:30	WBDiffusion	
4	Wafer Clean		Standard Piranha		WBNonmetal	
5	Wafer Clean		Standard Diff Clean		WBDiffusion	
6	Nitride Deposition	2500 Å	LONH378	01:30:00	TylanNitride	Ins. Layer

	Process	Target	Setting 1	Setting 2	Tool	Comments
7	Poly Deposition	1 μm	PolyEmit	01:19:00	TylanPoly	Sac. Layer
8	Lithography	1 μm Shipley 3612	Hard Contact	1.6 sec	EVAlign	
9	Poly Etch	1 μm	PolyEtch	00:08:02	DrytekII	
10	Resist Strip		Standard Piranha		WBNonmetal	
11	Lithography	1.6 μm Shipley 3612	Hard Contact	2 sec	EVAlign	
12	Poly Etch	9000 Å	Via Etch	00:45:00	AMTEtcher	
13	Poly Etch	1 μm	PolyEtch	00:08:02	DrytekII	Backside
14	Resist Strip		Standard Piranha		WBNonmetal	
15	Wafer Clean		Standard Diff Clean		WBDiffusion	
16	Nitride Deposition	1 μm	LONH378	06:15:00	TylanNitride	Membrane
17	Lithography	1.6 μm Shipley 3612	Hard Contact	2 sec	EVAlign	
18	Nitride Etch	1 μm	Via Etch	00:22:00	AMTEtcher	
19	Polymer Strip		Cleanup	00:03:00	DrytekII/Matrix	
20	Resist Strip		Standard Piranha		WBNonmetal	
21	KOH Etch		22.5% KOH	3-5 Days	WBGeneral	Sac. Etch
22	KOH Cleanup		Std. KOH clean		WBSilicide	
23	Wafer Clean		Standard Diff Clean		WBDiffusion	
24	Nitride Deposition	2000 Å	LONH378	01:12:00	TylanNitride	Seal holes
25	Lithography	1.6 μm Shipley 3612	Hard Contact	2 sec	EVAlign	
26	Nitride Etch	2000 AA	Via Etch	00:06:00	AMTEtcher	

	Process	**Target**	**Setting 1**	**Setting 2**	**Tool**	**Comments**
27	Polymer Strip		Cleanup	00:03:00	DrytekII/Matrix	
28	Resist Strip		Standard Piranha		WBNonmetal	
25	Lithography	1.6 μm Shipley 3612	Hard Contact	2 sec	EVAlign	
26	Nitride Etch	1 μm	Via Etch	00:23:00	AMTEtcher	Ground Pads
27	Polymer Strip		Cleanup	00:03:00	DrytekII/Matrix	
28	Resist Strip		Standard Piranha		WBNonmetal	
29	Metal Deposition	0.3 μm	Al/Si	00:03:00	Gryphon	
30	Lithography	1.6 μm Shipley 3612	Hard Contact	2 sec	EVAlign	
31	Metal Etch	0.3 μm	Std. Al Etch		WBMetal	
32	Lithography	1.6 μm Shipley 3612	Hard Contact	2 sec	EVAlign	
33	Nitride Etch	1.2 μm	Via Etch	00:28:00	AMTEtcher	Backside
34	Polymer Strip		Cleanup	00:03:00	DrytekII/Matrix	
35	Resist Strip		Standard Piranha		WBNonmetal	
36	Backside Etch	Variable	22.5% KOH	Var.	WBGeneral	

Appendix B

Processing Details (Wafer Bonding Method)

Unless otherwise specified, all processing was performed using standard standard at the Stanford Nanofabrication Facility (SNF). The process, time, and equipment names are given. Cross-sections relating to the process are presented in Figures 5.10 and 5.11. For reference, the standard piranha clean consists of a twenty minutes in a solution of sulfuric acid:hydrogen peroxide ratio of 9:1. Standard diffusion clean consists of ten minues in 4:1 sulfuric acid:hydrogen peroxide, ten minutes in 5:1:1 water:hydrogen peroxide:hydrochloric acid, and 30 seconds in 50:1 water:hydroflouric acid.

	Process	**Target**	**Setting 1**	**Setting 2**	**Tool**	**Comments**
1	Wafer Clean		Standard Piranha		WBNonmetal	
2	Wafer Clean		Standard Diff Clean		WBDiffusion	
3	Oxidation	1200 Å	Wet1000	00:12:15	Tylan1-4	
4	Lithography	1.0 μm Shipley 3612	Hard Contact	1.5 sec	EVAlign	
5	Oxide Etch	1200 Å	Oxide Etch	00:05:00	AMTEtcher	
6	Silicon Etch	1 μm	Si Trench	00:30:00	AMTEtcher	

	Process	Target	Setting 1	Setting 2	Tool	Comments
7	Resist Strip		Standard Piranha		WBNonmetal	
8	Wafer Clean		Standard Diff Clean		WBDiffusion	
9	Oxidation	Burn Polymer	Dry1000	00:30:00	Tylan1-4	
10	Oxide Etch		50:1 HF		WBDiffusion	
11	Wafer Clean		Standard Diff Clean		WBDiffusion	
12	Oxidation	6000 Å	Wet1100	00:52:49	Tylan1-4	For ins. layer and bonding
13	Wafer Bonding				MEMS Eng.	$125/wafer
14	Wafer Clean		Standard Diff Clean		WBDiffusion	
15	Nitride Deposition	2000 Å	LONH378	01:00:00	TylanNitride	
16	Photoresist Coating	1.6 μm Shipley 3612				
17	Wafer Grinding				Ginzton Crystal Shop	Leave ~50 μm
18	Silicon Etch	~50 μm	22.5% KOH		WBGeneral	Handle wafer removed
19	Oxide Etch		6:1 HF		WBNonmetal	Box removed by inspection
20	Wafer Clean		Standard Diff Clean		WBDiffusion	
21	Anneal		1100AN	02:00:00	Tylan1-4	Solidify bonding
22	Lithography	1.0 μm Shipley 3612	Hard Contact	1.5 sec	EVAlign	
23	Silicon Etch	1.34 μm	Si Etch	00:09:00	DrytekII	Define Membranes
24	Wafer Clean		Standard Diff Clean		WBDiffusion	
25	Nitride Deposition	550 Å	LONH378	00:16:30	TylanNitride	
26	Lithography	1.6 μm Shipley 3612	Hard Contact	2 sec	EVAlign	

	Process	**Target**	**Setting 1**	**Setting 2**	**Tool**	**Comments**
27	Nitride Etch	1.2 μm	Via Etch	00:28:00	AMTEtcher	Backside
28	Polymer Strip		Cleanup	00:03:00	DrytekII	
29	Resist Strip		Standard Piranha		WBNonmetal	
30	Metal Deposition	0.3 μm	Al/Si	00:03:00	Gryphon	
31	Lithography	1.6 μm Shipley 3612	Hard Contact	2 sec	EVAlign	
32	Metal Etch	0.3 μm	Std. Al Etch		WBMetal	
33	Anneal		FGA375	00:30:00	TylanFGA	
34	Backside Etch	Variable	22.5% KOH	Var.	WBGeneral	

Bibliography

[1] J.D. Achenbach. *Wave Propagation In Solids*. North-Holland Publishing Company, 1973.

[2] E.L. Adler. Electromechanical coupling to lamb and shear-horizontal modes in piezoelectric plates. *IEEE Transactions on Ultrasonics, Ferroelectrics and Frequency Control*, 36(2):223 – 30, March 1989.

[3] M. Aslam, B.E. Artz, S.L. Kaberline, and T.J. Prater. A comparison of cleaning procedures for removing potassium from wafers exposed to koh. *IEEE Transactions on Electron Devices*, 40(2):292 – 5, February 1993.

[4] B.A. Auld. *Acoustic Fields and Waves in Solids*, volume I. Krieger Publishing Company, 1990.

[5] B.A. Auld. *Acoustic Fields and Waves in Solids*, volume II. Krieger Publishing Company, 1990.

[6] B.A. Auld and M. Tan. Symmetrical lamb wave scattering at a symmetrical pair of thin slots. In *1977 Ultrasonics Symposium Proceedings, 26-28 Oct. 1978, Phoenix, AZ, USA*.

[7] M.H. Badi, G.G. Yaralioglu, A.S. Ergun, S.T. Hansen, E.J. Wong, and B.T. Khuri-Yakub. Capacitive micromachined ultrasonic lamb wave transducers using rectangular membranes. *IEEE Transactions on Ultrasonics, Ferroelectrics and Frequency Control*, 50(9):1191 – 203, September 2003.

[8] M.H. Badi, G.G. Yaralioglu, A. Sanli Ergun, F. Levent Degertekin, C.H. Cheng, and B.T. Khuri-Yakub. A first experimental verification of micromachined capacitive lamb wave transducers. In *2000 IEEE Ultrasonics Symposium. Proceedings. An International Symposium, 22-25 Oct. 2000, San Juan, Puerto Rico.*

[9] D.F. Ball and D. Shewring. Lamb waves for inspection of commercially rolled hot strip material. *Non-Destructive Testing*, 9(1):13 – 16, February 1976.

[10] D.S. Ballantine, R.M. White, S.J. Martin, A.J. Ricco, E.T. Zellers, G.C. Frye, and H. Wohltjen. *Acoustic Wave Sensors.* Academic Press, 1997.

[11] D. Bancroft. The velocity of longitudinal waves in cylindrical bars. *Phsyical Review*, 59:588–593, 1941.

[12] F. Bendec, M. Peretz, and S.I. Rokhlin. Ultrasonic lamb wave method for sizing of spot welds. *Ultrasonics*, 22(2):78 – 84, March 1984.

[13] Leo L. Beranek. *Acoustics.* Acoustical Society of America, 1993.

[14] A. Bozkurt, F.L. Degertekin, A. Atalar, and B.T. Khuri-Yakub. Analytic modeling of loss and cross-coupling in capacitive micromachined ultrasonic transducers. In *1998 IEEE Ultrasonics Symposium. Proceedings, 5-8 Oct. 1998, Sendai, Japan.*

[15] A. Bozkurt, I. Ladabaum, A. Atalar, and B.T. Khuri-Yakub. Theory and analysis of electrode size optimization for capacitive microfabricated ultrasonic transducers. *IEEE Transactions on Ultrasonics, Ferroelectrics and Frequency Control*, 46(6):1364 – 74, November 1999.

[16] A. Caronti, G. Caliano, A. Iula, and M. Pappalardo. An accurate model for capacitive micromachined ultrasonic transducers. *IEEE Transactions on Ultrasonics, Ferroelectrics and Frequency Control*, 49(2):159 – 68, February 2002.

[17] C. Chree. *Trans. Camb. Phil. Soc.*, 14:250, 1889.

[18] Richard S.C. Cobbold. *Transducers For Biomedical Measurements: Principles and Applications*. Wiley-Interscience, 1974.

[19] F. Levent Degertekin. *Hertzian contact lamb wave sensors*. PhD thesis, Stanford University, 1997.

[20] P. Diodati, G. Tassi, and A. Alippi. Lamb wave reflection at plate edges. *Applied Physics Letters*, 47(6):573 – 5, September 1985.

[21] B. Drafts. Acoustic wave technology sensors. *Sensors Magazine*, 17(10), October 2000.

[22] Eisler Evans, Hadley and Silverman. *Geophysics*, 19:20, 1954.

[23] R. D. Fay and O. V. Fortier. Transmission of sound through steel plates immersed in water. *Journal of the Acoustical Society of America*, 23(3):339 – 346, 1951.

[24] D. Fischer, W.J. Varhue, J. Wu, and C.A. Whiting. Lamb-wave microdevices fabricated on monolithic single crystal silicon wafers. *Journal of Microelectromechanical Systems*, 9(1):88 – 93, March 2000.

[25] V. Foglietti, D. Memmi, G. Caliano, E. Cianci, F. Galanello, and M. Pappalardo. Fabrication of micromechanical capacitive ultrasonic transducers by surface micromachining. In *International Conference on Microtechnologies: MICRO.tec 2000, 25-27 Sept. 2000, Hannover, Germany.*

[26] T. Giesler and J.-U. Meyer. Electrostatic excitation and capacitive detection of flexural plate-waves. *Sensors and Actuators A (Physical)*, A36(2):113 – 19, April 1993.

[27] T. Giesler and J.-U. Meyer. Electrostatically excited and capacitively detected flexural plate waves on thin silicon nitride membranes with chemical sensor applications. *Sensors and Actuators B (Chemical)*, B18(1-3):103 – 6, March 1994.

[28] Karl F. Graf. *Wave Motion In Elastic Solids.* Ohio State University Press, 1975.

[29] N.A. Hall and F.L. Degertekin. Integrated optical interferometric detection method for micromachined capacitive acoustic transducers. *Applied Physics Letters*, 80(20):3859 – 61, May 2002.

[30] M.I. Haller and B.T. Khuri-Yakub. A surface micromachined electrostatic ultrasonic air transducer. In *IEEE Ultrasonics Symposium, 1-4 Nov. 1994, Cannes, France.*

[31] Cheol-Hyun Han and Eun Sok Kim. Fabrication of dome-shaped diaphragm with circular clamped boundary on silicon substrate. In *12th International Workshop on Micro Electro Mechanical Systems - MEMS, 17-21 Jan. 1999, Orlando, FL, USA.*

[32] S. Hansen, N. Irani, F.L. Degertekin, I. Ladabaum, and B.T. Khuri-Yakub. Defect imaging by micromachined ultrasonic air transducers. In *1998 IEEE Ultrasonics Symposium. Proceedings, 5-8 Oct. 1998, Sendai, Japan.*

[33] S.T. Hansen, A.S. Ergun, and B.T. Khuri-Yakub. Acoustic sensing using radio frequency detection and capacitive micromachined ultrasonic transducers. In *2001 IEEE MTT-S International Microwave Symposium Digest, 20-25 May 2001, Phoenix, AZ, USA.*

[34] M. Hattunen and M. Luukkala. An investigation of generalized lamb waves using ultrasonic reflectivity measurements. *Applied Physics*, 2(5):257 – 63, November 1973.

[35] G.C. Hilton, J.M. Martinis, K.D. Irwin, N.F. Bergren, D.A. Wollman, M.E. Huber, S. Deiker, and S.W. Nam. Microfabricated transition-edge x-ray detectors. *IEEE Transactions on Applied Superconductivity*, 11(1 pt.1):739 – 42, March 2001.

[36] Yongli Huang, A.S. Ergun, E. Haeggstrom, M.H. Badi, and B.T. Khuri-Yakub. Fabricating capacitive micromachined ultrasonic transducers with wafer-bonding technology. *Journal of Microelectromechanical Systems*, 12(2):128 – 37, April 2003.

[37] G.E. Hudson. Dispersion of elastic waves in solid circular cylinders. *Phsyical Review*, 63:46–51, 1943.

[38] F.V. Hunt. *Electroacoustics; The Analysis of Transduction and its Historical Background*. Acoustical Society of America, 1954,1982.

[39] Umran S. Inan and Aziz S. Inan. *Electromagnetic Waves*. Prentice Hall, 2000.

[40] Götz J. Über den schalldurchgang durch metallplatten in flüssigkeiten bei schrägem einfall einer ebenen welle. *Akust. Z.*, 8:145–168, 1943.

[41] H. Jagannathan, G.G. Yaralioglu, A.S. Ergun, F.L. Degertekin, and B.T. Khuri-Yakub. Micro-fluidic channels with integrated ultrasonic transducers. In *2001 IEEE Ultrasonics Symposium. Proceedings. An International Symposium, 7-10 Oct. 2001, Atlanta, GA, USA*.

[42] X.C. Jin. *Micromachined capacitive ultrasonic immersion transducer array*. PhD thesis, Stanford University, 2002.

[43] X.C. Jin, F.L. Degertekin, S. Calmes, X.J. Zhang, I. Ladabaum, and B.T. Khuri-Yakub. Micromachined capacitive transducer arrays for medical ultrasound imaging. In *1998 IEEE Ultrasonics Symposium. Proceedings, 5-8 Oct. 1998, Sendai, Japan*.

[44] S.G. Joshi. Electronically variable time delay in ultrasonic lamb wave delay lines. In *1996 IEEE Ultrasonics Symposium. Proceedings, 3-6 Nov. 1996, San Antonio, TX, USA*.

[45] Gordon S. Kino. *Acoustic waves : devices, imaging, and analog signal processing*. Prentice-Hall, 1987.

[46] Herbert Kolsky. *Stress Waves in Elastic Media*. Dover Publications, Inc., 1963.

[47] Gregory T.A. Kovacs. *Micromachined Transducers Sourcebook*. McGraw-Hill, 1998.

[48] I. Ladabaum, Xuecheng Jin, H.T. Soh, A. Atalar, and B.t. Khuri-Yakub. Surface micromachined capacitive ultrasonic transducers. *IEEE Transactions on Ultrasonics, Ferroelectrics and Frequency Control*, 45(3):678 – 90, May 1998.

[49] H. Lamb. On the flexure of an elastic plate. *Proceedings of the London Mathematical Society*, 21:70, 1889.

[50] H. Lamb. On waves in an elastic plate. *Proceedings of the Royal Society of London*, A93(648):114–128, 1917.

[51] Daryl L. Logan. *A First Course in the Finite Element Method*. Wadsworth Group, 2002.

[52] W. Manthey, N. Kroemer, and V. Magori. Ultrasonic transducers and transducer arrays for applications in air. *Measurement Science & Technology*, 3(3):249 – 61, March 1992.

[53] S.J. Martin, M.A. Butler, J.J. Spates, W. Kent Schubert, and M.-A. Mitchell. Magnetically-excited flexural plate wave resonator. *IEEE Transactions on Ultrasonics, Ferroelectrics and Frequency Control*, 45(5):1381 – 7, September 1998.

[54] Warren P. Mason. *Electromechanical Transducers and Wave Filters*. D. Van Nostrand Company, 1942.

[55] J. McLean and F.L. Degertekin. Capacitive micromachined ultrasonic transducers with asymmetric membranes for microfluidic applications. In *2001 IEEE Ultrasonics Symposium. Proceedings. An International Symposium, 7-10 Oct. 2001, Atlanta, GA, USA*.

[56] Julius Miklowitz. *Elastic Waves and Waveguides*. North-Holland Publishing Company, 1978.

[57] R.M. Moroney, R.M. White, and R.T. Howe. Fluid motion produced by ultrasonic lamb waves. In *IEEE 1990 Ultrasonics Symposium Proceedings, 4-7 Dec. 1990, Honolulu, HI, USA*.

[58] R.M. Moroney, R.M. White, and R.T. Howe. Ultrasonic micromotors. In *IEEE 1989 Ultrasonics Symposium Proceedings, 3-6 Oct. 1989, Montreal, Que., Canada*.

[59] R.M. Moroney, R.M. White, and R.T. Howe. Microtransport induced by ultrasonic lamb waves. *Applied Physics Letters*, 59(7):774 – 6, August 1991.

[60] R.W. Morse. Dispersion of compressional waves in isotropic rods of rectangular cross section. *Journal of the Acoustical Society of America*, 20(6):833–838, November 1948.

[61] E. Moulin, J. Assaad, C. Delebarre, and D. Osmont. Modeling of lamb waves generated by integrated transducers in composite plates using a coupled finite element-normal modes expansion method. *Journal of the Acoustical Society of America*, 107(1):87 – 94, January 2000.

[62] K. Niederer, P.-C. Eccardt, H. Meixner, and R. Lerch. Micromachined transducer design for minimized generation of surface waves. In *1999 IEEE Ultrasonics Symposium. Proceedings. International Symposium, 17-20 Oct. 1999, Caesars Tahoe, NV, USA*.

[63] O. Oralkan, A.S. Ergun, J.A. Johnson, M. Karaman, U. Demirci, K. Kaviani, T.H. Lee, and B.T. Khuri-Yakub. Capacitive micromachined ultrasonic transducers: next-generation arrays for acoustic imaging?. *IEEE Transactions on Ultrasonics, Ferroelectrics and Frequency Control*, 49(11):1596 – 610, November 2002.

[64] M.F.M Osborne and S.D. Hart. Transmission, reflection, and guiding of an exponential pulse by a steel plate in water. i. theory. *The Journal of the Acoustical Society of America*, 17(1):1–18, July 1945.

[65] A. Palma, L. Palmieri, G. Socino, and E. Verona. Lamb-wave electroacoustic voltage sensor. *Journal of Applied Physics*, 58(8):3265 – 7, October 1985.

[66] K.E. Peterson. Silicon as a mechanical material. *Proceedings of the IEEE*, 70(5):420–457, May 1982.

[67] T.J. Plona, M. Behravesh, and G. Mayer. Rayleigh and lamb waves at liquid-solid boundaries. *Ultrasonics*, 13(4):171 – 4, July 1975.

[68] J.D. Plummer, M.D. Deal, and P.B. Griffin. *Silicon VLSI Technology; Fundamentals, Practice, and Modeling*. Prentice Hall, 2000.

[69] L.A. Pochhammer. Biegung des kreiscylinders–fortpflanzungs-geschwindigkeit kleiner schwingungen in einem kreiscylinder. *J. reine angew. Math.*, 81:324, 1876.

[70] Lord (J.W. Strutt) Rayleigh. On waves propagated along the plane surfaces of an elastic solid. *Proc. London Math. Soc.*, 17:4–11, 1885.

[71] Lord (J.W. Strutt) Rayleigh. On the free vibrations of an infinite plate of homogenous isotropic elastic matter. *Proceedings of the London Mathematical Society*, 20:225, 1889.

[72] H. Reissner. Der senkrechte und schräge durchtritt einer in einem fluüsigen medium erzeugten ebenen dilations -(longitudinal)-welle durch eine in diesem medium befindliche planparallele fest platten. *Helvetica Physica Acta*, 2:140–155, 1938.

[73] Yongrae Roh and B.T. Khuri-Yakub. Finite element modeling of capacitor micromachined ultrasonic transducers. In *2000 IEEE Ultrasonics Symposium. Proceedings. An International Symposium, 22-25 Oct. 2000, San Juan, Puerto Rico*.

[74] K. Röhrich. *Zeits. f. Physik*, 73:813, 1931.

[75] S. Rokhlin. Diffraction of lamb waves by a finite crack in an elastic layer. *Journal of the Acoustical Society of America*, 67(4):1157 – 65, April 1980.

[76] F.H. Sanders. Transmission of sound through thin plates. *Canadian Journal of Research*, A17:179–193, 1939.

[77] D.W. Schindel, D.A. Hutchins, Lichun Zou, and M. Sayer. The design and characterization of micromachined air-coupled capacitance transducers. *IEEE Transactions on Ultrasonics, Ferroelectrics and Frequency Control*, 42(1):42 – 50, January 1995.

[78] H. Seidel, L. Csepregi, A. Heuberger, and H. Baumgartel. Anisotropic etching of crystalline silicon in alkaline solutions. i. orientation dependence and behavior of passivation layers. *Journal of the Electrochemical Society*, 137(11):3612 – 26, November 1990.

[79] Irving H. Shames and Clive L. Dym. *Energy and Finite Element Methods in Structural Mechanics*. Hemisphere Publishing Corporation, 1985.

[80] S.K. Shear and A.B. Focke. Dispersion of supersonic waves in cylindrical rods of polycrystalline silve, nickel, and magnesium. *Phsyical Review*, 57:532–537, 1940.

[81] Y. Shinoda and K. Toda. Lamb wave device for amplitude modulation. *Journal of the Acoustical Society of America*, 65(2):537 – 40, February 1979.

[82] E.J. Skudrzyk. Vibrations of a systems with a finite or an infinite number of resonances. *The Journal of the Acoustical Society of America*, 30:1140–1152, 1958.

[83] P.R. Stepanishen. The radiation impedance of a rectangular piston. *Journal of Sound and Vibration*, 55(2):275–288, 1977.

[84] P. M. Sutton. Propagation of sound in plate-shaped solid delay lines. *Journal of the Acoustical Society of America*, 31(1):34 – 43, 1959.

[85] H.A.C. Tilmans. Equivalent circuit representation of electromechanical transducers. ii. distributed-parameter systems. *Journal of Micromechanics and Microengineering*, 7(4):285 – 309, December 1997.

[86] S. Timoshenko. On the correction for shear of the differential equation for transverse vibrations of prismatic bars. *Philosophical Magazine*, 41(6):744–746, 1922.

[87] S. Timoshenko. On the transverse vibrations of bars of uniform cross-section. *Philosophical Magazine*, 43(6):125–131, 1922.

[88] N. Tirole, A. Choujaa, D. Hauden, G. Martin, P. Blind, and M. Froelicher. Lamb waves pressure sensor using an aln/si structure. In *IEEE Ultrasonics Symposium, 31 Oct.-3 Nov. 1993, Baltimore, MD, USA*.

[89] K. Toda. Lamb-wave delay lines with interdigital electrodes. *Journal of Applied Physics*, 44(1):56 – 62, January 1973.

[90] K. Toda. Frequency characteristics of an interdigital transducer for lamb wave excitation. *Journal of Applied Physics*, 45(12):5136 – 40, December 1974.

[91] K. Toda. Lamb wave in a thin piezoelectric ceramic plate under influence of static tensile stress. *Journal of Applied Physics*, 46(12):5114 – 5115, 1975.

[92] K. Toda and Y. Yamashita. A lamb wave device for a communication system with ternary logic. *Proceedings of the IEEE*, 68(2):297 – 8, February 1980.

[93] I. Tolstoy and E. Usdin. Wave propagation in elastic plates - low and high mode dispersion. *Journal of the Acoustical Society of America*, 29(1):37 – 42, 1957.

[94] C. C. Tseng. Frequency response of an interdigital transducer for excitation of surface elastic waves. *IEEE Transactions on Electron Devices*, ED15(8):586.

[95] M.J. Vellekoop, G.W. Lubking, P.M. Sarro, and A. Venema. Integrated-circuit-compatible design and technology of acoustic-wave-based microsensors. *Sensors and Actuators A (Physical)*, A44(3):249 – 63, September 1994.

[96] I. A. Viktorov. Ultrasonic lamb waves (review). *Soviet Physics Acoustics-USSR*, 11(1):1 – 13, 1965.

[97] M.S. Weinberg, C.E. Dube, A. Petrovich, and A.M. Zapata. Fluid damping in resonant flexural plate wave device. *Journal of Microelectromechanical Systems*, 12(5):567 – 76, October 2003.

[98] S.W. Wenzel. *Applications of Ultrasonic Lamb Waves*. PhD thesis, University of California at Berkeley, 1992.

[99] S.W. Wenzel and R.M. White. A multisensor employing an ultrasonic lamb-wave oscillator. *IEEE Transactions on Electron Devices*, 35(6):735 – 43, June 1988.

[100] R. M. White and F. W. Voltmer. Direct piezoelectric coupling to surface elastic waves. *Applied PHysics Letters*, 7(12):314 – 316, 1965.

[101] R.M. White, P.J. Wicher, S.W. Wenzel, and E.T. Zellers. Plate-mode ultrasonic oscillator sensors. *IEEE Transactions on Ultrasonics, Ferroelectrics and Frequency Control*, UFFC-34(2):162 – 71, March 1987.

[102] D. C. Worlton. Experimental confirmation of lamb waves at megacycle frequencies. *Journal of Applied Physics*, 32(6):967 – 971, 1961.

[103] Yihui Wu, M. de Labachelerie, and F. Bastien. Investigations on excitation and detection methods for lamb wave sensors [biosensors]. *Sensors and Actuators A (Physical)*, A100(2-3):214 – 22, September 2002.

[104] Guizhen Yan, P.C.H. Chan, I-Ming Hsing, R.K. Sharma, J.K.O. Sin, and Yangyuan Wang. An improved tmah si-etching solution without attacking exposed aluminum. *Sensors and Actuators A (Physical)*, A89(1-2):135 – 41, March 2001.

[105] G.G. Yaralioglu, M.H. Badi, A.S. Ergun, C.H. Cheng, B.T. Khuri-Yakub, and F.L. Degertekin. Lamb wave devices using capacitive micromachined ultrasonic transducers. *Applied Physics Letters*, 78(1):111 – 13, January 2001.

[106] G.G. Yaralioglu, F.L. Degertekin, M.H. Badi, B.A. Auld, and B.T. Khuri-Yakub. Finite element method and normal mode modeling of capacitive micromachined saw and lamb wave transducers. In *2000 IEEE Ultrasonics Symposium. Proceedings. An International Symposium, 22-25 Oct. 2000, San Juan, Puerto Rico.*